

**THE EFFECT OF WAVES ON BENTHIC EXCHANGE:  
MEASUREMENT AND ESTIMATION OVER A BROAD RANGE  
OF SPATIAL AND TEMPORAL SCALES**

by

Christopher John Russoniello

A dissertation submitted to the Faculty of the University of Delaware in partial fulfillment of the requirements for the degree of Doctor of Philosophy in Geology

Spring 2018

© 2018 Christopher Russoniello  
All Rights Reserved

**THE EFFECT OF WAVES ON BENTHIC EXCHANGE:  
MEASUREMENT AND ESTIMATION OVER A BROAD RANGE  
OF SPATIAL AND TEMPORAL SCALES**

by

Christopher John Russoniello

Approved: \_\_\_\_\_  
Neil C. Sturchio, Ph.D.  
Chair of the Department of Geological Sciences

Approved: \_\_\_\_\_  
Estella A. Atekwana, Ph.D.  
Dean of the College of Earth, Ocean and Environment

Approved: \_\_\_\_\_  
Ann L. Ardis, Ph.D.  
Senior Vice Provost for Graduate and Professional Education

I certify that I have read this dissertation and that in my opinion it meets the academic and professional standard required by the University as a dissertation for the degree of Doctor of Philosophy.

Signed:

---

Holly Anne Michael, Ph.D.  
Professor in charge of dissertation

I certify that I have read this dissertation and that in my opinion it meets the academic and professional standard required by the University as a dissertation for the degree of Doctor of Philosophy.

Signed:

---

Audrey Hucks Sawyer, Ph.D.  
Member of dissertation committee

I certify that I have read this dissertation and that in my opinion it meets the academic and professional standard required by the University as a dissertation for the degree of Doctor of Philosophy.

Signed:

---

William J. Ullman, Ph. D.  
Member of dissertation committee

I certify that I have read this dissertation and that in my opinion it meets the academic and professional standard required by the University as a dissertation for the degree of Doctor of Philosophy.

Signed:

---

Fengyan Shi, Ph.D.  
Member of dissertation committee

## ACKNOWLEDGMENTS

I would like to first thank my advisor, Dr. Holly Michael, for helping on my journey of scientific- and self-discovery. The academic incubator you have created in Penny Hall is remarkable and unique. Your patience and insight guided me along a path where I learned about this discipline and the scientific method, and your enthusiasm, intelligence and integrity were continually infectious and inspiring.

To my committee members, Dr. William Ullman, Dr. Audrey Sawyer, and Dr. Fengyan Shi, your time, suggestions, and comments improved these projects greatly.

I am indebted to my lab group for their support, discussions, and encouragement both in and outside of the office, especially James Heiss, Carlos Duque Calvache, Cristina Fernandez, and Mahfuz Khan. I cannot thank you enough for academic and emotional support. James, you have been especially involved in this journey in so many ways—the journey would have been so much less interesting and fruitful without you.

To everyone who joined me in the field, I would still be wearing a wetsuit without your help. James Heiss, Aline Pieterse, Thijs Lanckriet, Mahfuz Khan, Kyra Kim, Lindsey Byron, Andrew Musetto, Kevin Myers, Deon Knights, Cristina Fernandez, Carlos Duque, and Margaret MacGibeny thank you for donating so much of your time.

To all my friends and family—thank you. Mom and dad, thank you for your unwavering encouragement in all walks of life. And finally, Margaret, I would not be the person I am without you, your patience, and your unconditional support.

## TABLE OF CONTENTS

LIST OF TABLES .....	viii
LIST OF FIGURES .....	ix
ABSTRACT.....	xiv

### Chapter

1	INTRODUCTION .....	1
1.1	Problems in Coastal Seas .....	1
1.2	Role of Seabed Aquifers in Chemical Cycling .....	2
1.3	Benthic Exchange Mechanisms in Coastal Seas.....	3
1.4	Methods to Quantify Benthic Exchange .....	4
1.5	Broader Significance.....	6
2	INVESTIGATION OF SEEPAGE METER MEASUREMENTS IN STEADY FLOW AND WAVE CONDITIONS .....	7
	Abstract .....	7
2.1	Introduction.....	8
2.2	Methods.....	10
2.2.1	Seepage Meter Design .....	10
2.2.2	Tank Experiments .....	10
2.2.3	Wave Flume Experiments.....	11
2.3	Results.....	16
2.3.1	Tank Experiments .....	16
2.3.2	Wave Flume Experiments.....	18
2.3.2.1	Seepage Meter Measurements of Wave-Induced Flux .	18
2.3.2.2	Comparison of Methods to Measure Unidirectional Flux .....	19
2.3.2.3	Effect of the Seepage Meter on Pressure and Flux Across the Bed .....	20
2.4	Discussion .....	21

2.5	Conclusion .....	23
2.6	Acknowledgements.....	24
3	<b>VARIABILITY IN BENTHIC EXCHANGE RATE, DEPTH, AND RESIDENCE TIME BENEATH A SHALLOW COASTAL ESTUARY .....</b>	<b>25</b>
	Abstract.....	25
3.1	Introduction.....	26
3.2	Background.....	29
	3.2.1 Field Site .....	29
	3.2.2 Analytical and Empirical Equations for Calculation of Benthic Exchange Rates .....	30
3.3	Methods.....	33
	3.3.1 Field Instrumentation and Data Collection .....	33
	3.3.1.1 Seabed Hydraulic Properties.....	33
	3.3.1.2 Tripod.....	34
	3.3.1.3 Differential Pressure Measurements .....	35
	3.3.1.4 ADCP Data .....	37
	3.3.2 Wind Data .....	39
3.4	Results.....	42
	3.4.1 Wave-Induced Benthic Exchange.....	42
	3.4.1.1 Field-Based Analysis .....	42
	3.4.1.2 Groundwater Flow Model Results .....	46
	3.4.2 Current- and Tide-Induced Benthic Exchange .....	49
3.5	Discussion.....	51
	3.5.1 Comparison of Wave-Induced Benthic Exchange Methods.....	51
	3.5.2 Exchange Zone Thickness .....	54
	3.5.3 Sources of Uncertainty.....	55
	3.5.4 Comparisons to Larger-Scale Drivers of Exchange.....	56
	3.5.5 Implications for Biogeochemical Reactions .....	56
3.6	Conclusions.....	57
3.7	Acknowledgements.....	58

4	PATTERNS OF WAVE-DRIVEN BENTHIC FLUXES ACROSS THE GLOBAL SEABED.....	59
	Abstract.....	59
	4.1 Introduction.....	60
	4.2 Methods.....	61
	4.3 Results.....	65
	4.3.1 Global Wave Pumping Rates and Patterns .....	65
	4.3.2 Effect of Seabed Heterogeneity .....	70
	4.3.3 Effect of Extreme Events .....	70
	4.4 Discussion.....	73
	4.4.1 Comparison to Previous Estimates and Global Discharge Rates.....	73
	4.4.2 Sources of Inaccuracy .....	74
	4.4.3 Effect of Climate Variability on Wave Pumping.....	75
	4.4.4 Effect of Wave Pumping on Coastal Ocean Chemistry.....	76
	4.5 Conclusion .....	77
5	CONCLUSIONS.....	79
	5.1 Spatial and Temporal Variability in Benthic Exchange .....	80
	5.2 Working Toward Larger Scale Benthic Exchange Estimates.....	80
	5.3 Implications.....	81
	5.4 Recommendations for Future Work.....	82
	REFERENCES .....	86
Appendix		
A	SUPPLEMENTAL INFORMATION FOR CHAPTER 2 .....	103
	A.1 One-Way Valve Characterization .....	103
	A.2 Sediment Characterization .....	103
	A.3 Supplementary Figures for Chapter 2 .....	104
B	SUPPLEMENTAL FIGURES FOR CHAPTER 3.....	105
C	SUPPLEMENTAL FIGURES FOR CHAPTER 4.....	108
D	PERMISSIONS.....	120

## LIST OF TABLES

Table 2.1: Characteristics of the five wave parameter sets (A-E) in wave flume experiments.....	15
Table 3.1: Burst-Averaged Wave-, Current-, and Tide-Induced Benthic Exchange Rates.....	43
Table 3.2: Wave Parameters Calculated with Different Methods .....	45
Table 4.1: Wave pumping rates for single K (and variable K) scenarios for the globe, the seven ocean basins discussed in the paper, and the Mediterranean and Black “Seas” (basin delineations shown in Figure C.5) .....	68
Table C.1 – Wavewatch III Grid information.....	117
Table C.2 – Detailed Single-K simulation results .....	118
Table C.3 – Detailed Variable-K simulation results.....	119

## LIST OF FIGURES

- Figure 2.1: Wave flume experimental set-up and wave-induced flux. a) Cross sectional schematic of wave flume with seepage meter and pressure sensors installed. b) Five seepage meter configurations (I-V). c) Diagram of terminology as illustrated by hypothetical data. Instantaneous flux is shown as solid red and blue lines, which are discharge and recharge components, respectively. Unidirectional flux ( $q$ ) is the discharge or recharge component of flux averaged over multiple wave periods, plotted as dotted red and blue lines, respectively. Net flux is the period-averaged sum of the discharge and recharge flux components, plotted as a bold dashed black line. These hypothetical data illustrate an asymmetric scenario where discharge is greater than recharge. d) Diagram of wave parameters and location of recharge and discharge beneath a surface wave (adapted from King et al. 2009). ..... 13
- Figure 2.2: Measured flux through three seepage meters (SM1-SM3) and the tank for 14 values of hydraulic gradient. The slope of the regression lines are the seepage meter efficiency. Corresponding correlation coefficients ( $R^2$ ) values are shown in the legend. Heavy grey line is the 1:1 line representing a seepage meter efficiency of 100%. ..... 17
- Figure 2.3: Flume experiment data. a) Net flux measured with a seepage meter (SM) and unidirectional flux predicted by theory. b) Unidirectional flux obtained from pressure gradients (Darcy flux), seepage meter measurements, and theory. Letters at top denote the wave parameter set. Note that two wave parameter sets (B and C) have  $L_w$  values of 4.92, but are offset for clarity. .... 19
- Figure 3.1: Site map. a.) State of Delaware, USA. Diamonds indicate 3 weather stations. b.) Holts Landing field site and vicinity. Star indicates tripod location. Dark shaded region indicates area from which wind fetch reaches tripod. .... 30
- Figure 3.2: Schematic illustrating benthic flux drivers, groundwater flowpaths, and parameters controlling each driver for a.) waves, b.) currents over bedforms, and c.) tidally-induced benthic exchange. d.) Representation of terms used to describe different components of wave-induced benthic exchange. See section 3.1.3 for a description of these terms..... 31

Figure 3.3:	Field deployment schematic illustrating tripod components including frame, up- and down-looking ADCPs, six differential pressure sensors within a pole-mounted waterproof case, associated tubing, and locations of tubing orifices. The orifices for two sensors – both a shallow (0-4 cm) and a deep (0-14 cm) – were located at locations 1, 2 and 3. Inset illustrates how tubing for both a shallow (red) and deep (blue) tubing was installed and anchored using an aluminum rod at each of the three locations. Differential pressures were measured between tube ends in shallow (sensors 1s, 2s and 3s) and deep (sensors 1d, 2d, and 3d) tubes. Note that data from only five sensors is presented because data from the deep sensor at location 3 (3s) was erroneous.....	35
Figure 3.4:	Modflow model schematic of geometry and boundaries.....	41
Figure 3.5:	Hourly ADCP-and-wind-generated wave parameters and wave-induced benthic exchange values. a.) Individual and mean wave-induced benthic exchange rates calculated from data collected with 5 pressure sensors. Shaded green region below 10 cm/d represents the measurement error (see discussion in section 5.3). b.) ADCP-derived significant wave height ( $h_w$ ) and peak period ( $T_w$ ) from peaks and PUV methods. Wind c.) fetch and d.) velocity for data from three weather stations. e.) Significant wave height and f.) wave period from ADCP and wind data. g.) Wave-induced exchange rates calculated from pressure sensors (5-sensor average in black, the 2-sensor shallow average and 3-sensor deep average bracket the gray region), and ADCP-derived and wind-derived wave parameters. ....	43
Figure 3.6:	Effect of wave parameters and hydraulic diffusivity on $q_w$ , residence time, and depth of wave-induced flux. a.) Comparison of wave-induced benthic exchange rates from numerical models and calculated from field data. Panels b., c., and d. show average residence time (colorplots) and mean depth of flux (black contours) for each of 260 Modflow model runs. Model thickness was prescribed as $L_w$ , which varied between wave bursts, so the model thickness and depth of plotted data vary temporally. Hydraulic diffusivity was assigned as $3.18 \times 10^{-2}$ , $10^{-1}$ , and $10^0$ to represent clay, sand and gravel for models presented in panels b., c. and d., respectively. The labeled black contours show depths at which vertical flux magnitudes are 50% and 5% of benthic exchange across the bed—the 5% contour ( $d_{ex}$ ) approaches a depth of $L_w/2$ (grey contour) at high hydraulic diffusivity (panel d).....	47

Figure 3.7: Current- and tide-induced benthic exchange values and the data used to calculate them. a.) Color plot of burst-averaged water column velocity profiles from down-looking ADCP. b.) average velocity in middle third of profile (red line), and water depth (black line). c.) Wave-induced  $q_w$  (from differential pressure measurements), current-induced  $q_c$  (from measured currents and range of bedform dimensions), and tide-induced  $q_t$  (from pressure measurements). .....50

Figure 3.8: Comparison of benthic exchange calculation methods. a.) Differential pressure vs. ADCP-measured wave parameters. b.) Differential pressure vs. wind-derived wave parameters. Although plots are in log-log space for clarity, R2 values in both plots are for linear, not log, comparisons..52

Figure 4.1. a) Time-averaged wave pumping rates in the single K scenario. Stippling indicates ocean area with sea ice > 30% of scenario duration. Pink circle around Coral Bank is location of highest wave pumping rate. b) Total volumetric wave pumping rate (black line is mean, grey region is +/- 1 the South China Sea (SCS), Yellow/East China Seas (YS/ECS), Great Barrier Reef (GBR), Gulf of Mexico (GOM), South Atlantic Bight (SAB), Patos Lagoon (PL), North Sea (NS), and Persian Gulf (PG). .....67

Figure 4.2. Wave pumping by basin and latitude for the single-K global scenario. a & c) One-month moving average of volumetric wave pumping for the 31-year scenario. b & d) Average annual volumetric wave pumping (solid lines)—shaded regions encompass +/-1 pumping by latitude normalized to the maximum value at that latitude over the 31-year scenario. Black contours show latitude where 30% of ocean cells are ice-covered. Red arrows illustrate movement of latitudinal peak annual volumetric wave pumping toward equator with time. Black arrows beneath July/August 1999 highlight abnormally-low wave pumping, likely from anomalous wave data. ....69

Figure 4.3. Comparison of SAB wave pumping during normal periods and tropical cyclone (Tr. Cyc.) events. a.) Time series of all wave pumping and extreme events. b.) Close-up view of 1985 (dashed box in a), when 4 tropical cyclones passed through the region and 7 extreme events occurred. Dotted purple line shows potential future with mild overall decrease to wave pumping rates but increase during extreme events. c.) Flux-weighted volumetric wave pumping histogram. d.) Empirical CDF showing cumulative probability wave-pumping event with given strength.....72

Figure 5.1 – Sample idea for a Marine Significance Factor .....85

Figure A.1:	Cross sectional schematic of wave tank with seepage meter installed. A constant head was maintained in both the tank and bucket through all experiments. In recharge experiments, tap water was allowed to overflow the tank and the bucket was lowered below the tank water level. In discharge experiments, tap water was allowed to overflow the bucket and the bucket was raised above the tank water level. The hydraulic gradient was controlled by changing the bucket elevation and was measured between the tank water surface and water level in a manometer tapped into the tank beneath the diffuser. ....	104
Figure B.1:	$(L_e)$ , loading efficiency $(p)$ , for three porosity values ( $n$ ). A value of $5 \times 10^{-10} \text{ Pa}^{-1}$ was used as in Merrit (2004). ....	105
Figure B.2:	Histogram of burst-averaged benthic exchange rate frequency from differential pressure sensors. ....	106
Figure B.3:	a.) Scatter plots of mixing zone depth vs. $L_w$ for 8 sets of MODFLOW models. Exchange zone depth ( $d_{ex}$ was determined as $w/w_0=5\%$ ) from individual model runs are shown as black 'x's. A linear line of best fit (red) is plotted for the 260 model runs of each model set, and the corresponding slope is displayed as a percentage at the top of each chart. b.) Relationship between $d_{ex}/L_w$ and $D$ for the 8 sets of model runs. Black circles indicate high- $D$ model sets in which a mixing zone depth of one-half gravity wavelength is most appropriate. Grey circles indicate model sets where that assumption is less appropriate. Large open circles indicate the three sets of models discussed as low- $D$ , intermediate- $D$ , and high- $D$ in the manuscript. c.) empirical relationship between $d_{ex}$ , $L_w$ , and $D$ . ....	107
Figure C.1:	Sediment type over the global seabed (NAVO, 2010) .....	109
Figure C.2:	Workflow for computing global wave pumping rates .....	110
Figure C.3:	Sensitivity to resolution of the wave simulation data .....	111
Figure C.4:	Sensitivity to simulation resolution (resample resolution) .....	112
Figure C.5:	Basin delineations used in the paper .....	113
Figure C.6:	Flux weighted PDF of flux in the Single-K and Variable-K simulations	114
Figure C.7:	Mean a.) global and b.) SAB wave parameters for the 31 year scenarios.	115

Figure C.8: Ice cover percentage over 31 year simulation .....116

## **ABSTRACT**

The loads and forms of nutrients, metals, and carbon in coastal seas have impacts on nearshore marine ecosystems. These solutes can undergo biogeochemical transformations in the shallow seabed aquifer, which is controlled by chemistry in surface water and groundwater and the benthic exchange that drives this mixing. This dissertation focuses on quantifying the effect of waves on ambient groundwater discharge, understanding how wave pumping compares to other driving mechanisms, and understanding how wave-induced benthic exchange varies on second-to-decadal temporal scales and spatial scales ranging from meters to the globe.

A laboratory study on the influence of waves on seepage meter measurements confirmed the utility of and quantified potential uncertainties associated with seepage meters. Tank tests showed seepage meters were efficient in measurement of both ambient discharge and recharge. Results of wave tank tests indicated that although waves did induce some net discharge through the seepage meter, measured fluxes were well below the theoretical rates expected for waves traveling over a flat seabed.

A field and modeling study investigated how wave, current/bedform, and tidally-induced benthic exchange compare and how these fluxes vary over time at a shallow estuarine location. Field measurements showed wave-induced exchange greatly exceeded exchange driven by currents or tides over the study duration. Darcy-calculation of fluxes from high-resolution pressure measurements were used to validate an analytical solution with field measurements of wave pumping for the first time. Results of the numerical models showed the effect of aquifer properties on benthic

exchange—seabed aquifers with low hydraulic diffusivity had higher fluxes, shallower exchange, and shorter residence times.

A global modeling study quantified the rates and temporal and spatial variability of wave pumping over the Earth's oceans. Global wave pumping between 1979 and 2010 averaged  $1.8 \times 10^5 \text{ km}^3/\text{yr}$ , which is equivalent to an average of 6.1 m/yr over the entire global shelf area. Seasonally, winter wave pumping rates exceed summer values by about one-third except in the circumpolar oceans where ice-cover drastically reduces wave pumping during winter months. Results of a regional analysis showed that extreme (top 10%) of wave pumping events drive about one-fifth of annual wave pumping.

These studies provide better estimates of wave pumping rates on a variety of scales and quantify the uncertainties associated with measurement of benthic exchange in the presence of waves. Thus, the findings have important implications for understanding chemical cycling in the seabed aquifer and, thus, for management of coastal ecosystems, and preservation of the recreational and economic resources they provide.

## Chapter 1

### INTRODUCTION

#### 1.1 Problems in Coastal Seas

Increased pollution in coastal seas has been accompanied by degradation of coastal ecosystems around the globe. This continuing degradation is expected to increase unless pollutant loads can be reduced, especially nutrients, which are among the most globally widespread pollutants. However, nutrient loading is predicted to increase in the future. For instance, nitrogen loads are expected to increase over much of the world because of continuing population growth and land use changes [e.g., Vitousek et al., 1997; Seitzinger et al., 2009]. Increased nutrient loads in the last century have led to eutrophication of coastal seas and estuaries, which in turn resulted in decreased biodiversity, blooms of toxic algae, reduced oxygen concentrations, and loss of fisheries and fishkills in dead zones. While it is clearly important to accurately measure nutrient loads, and to understand their fate once they reach coastal seas, nutrients are especially difficult to measure because of the complex physical and biochemical pathways nutrients travel through in coastal settings.

Rivers and fresh, terrestrial submarine groundwater discharge (SGD) carry the bulk of terrestrial nutrients to global seas [Vitousek et al., 1997]. While SGD volumes are typically less than river discharge groundwater, elevated solute concentrations in groundwater result in SGD often contributing a disproportionately high percentage of nutrients and other solutes to coastal waters compared to rivers. In the Delaware Inland Bays, where topographic relief is low and aquifer permeability is high, about one-third of recharge discharges as SGD [Russoniello et al., 2016] and groundwater discharge accounts for greater than 50% of the total nitrogen load [Volk et al., 2005]. A review of

regional studies by Slomp and Cappellen [2004] showed this trend is widely true—nitrogen and phosphorous loads in fresh SGD frequently exceed river loading. A recent global study that combined a global  $^{228}\text{Ra}$ -based SGD estimate with a global nutrient dataset found SGD carries 1.4 times more dissolved inorganic nitrogen (DIN) and 1.7 times more dissolved inorganic phosphorous (DIP) than rivers [Cho et al., 2018]. Effective nutrient management for protecting coastal ecosystem health requires accurate estimates of both loading and source, including spatial and temporal variability. Thus, it is critical to improve our understanding of the factors that promote reduction or increase of nutrients or other contaminant loads prior to discharge or may help to mitigate or exacerbate nutrient loads once they reach marine waters.

## **1.2 Role of FSeabed Aquifers in Chemical Cycling**

Nonconservative transport along groundwater flowpaths is caused by biogeochemical transformations in coastal and marine aquifers [Sawyer et al., 2014; Russoniello, 2016; Fernandez, 2012; Kroeger and Charette, 2008; Spiteri et al., 2008; Santoro, 2008; Heiss et al., 2017]. These transformations may reduce (i.e. through denitrification) [Tobias et al., 2001; Charette, 2007] or increase (i.e. by mobilizing ammonium produced by decomposition of organic matter) [Kroeger and Charette, 2008; Santoro, 2008] concentrations of different chemical species in groundwater prior to discharge. These changes are stimulated by mixing with marine water near the point of discharge [e.g. Robinson et al., 2007; Heiss et al., 2017], so they depend on both the chemistry of ground and surface waters as well as the rate of exchange between surface water and groundwater in shallow seabed aquifers. Therefore, coastal nutrient chemistry cannot be understood without understanding the mechanisms that drive such exchange.

Reactions affecting solute loading to surface waters are particularly prevalent in shallow seabed sediments where groundwater and surface water mix, creating ‘hot spots’ and ‘hot moments’ of biogeochemical activity that may transform nutrients prior to

discharge [McClain et al., 2003; Roy et al., 2012]. The extent of biogeochemical transformation that occurs in this active zone is controlled by the supply of reactants from upwelling groundwater, sediments, and surface water driven into the benthic zone, as well as the reaction timescale and residence time of surface water in the benthic zone [Zarnetske et al., 2011; Gu et al., 2012; Harvey et al., 2013; Gomez-Velez et al., 2015]. These factors are a function not only of groundwater and surface water chemistry, but also, just as importantly, on the physical mechanisms that drive benthic fluxes and the resulting subsurface flowpaths. Therefore, characterizing these fluxes – the rates, residence times, and depths of exchange – and how they vary in time and space is a necessary precursor to understanding chemical processing in the seabed aquifer.

### **1.3 Benthic Exchange Mechanisms in Coastal Seas**

Benthic flux in marine and estuarine waters may be driven by a wide variety of mechanisms, many of which have been studied and modeled [see reviews in Huettel and Webster, 2001; Boudreau et al., 2001; Santos et al., 2012]. For instance, Santos et al. [2012] discusses 12 mechanisms that drive benthic flux, and there are others, including tidal pumping [e.g. Wang and Davis, 1996; Sawyer et al., 2013] and density-bathymetry interactions [Konikow et al., 2013]. Most of these mechanisms are present in both limnic and marine environments. The fluxes associated with each mechanism vary in time and space [e.g. Riedl et al., 1972; Sawyer et al., 2013], and different drivers operate over different spatial scales. While these drivers may play important roles in particular settings, wave pumping, and currents-over-bedforms have been identified as the most important drivers of benthic exchange in coastal settings [e.g. Santos et al., 2012; Sawyer et al., 2013].

Coastal currents driven by tides, wind, and waves drive benthic flux by interacting with seabed bathymetry. This process has been investigated mostly in streams [e.g. Cardenas and Wilson, 2006; Cardenas and Wilson, 2007], but unlike currents in fluvial

environments, coastal currents change direction periodically as tides and winds change, which affects bedform shape. Pressure gradients induced by currents drive recharge in bedform troughs and discharge at peaks with exchange depths approximately equal to one bedform wavelength [Cardenas and Wilson, 2007; Elliott and Brooks, 1997; Thibodeaux and Boyle, 1987].

Surface gravity waves drive benthic exchange in coastal environments. Waves interact with bathymetry to drive recharge in the troughs between bedforms and discharge near bedform peaks [e.g. Huettel et al., 2003; Webb and Theodor, 1968; 1972].

Topography enhances wave-induced benthic flux across beds [Precht and Huettel, 2003], but wave-driven exchange also occurs over a flat seabed. In this mechanism, pressure oscillations associated with the peaks and troughs of surface gravity waves propagate along the seabed, which create pressure gradients in the aquifer that drive flow from high-pressure regions beneath wave crests to low-pressure regions beneath wave troughs [e.g. Reid and Kajiura, 1957; Riedl et al., 1972; King et al., 2009].

#### **1.4 Methods to Quantify Benthic Exchange**

Benthic exchange rates have been measured in laboratory and field experiments, quantified with numeric models, and calculated from analytical solutions. Each of these methods has strengths and weaknesses, and each plays a role in achieving a greater understanding of benthic exchange and its effect on chemistry in coastal waters.

Field and laboratory experiments permit measurement of the actual exchange process but are limited by the equipment and methods used in these measurements. Measuring these fluxes is difficult because relatively slow velocities and the short length and time scales of most exchange mechanisms necessitate high-resolution measurement equipment. Even with sensitive equipment, uncertainties may still be high. Nevertheless, a number of laboratory and field studies have successfully quantified rates, depths or residence times of benthic exchange driven by current-bed interaction [e.g. Elliott and

Brooks, 1997; Sawyer et al., 2011], waves [e.g. Yamamoto et al, 1978; Precht and Huettel., 2004], and other mechanisms. Field observations may help to identify processes. For instance, boils in surface water can indicate advective groundwater discharge [e.g. Moosdorf and Oehler, 2017], and wave pumping was initially considered following observations that seabed sediments were more oxic than could otherwise be explained [Riedl et al., 1972].

Numerical models allow investigation of different exchange mechanism alone or together and are especially useful to understand systems that cannot be measured in the laboratory or field. Examples include effects of heterogeneity [e.g. Sawyer and Cardenas, 2009], interacting mechanisms [e.g. Cardenas and Wilson, 2006], mechanisms with fluxes below sensor limits [e.g. Konikow et al., 2013], and a parameters range beyond what could be tested in a lab setting [e.g. Shum, 1992]. These models can vary in complexity to consider different governing equations, boundary conditions, and seabed morphology and aquifer characteristics. They can also be combined with chemistry models to understand reactive transport in the seabed aquifer [e.g. Shum, 1993; Cardenas et al, 2008; Bardini et al., 2012].

Analytical models are generally the easiest method to quantify benthic exchange rates, as they are typically based on hydrodynamic and seabed parameters that are relatively easy to measure. Analytical solutions have been developed to describe most of these benthic exchange drivers. For instance, wave-induced exchange may be calculated from wave parameters, water depth, and aquifer characteristics [e.g. Mu et al., 1999; King et al., 2009]. Analytical solutions are also generally relatively easy to solve, though some require numerical solution [e.g. Mu et al., 1999]. Analytical models must also be validated against field and numerical studies to confirm their veracity. These solutions consider fewer system characteristics, which may yield greater uncertainty than more complex numerical models. A strength, though, is that the simplicity of these models permits calculate benthic exchange rates over much larger areas than would be possible

with field measurements or numerical models [e.g. Riedl et al., 1972; King et al., 2012; Sawyer et al, 2013]. Results from these large-area models allows scientists and managers to place benthic exchange in the context of the larger system and to more accurately understand the effect of chemistry over a large area.

### **1.5 Broader Significance**

Exchange of water through the benthic zone is a significant and dynamic component of estuarine fluid budgets that directly influences chemistry of surface water and groundwater. Quantifying benthic exchange rates and patterns is critical for understanding and managing processes that promote healthy coastal ecosystems.

## Chapter 2

### **INVESTIGATION OF SEEPAGE METER MEASUREMENTS IN STEADY FLOW AND WAVE CONDITIONS**

This work has been published as Russoniello, C. J. and Michael, H. A. (2015), Investigation of Seepage Meter Measurements in Steady Flow and Wave Conditions. *Groundwater*, 53: 959–966. doi:10.1111/gwat.12302  
Copyright © 2015 National Ground Water Association

#### **ABSTRACT**

Water exchange between surface water and groundwater can modulate or generate ecologically important fluxes of solute across the sediment-water interface. Seepage meters can directly measure fluid flux, but mechanical resistance and surface water dynamics may lead to inaccurate measurements. Tank experiments were conducted to determine effects of mechanical resistance on measurement efficiency and occurrence of directional asymmetry that could lead to erroneous net flux measurements. Seepage meter efficiency was high (average of 93%) and consistent for inflow and outflow under steady flow conditions. Wave effects on seepage meter measurements were investigated in a wave flume. Seepage meter net flux measurements averaged 0.08 cm/hr—greater than the expected net zero flux, but significantly less than theoretical wave-driven unidirectional discharge or recharge. Calculations of unidirectional flux from pressure measurements (Darcy flux) and theory matched well for a ratio of wave length to water depth  $<5$ , but not when this ratio was greater. Both were higher than seepage meter measurements of unidirectional flux made with 1-way valves. Discharge averaged 23% greater than recharge in both seepage meter measurements and Darcy calculations of unidirectional flux. Removal of the collection bag reduced this net discharge. The presence of a seepage meter reduced the amplitude of pressure signals at the bed and

resulted in a nearly uniform pressure distribution beneath the seepage meter. These results show that seepage meters may provide accurate measurements of both discharge and recharge under steady flow conditions and illustrate the potential measurement errors associated with dynamic wave environments.

## 2.1 Introduction

Water exchange between surface water and groundwater in saline and fresh environments impacts ecologically important solute fluxes (e.g. Johannes 1980; Slomp and van Cappellan 2004; Moore 2010). Measurement of these fluxes can be difficult because fluid and solute discharge patterns are heterogeneous (e.g. Michael et al. 2003; Rosenberry 2005; Rosenberry and Pitlick 2009), and discharge rates vary on temporal scales of seconds to decades (e.g. Anderson and Emmanuel 2010; Smith et al. 2009; Rosenberry et al. 2012; Sawyer et al. 2013). However, accurate measurements are critical for quantifying fluid and solute fluxes. Indirect methods are often used to estimate groundwater-surface water exchange (see e.g. Burnett et al. 2006; Rosenberry et al. 2008). Methods include naturally-occurring tracers such as salinity (Ganju 2011),  $R_a$  and  $R_n$  (e.g., Corbett et al. 1997; Burnett and Dulaiova 2003), temperature (e.g. Johnson et al. 2008; Henderson et al. 2009), Darcy calculations from in situ pressure measurements (e.g. Woessner and Sullivan 1984; Gardner et al. 2009; Kennedy et al. 2010), and subsurface electrical resistivity measurements (Stieglitz et al. 2008). The only method to directly measure these fluxes is with a seepage meter (e.g. Lee 1977; Rosenberry et al. 2008). Seepage meters are inexpensive, enabling deployment at multiple locations for characterization of spatial and temporal distributions of water and conservative solute fluxes.

Despite the utility of seepage meters, they can incur measurement error. Resistance, or head loss, through the seepage meter results in reduced *mechanical efficiency*: the percentage of the true flow that a seepage meter measures. Mechanical

efficiency measured in laboratory tests ranges from 57% (Erikson 1981) to 95% (Rosenberry and Menheer 2006). Flux asymmetry results when mechanical efficiency is greater for groundwater discharge than recharge (e.g. Lee 1977; Erikson 1981). Such asymmetry could partially explain higher rates of saline discharge than recharge often measured in the field (e.g. Michael et al. 2005; Martin et al. 2007; Santos et al. 2009), despite the expectation that these components of recirculated sea water should balance over some spatial and temporal scale.

Wave and current interactions with seepage meters can drive excess flux that would not exist in calm waters (e.g. Cable et al. 1997; Rosenberry 2008; Smith et al. 2009), leading to questions about seepage meter accuracy in dynamic surface waters (e.g. Shinn et al. 2002; King et al. 2009; Rosenberry et al. 2013). Though effects of currents on seepage meter measurements have been studied and quantified in a controlled laboratory setting (Libelo and MacIntyre 1994; Rosenberry 2008), wave impacts have not received similar attention. Wave-driven flux across the sediment-water interface (hereafter the *bed*) has been measured in the field at frequent intervals (seconds) (Smith et al. 2009), but over longer time scales (hours), wave height and net flux do not appear to be correlated (e.g. Cable et al. 2006). However, concurrent forces that could contribute additional flux, such as current-bed interactions or pumping by marine fauna cannot be controlled for in the field. While many studies have investigated wave-induced flux across the bare seafloor (e.g. Webb and Theodor 1968; Yamamoto et al. 1978; King et al. 2009), to our knowledge wave-induced flux into seepage meters has not been investigated in the laboratory.

The goal of this study was to examine seepage meter measurements in the presence of steady groundwater flow and surface water waves. The objectives were to: (1) determine the magnitude and asymmetry of mechanical efficiency of Lee-type seepage meters (Lee 1977) used by the authors in this and other studies and (2) determine

seepage meter-measured fluxes in the presence of waves and compare them to those calculated from pressure gradients and an analytical model.

## **2.2 Methods**

### **2.2.1 Seepage Meter Design**

Seepage meters constructed from ends of 55-gallon steel drums (57 cm diameter, 15 cm height) (see Russoniello 2012 for description) were installed with 5 cm headspace above the bed. Plumbing supplies and quick-connect fittings (minimum inner diameter (I.D.) of 0.95 cm) were used to attach 61 cm x 76 cm 2 mil thick polypropylene autoclave collection bags (approximately 40 L capacity), which were selected for durability and to minimize effects of bag rigidity and elasticity noted by Murdoch and Kelly (2003). Collection bags were purged of air after they were prefilled with water to minimize anomalous inflation (e.g. Shaw and Prepas 1989; Libelo and MacIntyre 1994). The bags were pre-filled with approximately 2 L water when net groundwater discharge was expected. Bags were filled to a capacity that ensured they would not dry (< 10 L) when net groundwater recharge was expected.

### **2.2.2 Tank Experiments**

A series of tank experiments was conducted to determine the mechanical efficiency and asymmetry of the seepage meter design used in this and other studies (Russoniello et al. 2013; Sawyer et al. 2014) over a range of hydraulic gradients in both inflow and outflow directions. The tank, modeled after Belanger and Montgomery (1992) and Rosenberry and Menheer (2006), was constructed from a plastic cylinder (1.52 m diameter x 1.83 m tall; Figure A.1). A circular plywood diffuser (1 cm holes, ~8 cm spacing) was installed 10 cm above the tank bottom. 15 cm coarse (crushed) gravel, 15 cm of fine (pea) gravel, and 60 cm sand were placed on top. Inlets/outlets through the tank walls were installed below the diffuser and above the sediment. A bucket hung

outside the tank was connected to the bottom inlet by a hose. A constant head was maintained in both the tank and bucket. In recharge experiments, tap water was allowed to overflow the tank and the bucket was lowered below the tank water level. In discharge experiments, tap water was allowed to overflow the bucket and the bucket was raised above the tank water level. The hydraulic gradient was controlled by changing the bucket elevation and was measured between the tank water surface and water level in a manometer tapped into the tank beneath the diffuser. Flux through the entire tank was measured by collecting discharge from the tank over a given time period – from the tank overflow pipe for discharge experiments and the bucket for recharge experiments (see Figure A.1). The flux through the tank was compared to flux through seepage meters to calculate a mechanical efficiency ( $E_m$ ):

$$E_m = 100\% \times \left( \frac{q_{sm}}{q_{tank}} \right), \quad (2.1)$$

where  $q_{sm}$  is flux per unit area measured by seepage meter and  $q_{tank}$  is flux per unit area through the tank.

### 2.2.3 Wave Flume Experiments

Flume experiments were conducted to measure wave-induced water exchange across the bed with and without seepage meters in a 20 m (length) x 1.22 m (height) x 1.5 m (width) wave flume (Figure 2.1a; see Orzech and Kobayashi 1997 for flume description). Water depth and wave characteristics associated with each experiment are hereafter called *wave parameter sets*. A sand layer thickened from zero at the offshore end to approximately 70 cm at the onshore end. Wave-driven flux across the bed was determined near the flume midpoint (30 cm sand depth) using three methods: seepage meter measurement, calculation of *Darcy flux* from measured pressure gradients, and calculation from theory. The unidirectional, phase-averaged, theoretical wave-driven flux at a point along a flat planar bed can be calculated from King et al. (2009) as:

$$q_{th} = \frac{2Ka \tanh \frac{2\pi d}{L}}{L \cosh \frac{2\pi h}{L}} \quad (2.2)$$

where hydraulic conductivity (K), wave amplitude (a), wave length (L), water depth (h), and impermeable layer depth (d) are known (Figure 2.1a & d; Table 2.1).

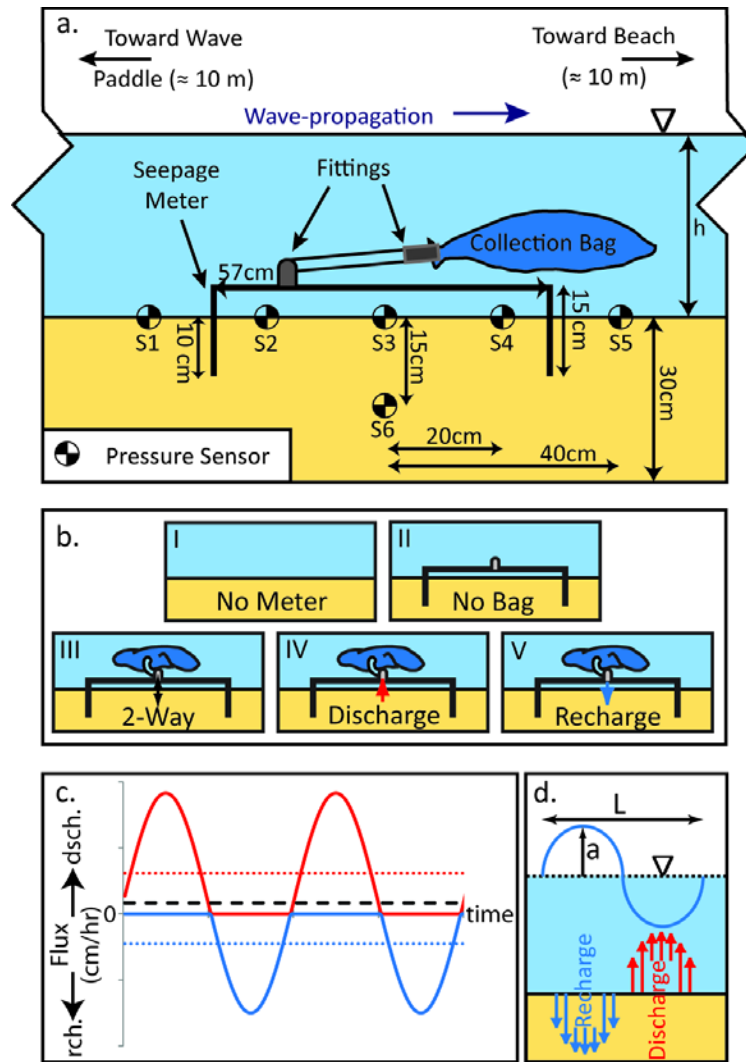


Figure 2.1: Wave flume experimental set-up and wave-induced flux. a) Cross sectional schematic of wave flume with seepage meter and pressure sensors installed. b) Five seepage meter configurations (I-V). c) Diagram of terminology as illustrated by hypothetical data. Instantaneous flux is shown as solid red and blue lines, which are discharge and recharge components, respectively. Unidirectional flux ( $q$ ) is the discharge or recharge component of flux averaged over multiple wave periods, plotted as dotted red and blue lines, respectively. Net flux is the period-averaged sum of the discharge and recharge flux components, plotted as a bold dashed black line. These hypothetical data illustrate an asymmetric scenario where discharge is greater than recharge. d) Diagram of wave parameters and location of recharge and discharge beneath a surface wave (adapted from King et al. 2009).

Five wave parameter sets (A-E) (Table 2.1) with four unique values of non-dimensional wave length ( $L_w = L/h$ ) were chosen to span  $L_w = 5.2$ , the value associated with maximum theoretical flux (Equation 1.2). In two wave parameter sets  $L_w$  was equivalent but amplitude differed. For each wave parameter set, experiments were run with five configurations: no seepage meter (*bare bed*) (I), a seepage meter with no collection bag (II), a seepage meter with a collection bag (III), and a seepage meter and collection bag with an in-line 1-way valve ( $66\% \pm 2\%$  efficiency; Appendix S1) oriented to capture discharge (IV) or recharge (V) only (Figure 2.1b). Configurations IV and V were suggested by King et al. (2009). *Net flux*, *unidirectional* discharge, and *unidirectional* recharge were measured with seepage meters in configurations III, IV and V, respectively (Figure 2.1c). The average value of 2 duplicate experiments (one for one hour and another for one-half hour) is reported for each wave parameter set. In 2 of 20 experiments, the 1-way valve malfunctioned and the experiment was re-run.

All 25 flume experiments (configurations I-V with wave parameter sets A-E) were also run for 7.5 minutes to measure pressure gradients. The differential pressure between six locations in the wave flume (Figure 2.1a) and an outside container with a water level equal to the still-water level of the flume (established by siphon after every calibration) was measured. The pressure difference between the ends of water-filled 0.16 cm I.D. polyethylene vacuum tubing was measured with Validyne DP 15 sensors linked to a Validyne CD280 dual voltage modulator. The polyethylene tubing was routed through the sediment to the side wall of the flume to avoid interference that could affect measurements. Raw voltage was recorded at 20 Hz with a DATAQ DI-149 data recorder connected to a Windows PC. Voltage was converted to pressure by applying slope and intercept calibration values, which were determined daily or when measured still water levels between experiments had drifted. Pressure was measured by two sensors at the seepage meter center (S3 at the bed and S6 15 cm beneath the bed) and four sensors (S1, S2, S4, and S5) located along the bed 20 cm and 40 cm ahead of and behind the seepage

meter center (Figure 2.1a). Flux was calculated for each 20 Hz measurement interval (hereafter *instantaneous flux*; Figure 2.1c) from the measured pressure gradient between S3 and S6 and sediment K ( $2.1 \times 10^{-4} \pm 3.8 \times 10^{-6}$  m/s; Appendix S1) using Darcy’s Law. This measurement of pressure difference across the top 15 cm likely somewhat underestimates flux since it is driven by the pressure gradient at the bed surface and the gradient decays with depth. This error varies across experimental conditions since the pressure signal decay with depth is dependent on wave parameters (e.g., Smith et al., 2009). Unidirectional recharge and discharge components of Darcy flux were calculated as the average of the discharge or recharge component of flux over the 7.5 minute experiment (Figure 2.1c).

There was an observed difference in bare-bed pressure wave amplitude among the five sensors (Figure 2.1; configuration I). While we would expect these bare-bed measurements to have a phase-offset, we would not expect measured the pressure wave amplitude and wavelength to vary among sensors. We interpret the discrepancies as measurement error, though there could be small spatial differences in amplitude. The average deviation from the mean amplitude for the 5 sensors ranged from -25% to 29%. However, the deviation from the mean for each sensor was consistent over the experiments (differing across experiments by only 7% on average). Because we compare only across seepage meter configurations (not between sensors), we do not expect that these differences significantly affected the comparisons. However, the differences do affect the absolute Darcy flux measurements.

Table 2.1: Characteristics of the five wave parameter sets (A-E) in wave flume experiments.

<b>Wave Parameter Set</b>	<b>Symbol</b>	<b>Unit</b>	<b>A</b>	<b>B</b>	<b>C</b>	<b>D</b>	<b>E</b>
<b>Wave Period</b>	T	<i>s</i>	1.00	1.00	1.00	1.30	1.75
<b>Wave Amplitude</b>	a	<i>m</i>	0.052	0.049	0.032	0.045	0.036
<b>Mean Water Depth</b>	h	<i>m</i>	0.305	0.270	0.270	0.270	0.270

<b>Wave Length</b>	L	<i>m</i>	1.38	1.33	1.33	1.89	2.68
<b>Relative Wavelength</b>	$L_w = L/h$	-	4.52	4.92	4.92	7.00	9.92

## 2.3 Results

### 2.3.1 Tank Experiments

The mean mechanical efficiency of the three seepage meters (Equation 1.1) was  $98\% \pm 16\%$ ,  $75\% \pm 9\%$ , and  $105\% \pm 18\%$  (overall mean = 93%) over the range of hydraulic gradients (Figure 2.2). Because seepage meters were constructed with identical materials and efficiency was greater than 100% in some cases, we infer that much of the variability was due to sediment heterogeneity, which is consistent with previous tank studies (e.g. Belanger and Montgomery 1992; Rosenberry and Menheer 2006) and field studies (e.g. Michael et al. 2003; Cardenas et al. 2004; Rosenberry 2008). The significant effect of heterogeneity even in controlled tank experiments highlights the need for multiple seepage meters to characterize average flux in field investigations.

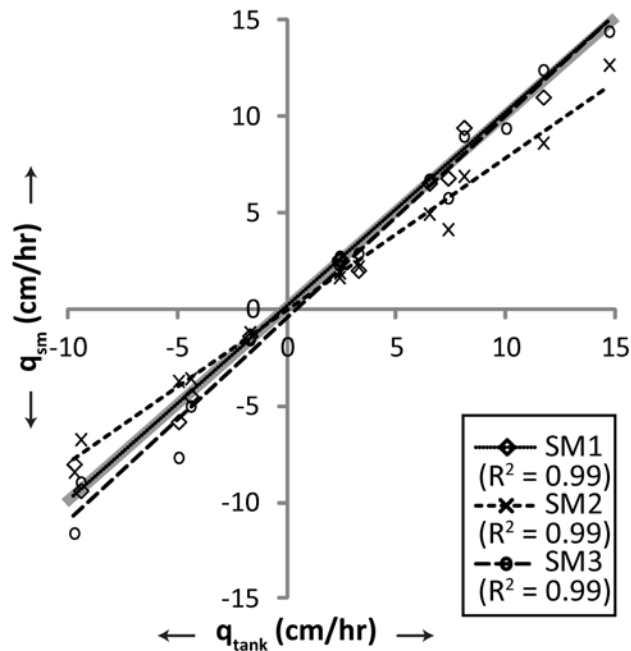


Figure 2.2: Measured flux through three seepage meters (SM1-SM3) and the tank for 14 values of hydraulic gradient. The slope of the regression lines are the seepage meter efficiency. Corresponding correlation coefficients ( $R^2$ ) values are shown in the legend. Heavy grey line is the 1:1 line representing a seepage meter efficiency of 100%.

Mechanical efficiency was consistent for individual seepage meters across the range of positive and negative hydraulic gradients (Figure 2.2). A t-test to determine whether the slope of mechanical efficiency vs. hydraulic gradient (determined by linear regression) was non-zero was rejected at the 95% level of significance. A t-test to determine whether the slope of mechanical efficiency vs. hydraulic gradient was different for values with positive and negative hydraulic gradients was rejected at the 99% level of significance. Thus, mechanical efficiencies were consistent across the range of tested hydraulic gradients and symmetric for inflow and outflow.

## **2.3.2 Wave Flume Experiments**

### **2.3.2.1 Seepage Meter Measurements of Wave-Induced Flux**

The net wave-driven flux measured by seepage meters should be zero since recharge should equal discharge. At high  $L_w$  values, net seepage meter discharge was at or near zero. However, in a few cases low net discharge was observed, with an overall average of 0.08 cm/hr (range of 0.0 to 0.2 cm/hr; Figure 2.3a). While this net flux can be considered an error or anomalous measurement, it is on average 6.5% of the wave-driven recharge or discharge as predicted by theory (Figure 2.3a). Thus, the seepage meter is not measuring only the discharge component of flow, and theoretical flux would be a high upper bound on wave-induced error.

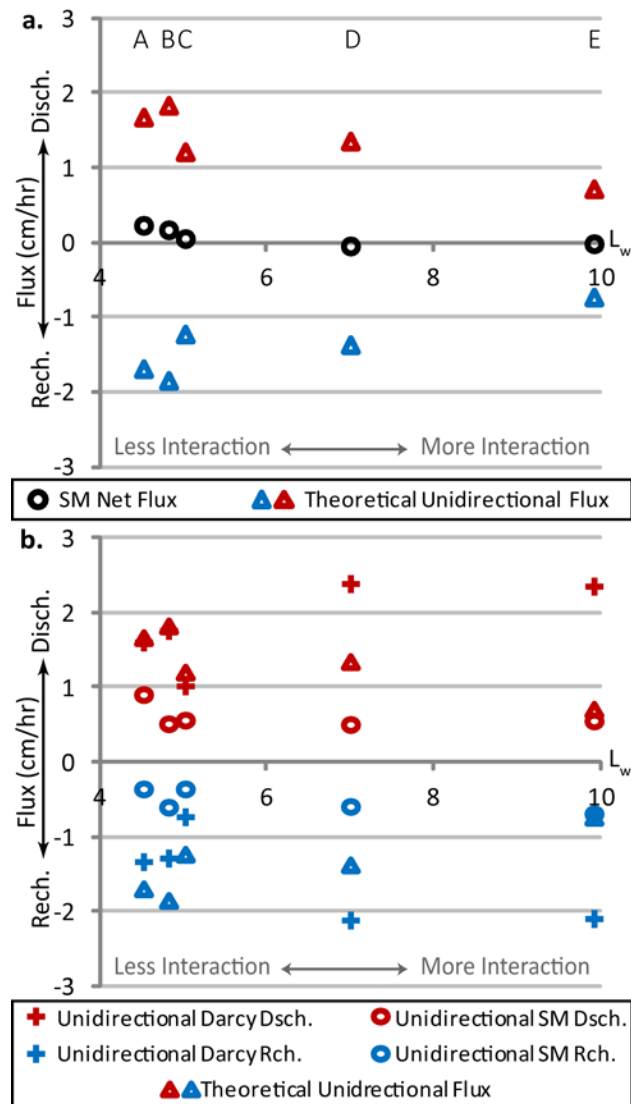


Figure 2.3: Flume experiment data. a) Net flux measured with a seepage meter (SM) and unidirectional flux predicted by theory. b) Unidirectional flux obtained from pressure gradients (Darcy flux), seepage meter measurements, and theory. Letters at top denote the wave parameter set. Note that two wave parameter sets (B and C) have  $L_w$  values of 4.92, but are offset for clarity.

### 2.3.2.2 Comparison of Methods to Measure Unidirectional Flux

There were differences in unidirectional flux measured and calculated by the three methods (Figure 2.3b). Unidirectional fluxes calculated from vertical pressure gradients matched theoretical values well for low  $L_w$ , but were much larger for high  $L_w$ , conditions for which longer wavelengths relative to water depth likely resulted in greater disturbance

to surface wave orbitals (*more interaction* in Figure 2.3). Unidirectional fluxes measured by seepage meters with 1-way valves were always less than Darcy and theoretical unidirectional fluxes (37% and 46%, respectively). All three methods consistently yielded fluxes in the same direction. Wave-driven unidirectional discharge should theoretically equal recharge, but discharge averaged 23% greater than recharge in both seepage meter measurements and Darcy fluxes with a seepage meter (configuration III). Darcy-calculated discharge was 33% greater than recharge across a bare bed (configuration I).

We note that the 1-way valves likely induced measurement error. The presence of the 1-way valve disrupted the pressure beneath the seepage meter. This changed the flow system, causing flow to be diverted into or out of the seepage meter, depending on the configuration. This disruption, combined with the valve inefficiency (see Appendix S1) indicates that these 1-way valves are not ideal for characterizing 1-way fluxes with seepage meters.

### **2.3.2.3 Effect of the Seepage Meter on Pressure and Flux Across the Bed**

The seepage meter affected pressure along the bed beneath it. The amplitude of pressure fluctuations inside the meter (S2, S3 and S4; Figure 2.1a) was on average 9% less and Darcy flux 13% less than along a bare bed for the same wave conditions. The presence of a seepage meter also reduced the spatial variation in pressure beneath it, observed as a reduced temporal phase offset in the pressure sensors. The phase offsets at S2 and S4 relative to S3 over a bare bed were -0.25 s and -0.16 s on average, respectively. However, beneath a seepage meter, the offsets were reduced to nearly zero—averages were -0.07 s and 0.00 s at S2 and S4, respectively. This indicates that the pressure along the bed inside the seepage meter was nearly uniform at a given time. The presence of the collection bag also affected measurements. The skew measured with the pressure sensors was greater with a bag attached; discharge exceeded recharge by 7% without a bag and 23% with the bag.

## 2.4 Discussion

Our measurements show that waves can induce anomalous net flow into seepage meters. These fluxes may be near zero or within measurement error, which is approximately 0.02 cm/hr for a two-hour measurement period for the scales used in this study. Measured wave-induced net fluxes (average 0.08 cm/hr) were similar in magnitude but less than field measurements made with the same seepage meters (values averaged 0.5 cm/hr in Russoniello et al., 2013 and 0.3 cm/hr in Sawyer et al., 2014) and with other seepage meters in a range of settings (see review in Taniguchi et al. 2002). Conditions during field deployments with our seepage meters were much lower energy than flume conditions (5 cm amplitude waves in 30 cm of water for the case with the greatest net flux). In other field studies, wave heights often exceed those in the flume experiments [e.g. Cable et al., 2006; Smith et al., 2009]. However, water depths are generally also greater [e.g. Lee, 1977; Cable et al., 2006; Santos et al., 2009]. Because wave amplitude and water depth have opposite effects on wave-driven flux, these factors tend to offset.

Anomalous net wave-induced flux may result if mechanical efficiency varies with either flux magnitude or direction. Waves become non-sinusoidal in shallow water ( $h < \frac{1}{2}L$ ) with peaks that are larger and of shorter duration compared to troughs. Beneath such waves, a seepage meter with reduced mechanical efficiency at greater fluxes would preferentially impede recharge, resulting in a net discharge measurement. Greater efficiency in the discharge compared to recharge direction (as would occur if the collection bag collapsed over the tube, for example; e.g. Asbury 1990) would also result in net discharge measurement in spite of net-zero actual flux. Tank experiments demonstrated that our seepage meters were not prone to these mechanical inefficiencies in still water, but such inefficiencies may occur in more dynamic settings and have been observed in other studies (e.g. Lee 1977; Erikson 1981).

Mechanical efficiency is impacted by seepage meter design. Mechanical efficiency was relatively high for the seepage meters used in this study (see compilation

in Rosenberry and Menheer 2006), likely because the large I.D. hose and fittings used in construction reduced head loss and turbulence (e.g. Rosenberry et al. 2008). The Reynold's Number ( $Re$ ) for flow in the hose fittings is:

$$Re = \frac{4 q A_{sm}}{\pi \nu D_F} \quad (2.3)$$

where  $q$  is the flux across the bed within the seepage meter area,  $A_{sm}$  is the seepage meter area,  $D_F$  is the hose fitting inner diameter, and  $\nu$  is the kinematic viscosity of the water. In the wave flume, the flow rate through the 0.95 cm I.D. seepage meter outflow tubes was always below the 28 cm/hr required to ensure laminar flow ( $Re < 2300$ ; White 2003). In studies where seepage meters had smaller 0.56 cm I.D. fittings (e.g. Erikson 1981; Belanger and Montgomery 1992), flow must remain below 16 cm/hr, which is close to the maximum instantaneous flux calculated from pressure gradients in our flume experiments (12.5 cm/hr). Because seepage meter design impacts turbulent flow, inner diameters for all hose fittings should be reported.

Anomalous flux may also be caused by interactions between waves and the collection bag. The bags in this study were above wave base in the shallow flume and visibly disturbed by passing waves. Pressure gradients were measurably different with the bag than without it, so it is likely that a bag-related mechanism is partially responsible for the anomalous discharge measurements (possible solutions are discussed in Rosenberry et al. 2008). Collection bag characteristics affect seepage meter measured flux (e.g. Murdoch and Kelly 2003; Libelo and Macintyre 1994), and likely also influence wave-induced artifacts. Such artifacts should be negligible if seepage meters are deployed in deeper water and calm conditions.

In settings where the salinity of discharging water is variable and different from that of the surface water, seepage meters are often used to measure the salinity of the discharging water (e.g. Michael et al. 2005; Mulligan and Charette 2006; Martin et al. 2007). Wave pumping may result in errors in this salinity measurement. In such settings,

often coastal, the salinity of the pre-filled water in the bag is generally different than that of the discharging water, so determination of discharge salinity requires a measurement of both volume and salinity of the bag before and after deployment. The calculation of discharge salinity from these measurements requires two assumptions. The first assumption is that the salinity of water in the seepage meter headspace is equivalent to the salinity of the discharging water. This requires an equilibration period during which groundwater discharging into the seepage meter completely replaces surface water trapped in the headspace during seepage meter installation. Waves may induce mixing between saline surface water and fresher water within the seepage meter headspace during this equilibration period because there is no collection bag to prevent mixing; this could prevent complete equilibration of the headspace. Incomplete flushing would result in measured discharge with salinity higher than the true value. The second assumption is that water pre-filled in the collection bag does not mix back into the headspace during measurement. If waves induce such mixing, and if pre-filled water is more saline than discharging groundwater, measured discharge salinity would be lower than the true value.

## **2.5 Conclusion**

This study shows that (1) these seepage meters are slightly inefficient, but equally so in both recharge and discharge directions under steady-flow conditions, (2) dynamic interactions between waves and a seepage meter induce a small anomalous net flux under some wave conditions that, when measurable, is much less than theoretically-predicted unidirectional fluxes, and (3) wave-induced discharge can exceed recharge, despite the symmetry observed in steady-flow tank experiments. These results provide insight into the utility of seepage meters deployed in field settings, especially coastal environments where waves are common. Improved understanding of seepage meter functioning and wave influence will lead to better interpretation of field measurements and improved

estimation of fluid and chemical fluxes between aquifers and adjacent surface water bodies.

## **2.6 Acknowledgements**

The authors gratefully acknowledge Jeffrey King at the U.S. Geological Survey for insightful suggestions and comments on the experimental design, project findings, and an early version of the manuscript. University of Delaware undergraduate students Matthew Kerezsi and Austen Reichhold assisted with tank and flume experiments. M. Bayani Cardenas (University of Texas at Austin) provided differential pressure transducers, and Audrey Sawyer (now at The Ohio State University) assisted with deployment and gave helpful advice. Nobuhisa Kobayashi and Michael Davidson (University of Delaware) provided access to and assistance with the wave flume. James Heiss, Sean Krepski (University of Delaware), and two anonymous reviewers provided helpful comments that improved the manuscript. This work was funded by the National Science Foundation (EAR-0910756).

## Chapter 3

### **VARIABILITY IN BENTHIC EXCHANGE RATE, DEPTH, AND RESIDENCE TIME BENEATH A SHALLOW COASTAL ESTUARY**

This work has been published as Russoniello, C. J., Heiss, J. W. and Michael, H. A. (2018), Variability in Benthic Exchange Rate, Depth, and Residence Time Beneath A Shallow Coastal Estuary. *J. Geophys. Res. Oceans.* 123. doi:10.1002/2017JC013568  
Copyright © 2018 American Geophysical Union

#### **ABSTRACT**

Hydrodynamically-driven benthic exchange of water between the water column and shallow seabed aquifer is a significant and dynamic component of coastal and estuarine fluid budgets. Associated exchange of solutes promotes ecologically important chemical reactions, so quantifying benthic exchange rates, depths, and residence times constrains coastal chemical cycling estimates. We present the first combined field, numerical, and analytical modeling investigation of wave-induced exchange. Temporal variability of exchange was calculated with data collected by instruments deployed in a shallow estuary for 11 days. Differential pressure sensors recorded pressure gradients across the seabed, and up-and down-looking ADCPs recorded currents and pressures to determine wave parameters, surface-water currents, and water depth. Wave-induced exchange was calculated 1) directly from differential pressure measurements, and indirectly with an analytical model based on wave parameters from 2) ADCP and 3) wind data. Wave-induced exchange from pressure measurements and ADCP-measured wave parameters matched well, but both exceeded wind-based values. Exchange induced by tidal pumping and current-bedform interaction – the other primary drivers in shallow coastal waters was calculated from tidal stage variation and ADCP-measured currents. Exchange from waves (mean = 20.0 cm/d; range = 1.75 to 92.3 cm/d) greatly exceeded

exchange due to tides (mean = 3.7 cm/d) and current-bedform interaction (mean =  $6.5 \times 10^{-2}$  cm/d). Groundwater flow models showed that aquifer properties affect wave-driven benthic exchange: residence time and depth increased and exchange rates decreased with increasing hydraulic diffusivity (ratio of aquifer permeability to compressibility). This new understanding of benthic exchange will help managers assess its control over chemical fluxes to marine systems.

### 3.1 Introduction

Estuaries and coastal seas are ecologically important systems that host diverse biological assemblages and reactive mixing zones driven by land-sea chemical gradients. Seabed sediments host high rates of chemical reactivity, and hydrodynamic mixing of water and solutes between seabed sediments and the overlying water column is an essential control on solute fluxes and reaction rates in these coastal ecosystems. In this work, we describe such mixing as *benthic exchange*, as defined in Boano et al. (2014). The benthic zone reactivity resulting from such hydrodynamic exchange has important effects on carbon and nitrogen cycling [e.g. Shum and Sundby, 1996]. Benthic photosynthesis generates organic carbon at rates that equal or vastly exceed those of the overlying pelagic zone [e.g. Huettel et al., 2014; Nelson et al., 1999] by exploiting the high terrestrial-sourced nitrogen concentrations. On a larger scale, remineralization within sandy coastal sediments may account for 4–13% of total respiration on continental shelves [Huettel et al., 2014], and 44% of global denitrification is hosted within continental shelf sediments [Seitzinger et al., 2006]. Clearly, understanding benthic exchange of fluid and solutes and quantifying the reaction rates accompanying such exchange is crucial for quantifying and managing nutrients and other chemicals in our coastal waters.

Solute reaction rates and removal efficiency are controlled by benthic exchange rate, exchange depth, and the residence time of water in these shallow seabed aquifers

[e.g., Seitzinger et al., 2006]. Benthic exchange rates control the flux of solutes to the benthic exchange zone [e.g. Sawyer, 2015]. Benthic exchange depth, which defines reaction zone volume, is controlled by the length and time scales of the hydrodynamic forcing mechanism [e.g. Jeng et al., 2001; Shum, 1993; Cardenas and Wilson, 2006] as well as the aquifer depth [e.g. Harrison et al., 1983; King et al., 2009] and hydraulic diffusivity [e.g. Jeng et al., 2001; Mu et al., 1999; Ferris, 1952], a ratio relating aquifer permeability to compressibility. Residence times, controlled by benthic exchange rates and depths, determine the time available for reactions to occur – removal efficiency is highest along shallow flowpaths with short residence times when the residence timescale matches the reactions timescale [Harvey et al., 2013; Gomez-Velez et al., 2015]. These three controls all vary with spatial and temporal pressure variations induced by surface water hydrodynamics, which in turn depend on the seabed morphology and hydraulic properties of the shallow aquifer [e.g. Elliott and Brooks, 1997; Reid and Kajiura, 1957; Merritt et al., 2004]. Furthermore, exchange rates are especially high in dynamic estuarine and coastal waters because of shallow water depths and variable bathymetry, dynamic weather and tides, and a highly permeable seabed [e.g. Santos et al., 2012; Sawyer et al., 2013]. Therefore, quantifying these three physical controls – benthic exchange rates, depths, and residence times — is crucial for understanding chemical cycling in coastal waters.

Currents [e.g. Ziebis et al., 1996], tides [e.g. Merritt et al., 2004], and waves [e.g. Thibodeaux and Boyle, 1987], have been identified as major hydrodynamic drivers of benthic exchange in shallow coastal waters. Tidally-induced exchange is easily quantifiable because tides are predictable and easily measured, and the resulting exchange is unidirectional over measurement timescales and relatively uniform in space [e.g. Michael et al., 2003; Sawyer et al., 2013]. Exchange induced by waves and currents is more difficult to quantify because they vary at small spatial and temporal scales that are difficult to measure, and because gross fluxes can be large, though net fluxes are zero

[e.g. Riedl et al., 1972; Santos et al., 2012]. Analytical and numerical models are excellent tools with which to estimate rates of exchange, especially over large areas [e.g. Riedl et al., 1972; King, 2012; Sawyer et al., 2013]. However, these predictions require assumptions that may not always be reasonable, and depend on the available temporal and spatial resolution of field measurements of controlling parameters. These fluxes cannot be directly measured with traditional seepage meters because they cannot resolve the temporal and spatial scales associated with waves, seabed currents, and bedforms [e.g. Rosenberry 2008; Smith et al., 2009; Russoniello and Michael, 2014], though automated seepage meters have resolved wave-induced flux variations at temporal resolutions as short as 15 seconds [Rosenberry and Morin, 2004]. Heat can be used as a tracer to estimate fluxes and exchange depth, but it cannot be used to separate the components of exchange linked to different drivers [e.g. Wilson et al., 2016] and temperature-based methods lack the spatial (centimeters) and temporal (seconds) resolution to resolve exchange from individual waves [e.g. Briggs et al., 2012]. Radioactive tracers such as Ra and Rn are unable to measure benthic exchange because the short residence times associated with the driving mechanisms are less than required to reach tracer equilibrium [e.g. Michael et al., 2011]. Other methods, such as eddy correlation measurements [e.g. Crusius et al., 2008; Berg et al., 2009], can determine chemical fluxes near the seabed, but resolve fluxes on timescales much longer than those of benthic exchange. While fluxes may be determined from accurate measurements of the seabed pressure gradients or water column current velocities, such measurements require high temporal and spatial resolution, and the sensors must incur no large observer effect on the measured pressure gradients—a set of conditions which heretofore has been met only in laboratory conditions [e.g. Yamamoto, 1978; Sawyer, 2011; Russoniello et al., 2015].

Studies have used analytical models informed by environmental data to investigate the relative importance of different benthic exchange mechanisms at estuarine

[e.g. Sawyer et al., 2013] and global [e.g. Santos et al., 2012] scales. However, these estimates have not been based on site-specific field data, as no study has measured the magnitude or temporal variability of wave-induced benthic exchange and its driving forces in the field at any scale. In this study, we calculated benthic exchange rates, depths and residence times from high-resolution measurements of seabed pressure gradients and water column velocity profiles at a typical coastal site. We calculated absolute and relative exchange rates and examined temporal variability in benthic exchange induced by waves, tides, and currents. We also compared a number of different methods to calculate wave-induced benthic exchange in order to assess the accuracy of each in relation to the difficulty and cost of implementation. Finally, we investigated how the parameters most relevant for reactivity - wave-induced benthic exchange depths and residence times - vary with changing environmental conditions using numerical models. Ultimately these findings will inform geochemists and managers about benthic exchange and its effect on coastal chemical cycling and nutrient fluxes.

## **3.2 Background**

### **3.2.1 Field Site**

Indian River Bay, one of the Delaware Inland Bays, is a shallow (<3m depth), microtidal 0<sup>2</sup> (Figure 3.1). The Inland Bays host tourism and fisheries that are economically important to the State of Delaware [e.g. Latham and Lewis, 2012], but the bays have been subject to environmental declines linked to eutrophication due to development of nearby communities and historic and current agricultural activity [e.g. Walch et al., 2016]. Previous studies have characterized the onshore and offshore hydrogeologic system at this site [e.g. Bratton, 2004; Russoniello et al., 2013; Sawyer et al., 2014; Andres et al., 2017].

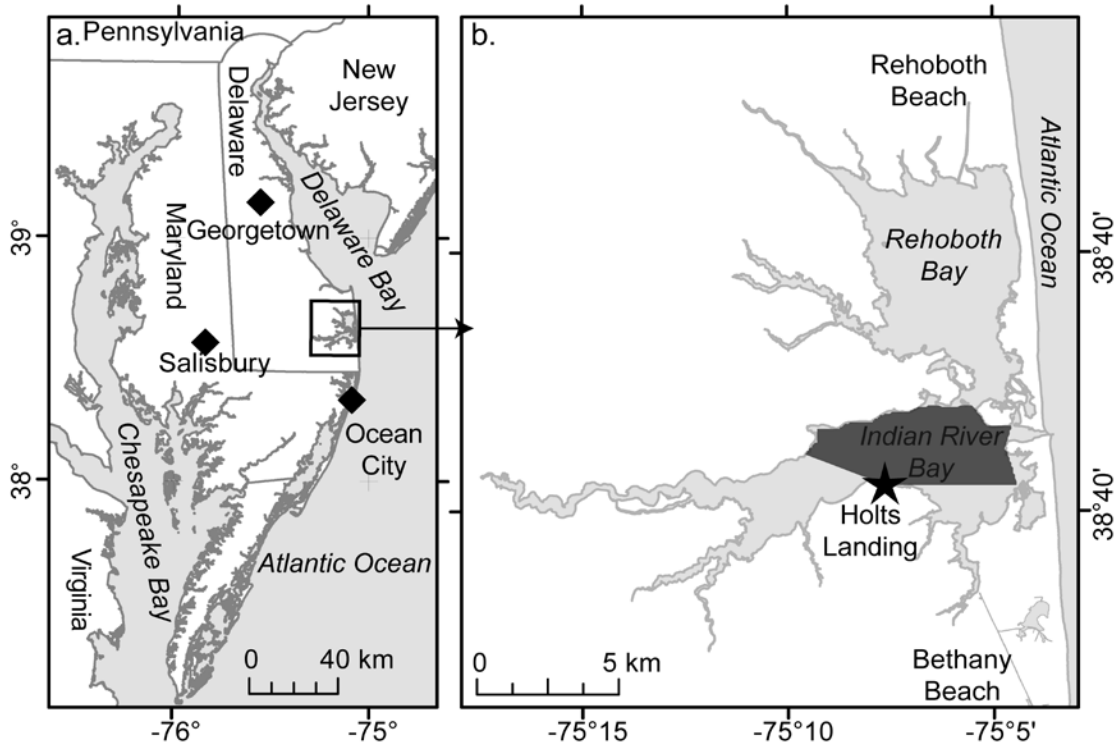


Figure 3.1: Site map. a.) State of Delaware, USA. Diamonds indicate 3 weather stations. b.) Holts Landing field site and vicinity. Star indicates tripod location. Dark shaded region indicates area from which wind fetch reaches tripod.

### 3.2.2 Analytical and Empirical Equations for Calculation of Benthic Exchange Rates

Sawyer et al. [2013] identified waves, current/bedform interactions, and tides as the main physical drivers of benthic exchange in the Inland Bays (Figure 3.2). In this study, benthic exchange due to waves, current/bedform interactions, and tides are quantified using hydraulic gradients calculated from measured pore pressures and by applying measured hydrodynamic and environmental data to analytical and empirical equations. The equations used to calculate the exchange rates are given below.

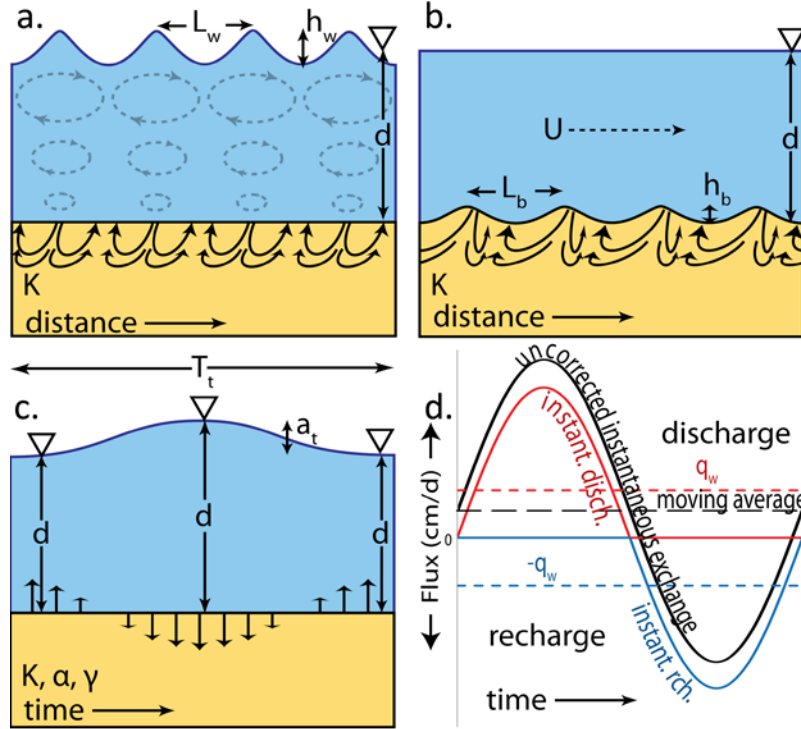


Figure 3.2: Schematic illustrating benthic flux drivers, groundwater flowpaths, and parameters controlling each driver for a.) waves, b.) currents over bedforms, and c.) tidally-induced benthic exchange. d.) Representation of terms used to describe different components of wave-induced benthic exchange. See section 3.1.3 for a description of these terms.

*Waves over a flat seabed* drive surface water into the benthic zone beneath the wave peak (high head) out beneath the wave trough (low head) (Figure 3.2a). An analytical solution for wave-induced benthic exchange ( $q_w$ ) across a flat seabed was developed by King et al. [2009]:

$$q_w = \frac{Kh_w}{L_w \cosh \frac{2\pi d}{L_w}} \quad (3.1)$$

where  $K$  is hydraulic conductivity,  $h_w$  is wave height,  $L_w$  is wavelength, and  $d$  is water depth. Wavelength was calculated using the dispersion equation:

$$\left(\frac{2\pi}{T_w}\right)^2 \approx g \frac{2\pi}{L_w} \tanh\left(\frac{2\pi}{L_w} d\right) \quad (3.2)$$

where  $T_w$  is wave period and  $g$  is gravity.

Wave period and wave height may be estimated from water depth, wind speed ( $W$ ), and fetch ( $X$ ) using empirical equations developed for a lake similar in fetch and depth to the Delaware Inland Bays [Young and Verhagen, 1996]. This approach is similar to that of Sawyer et al. [2013] except that we use measured, rather than modeled, water depths. .

$$T_w = \frac{7.52W}{g} \left[ \tanh(0.331\delta^{1.01}) \tanh\left(\frac{0.0005215\chi^{0.73}}{\tanh(0.331\delta^{1.01})}\right) \right]^{0.37} \quad (3.3)$$

$$h_w = \frac{0.241W^2}{g} \left[ \tanh(0.493\delta^{0.75}) \tanh\left(\frac{0.00313\chi^{0.57}}{\tanh(0.493\delta^{0.75})}\right) \right]^{0.87} \quad (3.4)$$

where  $\chi$  is dimensionless fetch ( $\chi = Xg/W^2$ ) and  $\delta$  is dimensionless water depth ( $\delta = dg/W^2$ ). We used local depth, corrected for tide, rather than fetch-averaged depth, as  $T_w$ , and  $h_w$  were relatively insensitive to water depth over the fetch in this shallow estuary [Sawyer et al., 2013].

**Currents over bedforms** induce flux across the seabed due to the head difference between the up-current and leeward sides of individual bedforms (Figure 3.2b). The amplitude of head variation ( $a_b$ ) due to current passing over periodic bedforms was described empirically by Fehlman [1985]:

$$a_b = 0.28 \frac{U^2}{2g} \begin{cases} \left(\frac{h_b}{0.34d}\right)^{3/8} & h_b/d \leq 0.34 \\ \left(\frac{h_b}{0.34d}\right)^{3/2} & h_b/d \geq 0.34 \end{cases} \quad (3.5)$$

where  $U$  is mean flow velocity in the water column,  $h_b$  is bedform height and  $g$  is gravity. The benthic exchange induced by interactions between currents and bedforms (hereafter: *current-induced*) was described by Elliott and Brooks [1997]:

$$q_b = \frac{2Ka_b}{L_b}, \quad (6)$$

**Tides** induce benthic exchange because the compressible aquifer stores and releases water back to the water column as tides rise and fall (Figure 3.2c). Tide-induced benthic exchange was calculated as [Sawyer et al., 2013]:

$$q_t = 2 \sin\left(\frac{\pi}{4}\right) \frac{a_t K (1-\gamma)}{\sqrt{\pi D T_t}} \quad (3.7)$$

where  $T_t$  is the tidal period,  $a_t$  is the tidal amplitude,  $\gamma$  is the loading efficiency and  $D$  is hydraulic diffusivity ( $K/S_s$ ), where  $S_s$  is specific storage of the aquifer sediments. We assigned a  $\gamma$  of 0.9 as in Sawyer et al. [2013], which is a reasonable value for sediments [e.g. Wang, 2000; Younger, 1993] (Figure B.1).

### 3.3 Methods

#### 3.3.1 Field Instrumentation and Data Collection

##### 3.3.1.1 Seabed Hydraulic Properties

A grain size analysis was performed on 5 seabed sediment samples collected near the tripod. Sediments were collected using a 5 cm x 20 cm bucket auger and were oven-dried at 80 degrees overnight before being sorted with -1, 0, 1, 1.5, 1.75, 2, 2.5, 2.75, and 3 phi sieves. K values for each sample were determined with an Excel spreadsheet, HydrogeoSieveXL [Devlin, 2015], which calculates K from grain size with 15 different methods and informs the user whether the sediment statistics permit the use of each method for that sample. Hydraulic conductivity values calculated from grain size analysis for six sediment samples averaged  $27.5 \pm 4.0$  m/d and ranged from 22.2 to 32.4 m/d (See supplemental appendix A for full analysis results). These values are consistent with the observed medium-coarse nature of the seabed sand [e.g. Fetter, 2001]. We assigned each sample a K value equal to the arithmetic mean K value (27.5 m/d) of all methods and applied the mean of these means as the K value for all calculations and models throughout this study.

### **3.3.1.2 Tripod**

An instrument tripod was constructed and installed offshore of Holts Landing State Park in Indian River Bay, DE, USA to measure surface water wave and current parameters and pressure gradients across the seabed from which benthic exchanges could be calculated (Figure 3.3). The sensor tripod was deployed ~70 m from the coastline in water that averaged ~1 m depth (Figure 3.1, 3.3). Three 3.8 cm diameter 6 m long steel pipes were vibrated 3 m into the seabed to form an equilateral triangular footprint with 2.5 m sides. These 3 pipes were connected by four 3 m horizontal pipes which stabilized the uprights and provided mounting points for sensors. The tripod and associated sensors were deployed and collected data between 16 and 27 October 2014.

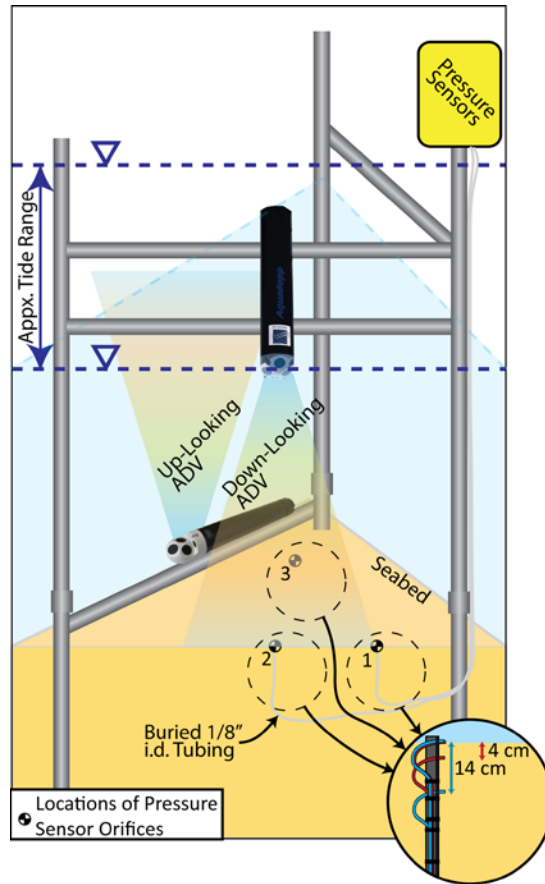


Figure 3.3: Field deployment schematic illustrating tripod components including frame, up- and down-looking ADCPs, six differential pressure sensors within a pole-mounted waterproof case, associated tubing, and locations of tubing orifices. The orifices for two sensors – both a shallow (0-4 cm) and a deep (0-14 cm) – were located at locations 1, 2 and 3. Inset illustrates how tubing for both a shallow (red) and deep (blue) tubing was installed and anchored using an aluminum rod at each of the three locations. Differential pressures were measured between tube ends in shallow (sensors 1s, 2s and 3s) and deep (sensors 1d, 2d, and 3d) tubes. Note that data from only five sensors is presented because data from the deep sensor at location 3 (3s) was erroneous.

### 3.3.1.3 Differential Pressure Measurements

Six Validyne P24 differential pressure sensors were deployed to measure pressure gradients across the seabed [Validyne, 2014]. In these sensors, a difference in pressure between the two ports induces flexing in a metal diaphragm, which in turn produces a +/-

5 V analog DC output with an error equivalent to 0.250% of full scale. We selected ‘dash 28’ diaphragms with a 56 cm H<sub>2</sub>O range, so that each sensor has an error of 1.4 mm H<sub>2</sub>O. A length of polyethylene tubing (approximately 6 m x 1/16” inner diameter and 1/8” outer diameter) was attached to both the positive and negative orifices of each differential pressure sensor so that pressures were measured between the positive and negative tubing ends. Tubing and sensors were filled with degassed water (hot tap water further degassed by applying negative pressure with a syringe) to minimize compressibility between the orifice and diaphragm. The translucent tubing was examined immediately before deployment to confirm that no bubbles were present. Analog voltage signals from the differential pressure sensors were digitized and logged with a Campbell CR1000 logger at 10 Hz. The differential pressure sensors, logger, and two 12 v batteries were mounted in a waterproof case installed well above the high tide level on an upright pole of the tripod (Figure 3.3). Prior to deployment, each sensor was zeroed and a calibration curve between pressure and voltage was established for each sensor.

The six differential pressure sensors were deployed in 3 pairs of 2 to measure differential pressure between 0 and 4 cm depth and 0 and 14 cm depth at three locations. Hereafter, each differential pressure sensor is described first by the mounting rod to which the tubing was attached (1, 2 or 3) and then by the depth of the lower tube “s” (for shallow) or “d” (for deep), such that the 6 differential pressure sensors are described as *1s*, *1d*, *2s*, *2d*, *3s*, and *3d*. Prior to deployment, tubing ends were firmly attached to three 0.5 m long aluminum mounting rods (Figure 3.3 inset) and tubing orifices were wrapped in fine nylon screen material. The mounting rods were pushed vertically into the seabed, taking care not to damage the tubing, until the upper orifice of each tube was level with the seabed. The three mounting rods were spaced 1 m apart in a triangular pattern. The twelve tubes were routed through a trench to the base of the tripod and up the tripod leg to the waterproof case. A *burst* of data was recorded at 10 Hz for 6 minutes every hour, on the hour, resulting in 2400 differential pressure measurements per sensor per hour – a

total 4,680,000 differential pressure values over the 11-day deployment. Sensor 3s had a clear and large drift during the deployment and data from that sensor was discarded, thus we only present data from the remaining 5 sensors.

Voltage data was converted to differential pressure by applying the calibration. Hydraulic gradients calculated from this differential pressure were used with Darcy's law to calculate *uncorrected instantaneous exchange* (Figure 3.2d). A sixty-second moving average was calculated and subtracted from uncorrected instantaneous exchange to calculate *instantaneous exchange*. By subtracting the moving average, pressure gradients that remain constant over time scales longer than one-minute are removed (possibly induced by tides, persistent currents, terrestrial gradients, or drift in the pressure sensor). The positive and negative values of instantaneous exchange are *instantaneous discharge* and *recharge*, respectively. The magnitudes of burst-averaged instantaneous discharge and recharge are equal, describe the same value ( $q_w$ ) as Equation 3.1, and are thus referred to as *wave-induced benthic exchange*. This value describes the one-way benthic exchange induced by waves into or out of the seabed.

#### **3.3.1.4 ADCP Data**

Two 2 MHz Aquadopp HR Acoustic Doppler Current Profilers (ADCP) were mounted to the tripod crossbars to measure velocity profiles, water depth as it varied with tide, and to calculate wave parameters [Nortek, 2010]. The ADCPs internally logged three orthogonal velocity vectors (east, north, and up) and pressure for each depth interval or *bin* of each profile. All calculations using parameters measured by the ADCPs were based on this 'east, north, up' data. The compass built into each ADCP was calibrated immediately prior to deployment. In order to prevent interference between the sonars, one ADCP recorded a 'burst' of data every 60 minutes on the hour while the other ADCP recorded every 60 minutes on the half hour. Tide-induced benthic exchange values were calculated with tide elevation (from ADCP pressure data) and equation 3.7.

A tidal amplitude was determined for each ebb and flood tide from which tide-induced exchange rates were calculated.

An *up-facing ADCP* was mounted to the instrument frame to measure velocity profiles in the water column, with the ADCP head 0.21 m above the seabed. Twelve bins were spaced at 10 cm with a 20 cm blanking distance. Bursts of data were recorded at 4 Hz for 10 minutes every hour on the half-hour. The values recorded by this ADCP were linearly interpolated from the nearest value ahead of and behind the hour for direct comparison. The *PUV* method was used to estimate wave parameters ( $T_w$  and  $h_w$ ) and wave direction from pressure ( $P$ ) and the two horizontal velocity components ( $\vec{u}$  and  $\vec{v}$ ) [Nortek 2010]. Pressure and the average velocities from cells 2 through 4 (depth range = 51 to 81 cm above seabed) were used for these calculations. The wave period for each burst was also calculated with two additional methods: 1) from a Fourier Transform of differential pressure sensor data for each burst, and 2) from the frequency of peaks in the smoothed ADCP pressure signal. The three methods matched well, and the *PUV*-derived  $T_w$  value was assigned in all except 41 of the 260 bursts, in which the *PUV* script could not assign a  $T_w$  value. In these 41 bursts the average value from the peaks and differential pressure methods was assigned as the  $T_w$  value. Wave-induced benthic exchange was calculated from these data and Equations 3.1 and 3.2 for each burst and compared to benthic exchange calculated from differential pressure sensor data. Wave-induced benthic exchange calculated from ADCP-derived wave parameters is hereafter the *ADCP method*.

A second *down-facing ADCP* was mounted to the tripod to measure currents at the seabed. The head was 75 cm above the seabed and directly above pressure sensor 1s and 1d. The blanking distance was set to 10 cm and bin spacing was set to 2 cm for a total of 33 bins. Data was logged at 1 Hz in 5 minute bursts every hour on the hour. The tide level dropped below the ADCP head during three low tides with corresponding gaps in data. Mean flow velocity ( $U$ ) for each burst was calculated from the middle one-third

of the down-looking ADCP velocity profile in order to remove noisy data at the profile top and bottom linked to low tide and bin-overlap with the seabed. Current-induced benthic exchange was calculated using Equations 3.5 and 3.6 from these data and, because we did not measure bedform dimensions, across a reasonable range of  $L_b$  and  $h_b$  values ( $L_b=0.01$  to  $0.5\text{m}$ ,  $h_b=0.01$  to  $0.1$  m).

### **3.3.2 Wind Data**

Wave-induced benthic exchange was also calculated from wind velocity and direction data collected at the three nearest National Weather Service weather stations during October 2014 [NCDC, 2016]. Georgetown, DE (GED, 929 records), Ocean City, MD (OXB, 976 records), and Salisbury, MD (SBY, 969 records) were 43.5, 23.0, and 31.6 km from the study site, respectively (Figure 3.1a). Wind fetch was measured in Google Earth as the distance between the tripod and the far shore for all compass directions (Figure 3.1b) and assigned based on measured wind direction (10 degree resolution). Wind velocity and direction data was processed with equations 3.2, 3.3, and 3.4 to obtain wave parameters, which were used in equation 3.1 to obtain wave-induced benthic exchange values. These were compared to wave-induced benthic exchange calculated from differential pressure sensors and ADCP data. Wave-induced benthic exchange calculated from wind-derived wave parameters is hereafter the *wind method*. Wind records are recorded at irregular intervals (47 minute average), so for comparison to other measurements collected on the hour, wind-based wave-induced benthic exchange rates were linearly interpolated from the nearest value ahead and behind the hour.

### **Numerical groundwater flow modeling**

Transient groundwater flow models were constructed using MODFLOW-2005 [Harbaugh et al., 2000] to investigate the effects of wave parameters, water depth, and aquifer parameters ( $S_s$  and  $K$ ) on groundwater velocities, benthic exchange zone depth, and residence times in seabed aquifers under the influence of waves. A sensitivity

analysis showed that wave-induced flux depends on hydraulic diffusivity ( $D=K/S_s$ ) rather than  $K$  or  $S_s$  alone, so the field-measured  $K$  value was held constant in all model runs while  $S_s$  was varied.

A total of 2080 MODFLOW simulations were constructed and run to represent wave conditions of each of the 260 measured bursts and for each of eight values of  $S_s$ . Each set of 260 models was assigned a single  $S_s$  value from  $10^{-2}$  to  $10^{-5.5}$  m<sup>-1</sup> at half-magnitude intervals (Figure B.1). Three model sets ( $S_s = 10^{-2}$ ,  $10^{-3}$ , and  $10^{-4}$  m/s) are presented in greater detail herein than the other five sets.

Each 2-D cross-sectional MODFLOW model (100 layers by 120 columns) was assigned a thickness of  $L_w$ , which is twice the depth of  $L_w/2$  expected for wave-induced benthic exchange [e.g. King 2009] (Figure 3.4). Model columns were assigned a width of  $L_w/40$  and each stress period (1 timestep per stress period) was assigned a duration of  $T_w/20$  (i.e. waves are each 40 cells wide and 20 stress periods long). Each model was run for  $T_w*50$  seconds, or 1000 stress periods. Results were calculated based on one wavelength in the middle of the domain (columns 41-80) to avoid potential edge effects along the model boundaries, and the last wave period (stress periods 981-1000) to ensure that dynamic steady state had been achieved.

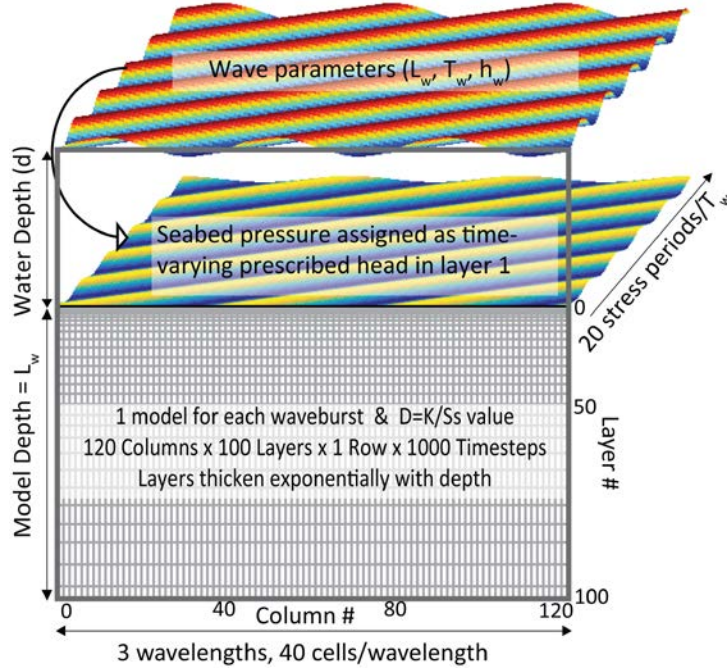


Figure 3.4: Modflow model schematic of geometry and boundaries.

For each stress period, a wave-induced hydraulic head was prescribed to all cells across the top model layer using the MODFLOW “Time-Variant Specified-Head” package [Harbaugh et al., 2000]. The space- and time-varying seabed pressure value was calculated with linear wave theory [e.g. King et al., 2009], which depends on  $T_w$ ,  $h_w$  and  $d$ . In each stress period, the wave pressure signal on the seabed migrated a distance  $1/20 L_w$  (1 column). The pressure signal therefore repeated after one wave period. All other model boundaries were prescribed as zero flow.

For each model, a representative residence time ( $R_k$ ) was calculated for each layer ( $k$ ) as:

$$R_k = \sum_{n=1}^k \frac{V_k}{|Q_{\bar{w}}|} \quad (3.8)$$

where  $V_k$  is the volume of a cell in layer  $k$ , and  $|Q_{\bar{w}}|$  is the mean magnitude of the vertical component of wave-induced groundwater flow measured across the top boundary of cells in that layer. The  $R_k$  value may be considered a description, on average, of the

age of water at a certain depth. This calculation makes several assumptions and it is not intended to be an exact value of residence time. However,  $R_k$  is a useful indicator to identify how wave and aquifer parameters affect the residence time of water in the benthic exchange zone.

## **3.4 Results**

### **3.4.1 Wave-Induced Benthic Exchange**

#### **3.4.1.1 Field-Based Analysis**

Wave-induced benthic exchange rates calculated from the 5 differential pressure measurements averaged 20.0 cm/d and ranged from 1.75 to 92.3 cm/d over the 260 bursts (Figure 3.5a, g, B.2, Table 3.1). The average wave-induced benthic exchange from shallow sensor measurements was 29.1 cm/d, or 217% of the average wave-induced benthic exchange from deep sensor measurements. Thus, only about one-half of the wave-induced pressure amplitude was measured at 14 cm depth (deep sensors) compared to 4 cm depth (shallow sensors), indicating that wave-induced pressure gradients are attenuated rapidly with depth in the aquifer. Wave-induced instantaneous exchange had a maximum rate of 1613 cm/d (0.19 mm/s; 5-sensor average) during the course of the study. In a given burst, the maximum instantaneous exchange measured with a differential pressure sensor wave-induced benthic exchange rate ( $q_w$ ) by an average of about 1 order of magnitude (8.2 to 10.1 times for the 5 sensors).

Table 3.1: Burst-Averaged Wave-, Current-, and Tide-Induced Benthic Exchange Rates

		Wave-induced ( $q_w$ ) (cm/d)							Current-induced <sup>a</sup>	Tide-induced	
		Differential Pressure Sensors			ADCP	Wind	Groundwater Models			( $q_b$ )	( $q_t$ )
		Shallow Sensors	Deep Sensors	5-sensor Mean			$S_s=10^{-2}$	$S_s=10^{-3}$	$S_s=10^{-4}$	(cm/d)	(cm/d)
Mean	1s:	25.78	9.49								
	2s:	32.47	17.38	19.96	22.47	11.71	105.80	34.74	16.58	0.07	3.43
	3d:		14.64								
Median	1s:	13.46	4.46								
	2s:	19.29	9.84	11.08	13.40	06.78	45.06	14.98	08.19	0.04	3.43
	3d:		8.08								
Min	1s:	1.76	0.77								
	2s:	2.92	0.98	1.75	01.47	0.00	01.57	0.69	0.62	0.00	2.34
	3d:		0.79								
Max	1s:	113.95	49.97								
	2s:	148.32	81.16	92.30	103.76	87.85	596.75	194.03	82.28	0.47	4.62
	3d:		69.71								
$\sigma$	1s:	26.45	10.66								
	2s:	31.38	17.57	20.05	21.42	13.11	129.59	42.10	18.01	0.08	0.50
	3d:		15.09								
CV <sup>b</sup>	1s:	1.03	1.12								
	2s:	0.97	1.01	1.00	0.95	1.12	1.22	1.21	1.09	1.20	0.15
	3d:		1.03								

Note: All values in table are mean value over the 260 bursts

<sup>a</sup>The current-induced values assume the tallest, steepest bedform.

<sup>b</sup>Coefficient of variation (CV) =  $\sigma$ /mean

Figure 3.5: Hourly ADCP-and-wind-generated wave parameters and wave-induced benthic exchange values. a.) Individual and mean wave-induced benthic exchange rates calculated from data collected with 5 pressure sensors. Shaded green region below 10 cm/d represents the measurement error (see discussion in section 5.3). b.) ADCP-derived significant wave height ( $h_w$ ) and peak period ( $T_w$ ) from peaks and PUV methods. Wind c.) fetch and d.) velocity for data from three weather stations. e.) Significant wave height and f.) wave period from ADCP and wind data. g.) Wave-induced exchange rates calculated from pressure sensors (5-sensor average in black, the 2-sensor shallow average and 3-sensor deep average bracket the gray region), and ADCP-derived and wind-derived wave parameters.

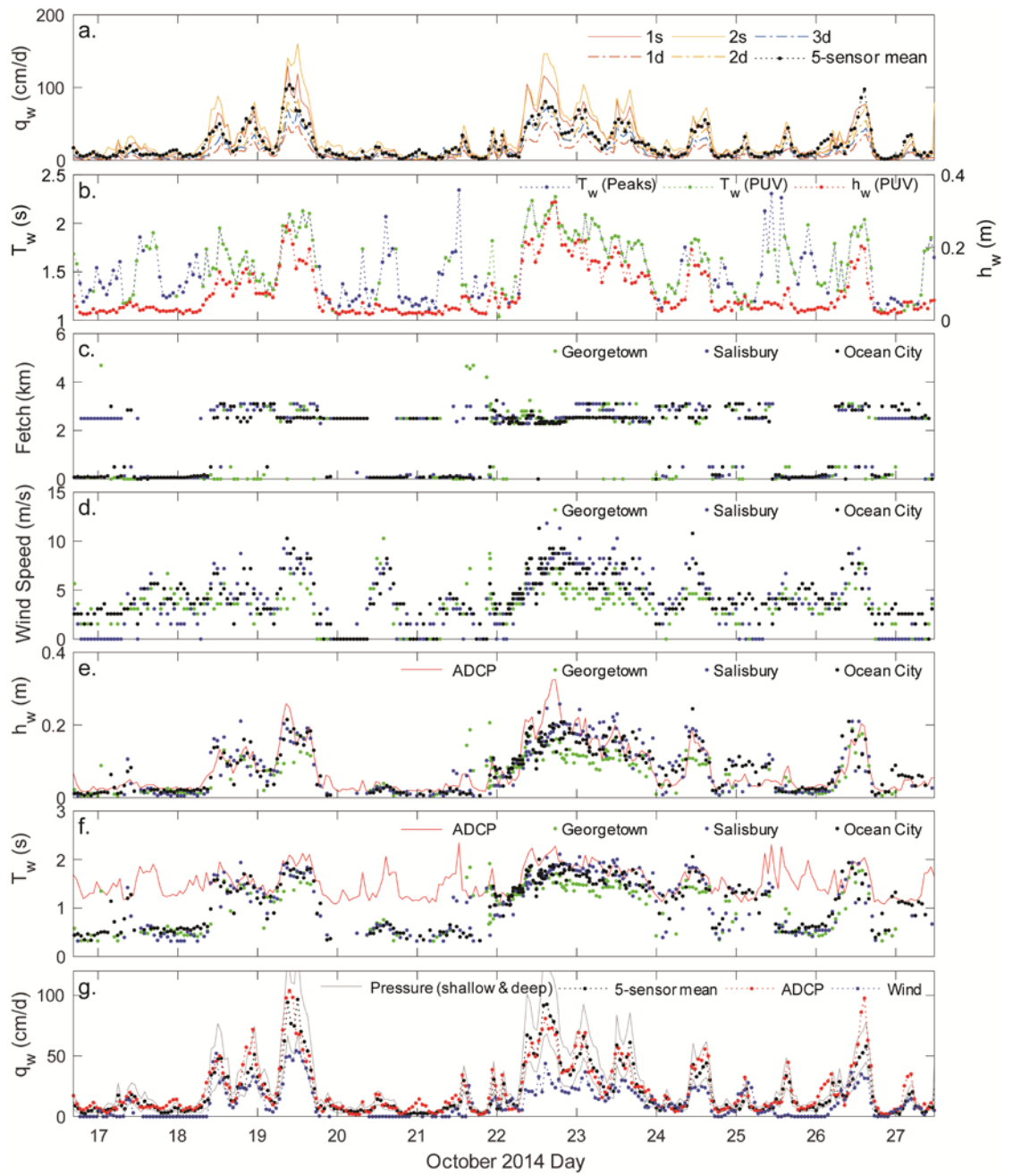


Table 3.2: Wave Parameters Calculated with Different Methods

	Calculation Method	Mean	$\sigma$	Min.	Max.
Wave Period ( $T_w$ )	PUV	1.62	0.29	1.04	2.28
	Peaks	1.60	0.33	1.08	2.34
	Differential pressure sensors	1.66	0.32	1.08	2.93
	Applied $T_w$ value <sup>a</sup>	1.62	0.30	1.04	2.34
	Wind: Georgetown	0.69	0.57	0.00	1.97
	Wind: Ocean City	0.74	0.57	0.00	2.11
	Wind: Salisbury	0.85	0.56	0.00	2.06
	Wind: Average	0.54	0.57	0.00	2.11
Wave Height	PUV	7.51	6.69	1.61	32.5
	Wind: Georgetown	4.37	4.95	0.00	21.1
	Wind: Ocean City	4.75	5.49	0.00	25.8
	Wind: Salisbury	5.60	5.37	0.00	24.5
	Wind: Average	4.91	5.27	0.00	25.8

<sup>a</sup>value used to calculate wave-induced benthic exchange from the ADCP method

Wave-induced benthic exchange calculated analytically (Equation 3.1) from ADCP-based wave parameters averaged 22.5 cm/d (Figure 3.5b, g, Table 3.1). Values of  $h_w$  calculated with the PUV method averaged 7.5 cm and  $T_w$  values averaged 1.62 s. Burst-averaged velocity magnitudes from the up-looking ADCP averaged 7.7 +/- 3.0 cm/s and ranged from 1.6 to 14.0 cm/s.

Wave-induced benthic exchange calculated from wave conditions derived from wind data averaged 11.7 cm/d (Figure 3.5g, Table 3.1). During the experiment, winds were predominantly Northerly and Southerly. The resulting fetch was bimodally distributed (Figure 3.5c) because southern shorelines are close (148 m average), whereas northern shorelines are far (3.3 km average; Figure 3.1b). Wind velocities averaged 3.70 +/- 2.40 m/s with sustained winds measured up to 13.4 m/s (Figure 3.5d). Wave parameters ( $h_w$  and  $T_w$ ) calculated with the wind data from the 3 NOAA wind stations were similar (Figure 3.5e, f, Table 3.2). Wind-derived  $h_w$  and  $T_w$  values matched well

with those calculated from ADCP data when fetch was long, but not as well when fetch was short (Figure 3.5c, e, f). Wave-induced benthic exchange calculated with the wind method followed a similar trend as those calculated with the differential pressure and ADCP methods, but averaged about half (59% and 52%, respectively). This was largely due to the short fetches from southerly winds produced calculated wave conditions that were less energetic than those measured locally (Figure 3.5c, d, g).

#### **3.4.1.2 Groundwater Flow Model Results**

Numerically simulated wave-induced benthic exchange from the set of high-D models matched well with the wave-induced benthic exchange calculated from the differential pressure measurements and ADCP methods (Figure 3.6a). This agreement is expected because a low compressibility assumption (reasonable for the sandy sediments) and identical wave conditions were prescribed for both the numerical and analytical solutions. Modeled wave-induced benthic exchange from the low-D models averaged 5.3 times greater than the wave-induced benthic exchange calculated with the ADCP method (average = 105.8 cm/d; Figure 3.6a and Table 3.1), because the numerical model accounted for the highly compressible aquifer. Numerically simulated wave-induced benthic exchange followed the same trends as wave-induced benthic exchange calculated with the other three methods for all tested values of D.

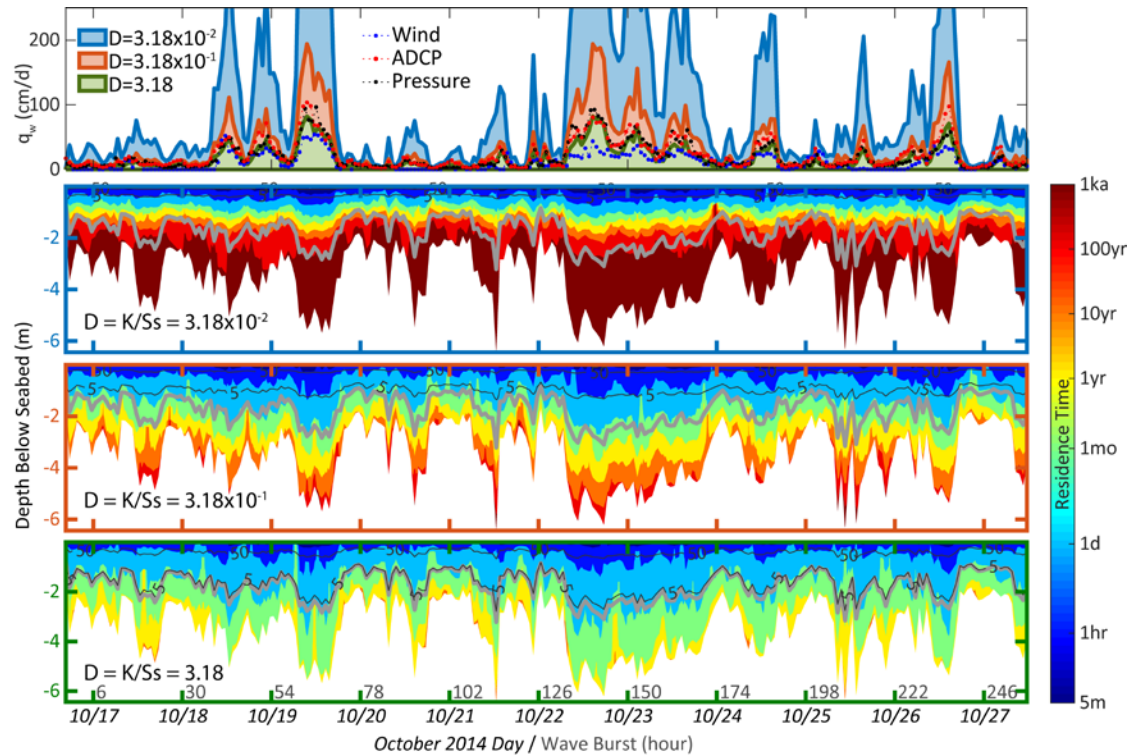


Figure 3.6: Effect of wave parameters and hydraulic diffusivity on  $q_w$ , residence time, and depth of wave-induced flux. a.) Comparison of wave-induced benthic exchange rates from numerical models and calculated from field data. Panels b., c., and d. show average residence time (colorplots) and mean depth of flux (black contours) for each of 260 Modflow model runs. Model thickness was prescribed as  $L_w$ , which varied between wave bursts, so the model thickness and depth of plotted data vary temporally. Hydraulic diffusivity was assigned as  $3.18 \times 10^{-2}$ ,  $10^{-1}$ , and  $10^0$  to represent clay, sand and gravel for models presented in panels b., c. and d., respectively. The labeled black contours show depths at which vertical flux magnitudes are 50% and 5% of benthic exchange across the bed—the 5% contour ( $d_{ex}$ ) approaches a depth of  $L_w/2$  (grey contour) at high hydraulic diffusivity (panel d).

Simulated exchange zone thicknesses were proportional to both  $L_w$  and  $D$ . For simplicity, the exchange zone is defined as the zone in which vertical wave-induced groundwater flow in the seabed aquifer exceeds 5% of the wave-induced benthic exchange across the seabed, the thickness of which is denoted  $d_{ex}$ .

In the set of high- $D$  models representative of the relatively incompressible and permeable aquifer at the study site ( $D=3.18 \times 10^0$  m/s),  $d_{ex}$  averaged 1.69 m (Figure 3.6d). This  $d_{ex}$  value is 97% of  $L_w/2$ , which is the depth that surface waves are predicted to influence according to analytical solutions that neglect sediment compressibility [e.g. King et al., 2009]. The benthic exchange zone thickness decreases markedly as  $D$  decreases:  $d_{ex}$  averages 1.01m (58% of  $L_w/2$ ) and 0.37m (21% of  $L_w/2$ ) for intermediate- $D$  ( $3.18 \times 10^{-1}$  m/s; Figure 3.6c), and low- $D$  ( $3.18 \times 10^{-2}$  m/s; Figure 3.6d) models, respectively. Because  $L_w$  varied during the course of the study, the exchange zone was also highly variable for all model sets. No correlation appears to exist between  $d_{ex}$  and either  $h_w$  or  $d$ .

Average residence times increased with depth for all model cases—the increase with depth was most rapid in the low- $D$  model where the exchange zone was thinnest, whereas the rate of increase of residence time was lowest in the high- $D$  model where the exchange zone was thickest (Figure 3.6b-d). The thin, low- $D$  exchange zone, combined with high exchange rates, results in a short mean residence time of just 5.5 days (Figure 3.6b). Residence times were longer in the higher- $D$  model sets, with larger  $d_{ex}$  values—the residence time in the intermediate- $D$ , and high- $D$  aquifers average 70.9 and 183.3 days, respectively (Figure 3.6c, d). Residence time has a strong correlation with  $L_w$  ( $r^2=0.98, 0.99$ , and  $0.97$  in low- $D$ , intermediate- $D$ , and high- $D$  model sets, respectively), but a correlation to  $h_w$  and  $d$  was not observed.

### 3.4.2 Current- and Tide-Induced Benthic Exchange

Estimates of current-induced benthic exchange, calculated from down-looking ADCP-measured currents (Figure 3.7a, b), water depth (Figure 3.7b), and assumed bedform dimensions were consistently much less than wave- and tide-induced benthic exchange during the measurement period (Figure 3.7c, Table 3.1). Near-bed currents measured with the down-looking ADCP averaged  $3.0 \pm 1.3$  cm/s (red line in 7b), and water depth averaged  $1.28 \pm 0.27$  m (black line in Figure 3.7b). Current-induced benthic exchange rates were calculated for a range of bedform dimensions ( $h_b = 1$  to 10 cm and  $L_b = 5$  to 50 cm) for each burst (shaded cyan region in Figure 3.7c). The steepest bedforms resulted in the highest current-induced benthic exchange rates, which averaged  $6.5 \times 10^{-2}$  cm/d over the study period (thick upper blue line in Figure 3.7b). This exchange rate is just 0.33% of the average wave-induced exchange rate calculated from differential pressure measurements.

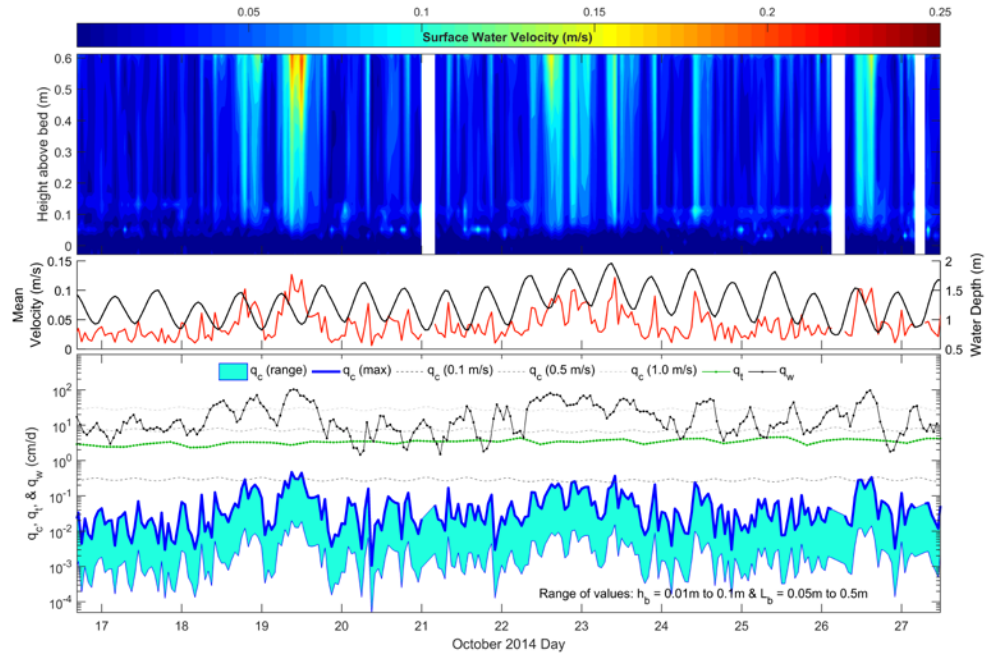


Figure 3.7: Current- and tide-induced benthic exchange values and the data used to calculate them. a.) Color plot of burst-averaged water column velocity profiles from down-looking ADCP. b.) average velocity in middle third of profile (red line), and water depth (black line). c.) Wave-induced  $q_w$  (from differential pressure measurements), current-induced  $q_c$  (from measured currents and range of bedform dimensions), and tide-induced  $q_t$  (from pressure measurements).

Tide-induced benthic exchange calculated analytically (3.70 cm/d average) was always greater than current-induced benthic exchange, but exceeded wave-induced benthic exchange in only 9 of 260 bursts (3.6%; Figure 3.7c, Table 3.1). The mean measured tidal amplitude was  $0.33 \pm 0.05$  m (range = 0.23 to 0.44 m) and the mean tidal period during the deployment was 12.4 hours (Figure 3.7b). This is consistent with the finding of Sawyer et al. [2013] for simulations over the entire Delaware Inland Bays.

### **3.5 Discussion**

#### **3.5.1 Comparison of Wave-Induced Benthic Exchange Methods**

The wave-induced benthic exchange rates obtained from differential pressure measurements and ADCP-based calculations had similar magnitudes and were well correlated ( $R^2=0.868$ ; Figure 3.5; Figure 3.8a), which supports the validity of both methods. This goodness of fit between ADCP- and differential pressure-based exchange rates was not correlated to  $T_w$ ,  $h_w$ , wind direction or speed, tidal stage, or mean current velocity. The agreement between the ADCP-based method and the high-D set of groundwater flow models also supports the use of the analytical model of Equation 3.1 to calculate exchange from wave parameters for relatively incompressible seabed sediments. A lack of agreement between these methods and the low-D numerical model suggests that sediment compressibility is an important control on wave-induced exchange in seabed aquifers composed of finer and more compressible sediments, and that the analytical model should not be used where that is the case.

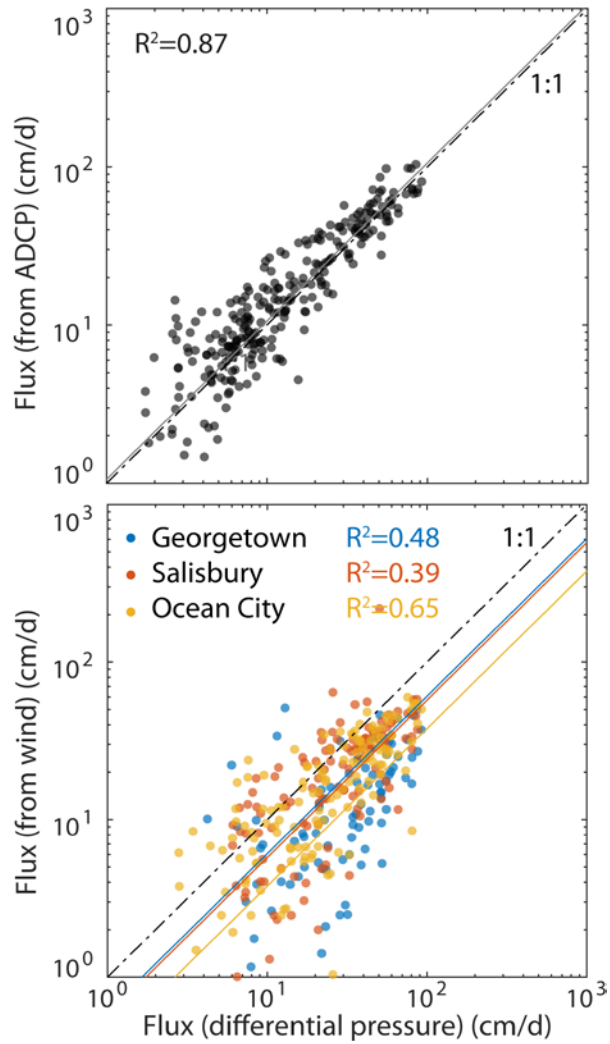


Figure 3.8: Comparison of benthic exchange calculation methods. a.) Differential pressure vs. ADCP-measured wave parameters. b.) Differential pressure vs. wind-derived wave parameters. Although plots are in log-log space for clarity,  $R^2$  values in both plots are for linear, not log, comparisons.

ADCP-derived exchange rates frequently exceeded differential pressure-derived exchange rates and averaged 12.6% larger than the average from all 5 sensors (Figure 3.5g; Tables 3.1, 3.2). This is likely because we are underrepresenting the real flux by including the deep pressure sensor data in these calculations. A more accurate method might be to average only shallow-sensor-based exchange rates because they capture near-seabed pressure gradients that have not attenuated with depth as much as the signal recorded by the deep pressure sensors—fluxes from the shallow sensors exceeded ADCP-derived rates by 30% (Figure 3.5a, g, Table 3.1). We might expect this difference because aquifer compressibility is ignored by the ADCP method but inherent in the pressure-based method, and compression increases wave-induced benthic exchange rates across the seabed.

Wind-derived wave-induced benthic exchange rates were lower than those calculated from the ADCP (52.1%) and pressure (58.7%) data, particularly when fetch was limited (Figure 3.5g, Table 3.2). At those times, the empirical wind-generated wave model underestimated wave intensity because effects of wave spreading, hysteresis, and non-wind wave sources were unaccounted for [e.g. Young and Verhagen, 1996; Herbers et al., 1999]. Prescribing a minimum  $T_w$  value, a technique employed in other wave models [e.g. Tolman, 2009] and consistent with measured wave data (Figure 3.5b), could improve matching. Wind data and resulting wave-induced benthic exchange rates were inconsistent among the three weather stations (Figure 3.5, 8b), which illustrates the difficulty of characterizing wind over the distances between the study site and weather stations (23-43 km; Figure 3.1a). This method has great potential because of its ease, but improved results would require either more accurate wind data and application only at locations with greater fetch, or more complex wave models.

### 3.5.2 Exchange Zone Thickness

An empirical formula to relate  $D$ ,  $L_w$ , and  $d_{ex}$  was developed by comparing  $d_{ex}$  and  $L_w$  in the 8 model sets. In each of these 8 model sets, a line with a zero Y-intercept was fit to  $d_{ex}$  vs.  $L_w$  (Figure B.3). An empirical relationship was established by plotting these 8 slopes vs. the  $D$  for each model set:

$$\frac{d_{ex}}{L_w} = \begin{cases} 0.188 \log_{10} D + .369, & D < 4 \\ 0.481, & D \geq 4 \end{cases} \quad (3.9)$$

Thus, the exchange zone depth in high- $D$  aquifers approaches the commonly cited theoretical exchange zone thickness of  $\frac{1}{2} L_w$  (e.g. King et al., 2009). However, that rough estimate greatly overestimates  $d_{ex}$  in low- $D$ , aquifers. Seabed sediment type varies widely, but an estimate of exchange depth for reasonable sand  $K$  and  $S_s$  values gives perspective. Assuming  $K$  values for clean sand range from  $10^{-6}$  to  $10^{-3}$  m/s (e.g. Fetter, 2001) and  $S_s$  for sand is  $\sim 10^{-3} \text{ m}^{-1}$  (Figure B.1), the corresponding exchange depths range from nearly zero to the theoretical maximum ( $\frac{1}{2} L_w$ ).

Exchange depths for current-induced flow are on the order of one bedform wavelength [Cardenas and Wilson, 2006; Elliott and Brooks, 1997; Thibodeaux and Boyle, 1987], which are assumed in this study to be less than 0.5 m (and probably much less). Tide-induced exchange depths in this estuary have been calculated to be on the order of millimeters to centimeters, and depend on tidal period, tidal amplitude,  $c$ ,  $K$ , and effective porosity, which influence penetration and tide-induced benthic exchange [Sawyer et al., 2013]. Thus, the exchange zone generated by wave-induced exchange is consistently larger (and generally much larger) than that generated by tides or currents at the Holts Landing study site.

Exchange zone thickness is likely variable on small spatial scales due to sediment heterogeneity. This can be seen by comparing the pressure data at the two sensor locations that had measurements at two depths. Pressure attenuated more rapidly with depth at Sensor 1 than at the Sensor 2 location, despite being just 1 m apart. The time-

averaged absolute pressure difference at 1d was 129% of that measured at 1s, whereas the value at 2d was 185% of the 2s value. The MODFLOW model results show that this difference can be accounted for by variability in  $K$  or  $S_s$ .

### 3.5.3 Sources of Uncertainty

There are a number of uncertainties in the calculations used to estimate benthic exchange in this study. First, it is unclear how nonlinear interactions between these three mechanisms affect the resulting rates of benthic exchange [e.g. King et al., 2012; Sawyer et al., 2013]. For instance, net discharge or recharge from tides or terrestrially-derived fresh discharge could impede or enhance shallow exchange mechanisms like wave- or current-induced exchange [e.g. Cardenas and Wilson, 2007]. The effects of these interactions is difficult to quantify and are in need of further investigation.

Changes in seabed elevation also affect benthic exchange calculations that include water depth as a parameter. These changes can occur quickly, depending on the hydrologic and sedimentological conditions. During the deployment, reductions in seabed elevation of up to 0.5 cm were observed. This was assumed to be the result of scour lowering the seabed rather than movement of the well-anchored orifice. This seabed movement could affect the water depth used in the calculations (e.g. Equations 3.1-5). It also suggests that the sensor tube and mounting rod could impose an observer effect that affected exchange. Lastly, changes in orifice depth could cause variability in the assumed constant  $dl$  term of Darcy's law and affect differential-pressure derived fluxes. The  $<0.5$  cm bed movement could have an impact of up to 12% on the resulting wave-induced fluxes, which might explain some of the discrepancy between ADCP and differential-pressure-based exchange rates.

Error inherent to measurements made with pressure sensors also reduces the certainty of pressure-based calculations of wave-induced flux. For the  $K$  value measured in this study, the 1.4 mm error associated with each pressure sensor translates to an

instantaneous exchange error of 96 cm/d for shallow sensors and 27 cm/d for deep sensors. Although some wave-induced exchange rates are within the measurement error, those rates were determined from instantaneous exchange values that well-exceed that error, so we have confidence in our calculated exchange rates. Furthermore, by subtracting the moving average during processing we removed any bias component of the error. Finally, wave-induced benthic exchange rates obtained from differential pressure measurements and ADCP-derived values correlated well even at low values (Figure 3.8a).

#### **3.5.4 Comparisons to Larger-Scale Drivers of Exchange**

The measured wave-induced benthic exchange values are similar in magnitude to flux measurements on longer temporal scales at this site. Russoniello et al. [2013] and Sawyer et al. [2014] used seepage meters to characterize submarine groundwater discharge (SGD) near the location of the tripod used in this study. SGD in the area near the tripod was composed of recirculated baywater and had net discharge values ranging from 0 to 50 cm/d, which is similar in magnitude to wave-induced benthic exchange rates measured in this study. These seepage meter measurements integrated SGD at 2 hour intervals, so they are characterizing a different driving mechanisms than the short-timescale associated with wave-induced exchange. Nearer to shore, these studies identified fresh SGD rates as high as 32 cm/d, so wave induced exchange rates exceed the highest measured terrestrially-driven SGD.

#### **3.5.5 Implications for Biogeochemical Reactions**

Biotic and abiotic reaction rates in the benthic exchange zone depend on the supply of reactive solutes and the residence time of those solutes in the benthic reaction zone. Our analysis shows that surface waves have a strong control on solute fluxes, the size of the reactive zone, and the residence time in that zone, and those controls are

greater than those imposed by tides and currents at our field site, a typical shallow estuary. Thus waves strongly influence benthic reactivity and corresponding chemical fluxes through and discharging from the seabed [e.g. Shum, 1993; Cardenas et al., 2008] and influencing elemental cycling [e.g.]. The new understanding of spatial and temporal variability of wave-induced exchange derived from this analysis can help identify the “hot spots” and “hot moments” in submerged sediments and coastal aquifers [Marzadri et al., 2012; Zarnetske et al., 2011; Briggs et al., 2014; Heiss et al., 2017]. In the benthic exchange zones, reactions in hot spots and during hot moments are highest when the residence timescale matches the reaction timescale [Harvey et al., 2013; Gomez-Velez et al., 2015]. “Hot moments” of high reactivity should occur when long  $L_w$  values drive deep exchange and large  $h_w$  values generate rapid benthic exchange rates with short residence times (Equations 3.1, 3.9). “Hot spots” should occur where high-diffusivity sediments (large  $K$ , small  $S_s$ ) result in relatively deep mixing zone and relatively short residence times.

### **3.6 Conclusions**

Benthic exchange in a shallow, sandy, micro-tidal estuary were quantified using 6 independent techniques involving field measurements, numerical simulations, and analytical models to 1) compare estimation methods, 2) characterize primary controls on the spatial and temporal variability in exchange rates, depths, and residence times, and 3) compare the relative influence of waves, tides, and currents. The agreement between wave-induced benthic exchange calculated from high-resolution differential pressure measurements across the seabed and an analytical solution based on ADCP-measured wave parameters showed that such exchange can be accurately measured with pressure sensors in field settings. Numerical groundwater model results showed that the simple analytical solution applied represents exchange well for incompressible seabed sediments but overestimates the exchange in compressible sediments. The models also showed that

the depth of benthic exchange in typical seabed sediments ranged from nearly zero in more compressible sediments to a maximum depth of one-half the surface wavelength in rigid aquifers. The results can be used to predict factors that affect the biogeochemistry of benthic exchange zones and their effects on shallow estuaries where wave-induced benthic exchange is a dominant mechanism. The insights gained may aid coastal managers in quantifying nutrient and contaminant loads to and processing within estuarine and nearshore ecosystems.

### **3.7 Acknowledgements**

The authors thank Jack Puleo, James Kirby and Arthur Trembanis for lending field equipment, Mahfuz Khan, Carter Duval and Margaret MacGibeny for assistance deploying and retrieving equipment, Caitlyn Sarno for assistance with sediment analysis, Audrey Sawyer for constructive comments on experimental design, Leonard Konikow for modeling assistance, and Adam Skarke and Ryan Mieras for assistance processing field data. The paper benefitted from the feedback of Jud Harvey and an anonymous reviewer. This work was funded by the US National Science Foundation EAR-0910756 and EAR-1246554 and the University of Delaware Office of Graduate and Professional Education Summer Doctoral Fellowship. Data may be accessed on the CUAHSI HydroShare database [Russoniello et al., 2017].

## Chapter 4

### **PATTERNS OF WAVE-DRIVEN BENTHIC FLUXES ACROSS THE GLOBAL SEABED**

#### **ABSTRACT**

Waves traveling over continental shelves drive fluid fluxes through the seabed that are a dynamic and significant portion of the global water budget. These fluxes contribute solutes that drive reactions in the benthic zone, which impact global chemical cycles at rates dependent on the magnitude of fluid exchange. Thus, accurate estimates of benthic exchange rates and patterns are critical to determine the impact of waves on ocean chemistry and to identify locations and times of intensive biogeochemical cycling. We draw on hindcast models of global ocean waves to calculate wave-driven benthic exchange (wave pumping) at high spatial and temporal resolution for 31 years from 1979 through 2009. Wave pumping averages  $1.8 \times 10^5 \text{ km}^3/\text{yr}$  over this period—equivalent to 6.1 m/yr over the entire global shelf area—enough to flush the global ocean every 7600 years. Wave pumping is seasonal in the major ocean basins, especially the circumpolar oceans where winter sea ice cover inhibits wave propagation. Regional analysis shows that 21% of wave pumping is driven by extreme events in the top 10 percentile, and that tropical cyclones are responsible for most very large wave-pumping events. Global climate models predict increases in the frequency and intensity of these extreme events, which we show can partially offset a predicted general decrease in waves and wave pumping. Similarly, we show that wave pumping will increase by 2-3 times in the Arctic as sea ice decreases. These results show where, when, and at what rates wave pumping occurs, which can help identify the moments and spots where biogeochemical reactions have disproportionate global impacts.

## 4.1 Introduction

Ocean waves traveling over continental shelves pump water and solutes between the water column and seabed aquifer at rates that globally exceed surface and submarine fresh discharge [e.g. Burnett et al., 2003; Huettel et al., 2014; Cho and Kim, 2016; Cho et al., 2018]. Waves are one driver of *benthic exchange*, advective mixing between the water column and the shallow seabed aquifer [Boano et al., 2014]. Benthic exchange drives high rates of biogeochemical activity in shallow continental shelf sediments [e.g. Berg et al., 2003; Glud, 2008; Jahnke et al., 2008], and this mixing of fluids and solutes has important implications for chemical pathways at the global scale. Because waves are among the largest drivers of such exchange [Santos et al., 2012; Sawyer et al., 2013; Russoniello et al., 2018], these *wave pumping* rates and how they vary in space and time can impact global chemical cycles. However, the temporal and spatial distribution of wave pumping has not been investigated on large scales.

Continental shelf sediments are important sinks for carbon, nutrients and metals [e.g. Huettel et al., 2014; Bourke et al., 2016; Laruelle et al., 2018; Chen et al., 2003]. The shelf is host to approximately 20% of global primary pelagic production [Duarte et al., 2005], with much of that occurring in sediments [Jahnke et al., 2000]. These shelf sediments also play an important role in global nutrient cycling, accounting for up to 44% of denitrification [Seitzinger et al., 2006] and half of phosphorous burial [Filippelli 1997; Filippelli 2002]. Ultimately, biogeochemical transformations are controlled by the supply of reactants from groundwater, sediments, and surface water to the benthic zone, as well as the reaction timescale and residence time of water and solutes [Zarnetske et al., 2011; Harvey et al., 2013; Gomez-Velez et al., 2015]. Because infiltrating surface water delivers the bulk of new reactants to shallow shelf aquifers, an accurate quantification of rates and spatiotemporal wave pumping patterns is required to characterize chemical pathways and fluxes in coastal seas.

Wave pumping rates and variability can be calculated at the temporal and spatial resolution of available wave and seabed data, but these data have previously lacked the resolution and coverage to allow global analysis at reasonable scales. Analytical equations for wave pumping [e.g. Riedl et al., 1972; King et al., 2009] have been validated in wave tank [e.g. King et al., 2009; Russoniello and Michael, 2015], and field [Russoniello., et al. 2018] studies. Such solutions have been utilized to calculate and describe spatio-temporal variability of wave pumping for bays [Sawyer et al., 2013] and small continental shelf areas [King., 2011; Riedl et al., 1972]. Studies have extrapolated field and regional estimates of benthic exchange rates to estimate global fluxes [e.g. Riedl et al., 1972; Santos et al., 2012]. However, such extrapolations ignore spatial and temporal variability caused by changes in seabed or wave characteristics, and this variability propagates through to uncertainty in reaction rates and chemical fluxes. Direct analysis of spatially and temporally resolved data on wave and seabed characteristics is required to accurately quantify the impact of wave pumping on global chemical cycles and to identify biogeochemical hotspots and hot moments across the globe.

In this study we estimate the temporal and spatial distribution of wave pumping rates over the global ocean using results from a high resolution ( $< 0.5$  degrees, 3 hour interval) simulation of global waves for the 31-year period between 1979 through 2009 to identify when and where high wave pumping rates are highest and have the greatest potential to impact the chemical composition of ocean waters. We place these results in the context of current and potential future climates to understand how chemical cycles may change as waves and wave pumping change in coming years.

## 4.2 Methods

*Wave pumping velocities* ( $q_w$  [L/T]) were calculated analytically [King et al., 2009] based on depth ( $d$ ), seabed hydraulic conductivity ( $K$ ), wave height ( $h_w$ ), and wave length ( $L_w$ ):

$$q_w = \frac{Kh_w}{L_w \cosh \frac{2\pi d}{L_w}} \quad (4.1)$$

This ‘wave pumping’ value describes only exchange induced by hydrostatic pressure oscillations and does not include other wave-induced sources of benthic exchange such as flux induced by oscillatory currents over bedforms or wave setup [e.g. Santos et al., 2012].

Wave length was calculated from  $d$  and wave period ( $T_w$ ) using the dispersion equation:

$$\left(\frac{2\pi}{T_w}\right)^2 \approx g \frac{2\pi}{L_w} \tanh\left(\frac{2\pi}{L_w} d\right) \quad (4.2)$$

Where  $g$  is gravitational acceleration. *Volumetric wave pumping rates* ( $Q_w$  [ $L^3/T$ ]) were calculated for model cells as the product of  $q_w$  and cell area.

Global wave parameters, significant height of combined wind waves and swell and primary wave mean period ( $h_w$  and  $T_w$ ), were obtained from a hindcast simulation generated by the NOAA Marine Modeling and Analysis Branch [MMAB, 2017] using the Wavewatch III numerical model. Simulation results are available at 3-hour temporal and 4- to 30-minute spatial resolutions (Table C.1) for the period between January 1979 and December 2009. Ocean cells without wave data were considered ice-covered and ice extent was tracked.

Wave pumping was calculated for global and regional scenarios. Two global-scale scenarios were constructed: a *single-K scenario* was built to investigate temporal and spatial variability of the forces driving wave pumping, and a *variable-K scenario* was built to examine how seabed heterogeneity affects spatial variability. Additionally, a regional single-K scenario was run to compare wave pumping rates between extreme events and calm periods. For this purpose, we chose the 106,800 km<sup>3</sup> South Atlantic Bight of the North American East Coast (Figure 4.1c), because 1) we could compare to a previous study of the region [Riedl et al., 1972], 2) a high-resolution wave dataset (4 arcminute) is available for the entire SAB coastline [MMAB, 2017], and 3) the small area

allowed postprocessing of results following the scenario termination (summary statistics were calculated and results were cleared from memory after each timestep in global scenarios). Global scenarios downsampled the waves dataset to a 7-day timestep to balance memory and processing requirements with temporal resolution—the regional scenario retained the 3-hour native timestep.

Water depth and hydraulic conductivity were assumed constant in time, so a single static data layer was applied for each scenario. Global ocean depths were resampled from a one-minute bathymetric model [Amante and Eakins, 2009]. A constant  $K$  of  $1.05 \times 10^{-4}$  m/d was assigned to the global single- $K$  scenario and to the regional SAB scenario. This  $K$  value is representative of sandy continental shelf sediments [e.g. Fetter, 2001] and matches the average global seabed conductivity used by Reidl et al. [1972]. For the variable- $K$  scenario,  $K$  values corresponding to the sediment type were assigned to each cell of a global sediment map (Figure C.1) [ESME, 2012]. A sandy  $K$  of  $10^{-4}$  m/d assigned to shelf areas outside the dataset coverage.

While the use of the variable- $K$  field allows insight into the effect of seabed heterogeneity on local and global wave pumping rates, uncertainties in the  $K$  dataset suggest the variable  $K$  scenario is no more reliable than the single  $K$  scenario. We identified independent (but quite discordant) representations of seabed geology [NAVO, 2013; Dutkiewicz et al., 2015], and for the purposes of this study, selected the one that appeared most reasonable in coastal areas [NAVO, 2013]. The  $K$  data spatial resolution was coarser than wave and bathymetry data, and sediment-based  $K$  values have orders-of-magnitude uncertainty [e.g. Freeze and Cherry, 1979]. Because of the strong control of  $K$  on exchange, refinement of process-based benthic exchange estimates will require more detailed and consistent characterization of benthic sediment texture and associated hydraulic properties.

All calculations were made with custom-built Matlab scripts and functions (Figure C.2). Wave data for each grid in the domain were downloaded, transformed,

resampled (2 minute resolution), and merged into a single grid with hierarchical-preference given to the higher-resolution dataset (Figures C.3 and C.4 show sensitivity to wave data and resampled resolutions). Wave pumping was only calculated for seabeds shallower than 200 m as wave pumping is minimal below that depth [e.g. Riedl et al., 1972]. This encompasses the vast majority of continental shelf area [e.g. Riedl et al., 1972; Hall, 2002], so *continental shelf* in this work refers to seabed above the 200m isobath.

## 4.3 Results

### 4.3.1 Global Wave Pumping Rates and Patterns

Volumetric wave pumping on the continental shelf over the 31-year study period averaged  $1.8 \times 10^5 \text{ km}^3/\text{yr}$  with a range of  $1.3 \times 10^5$  to  $2.3 \times 10^5 \text{ km}^3/\text{yr}$  (Figure 4.2a). These rates would flush the ocean every 7600 years (Figure 4.1a, Tables 1, C.2). Four timesteps in July and August 1999 below this range, with rates as low as  $7.4 \times 10^4 \text{ km}^3/\text{yr}$  (Black arrows in Figure 4.2), are likely due to erroneous wave inputs. Wave pumping velocities averaged 6.1 m/yr and ranged from zero to a maximum of  $8.0 \times 10^2 \text{ m/yr}$  at Coral Bank, a shoal in the highly energetic southern Indian Ocean (pink circle; Figure 4.1). Average wave pumping velocity exceeded 1 m/yr over 16% of shelf area and was less than 1 mm/yr over 3% of shelf area.

Wave pumping velocities varied with latitude and between the seven ocean basins, but the majority of volumetric wave pumping occurs in the Northern Hemisphere, where larger continental shelves offset higher wave pumping velocities in the Southern Hemisphere (Figures 4.1b, 4.2). Average wave pumping rates were generally similar among the temperate ocean basins, but were low in the North Pacific, with its deep shelves and low wave energy (Table 4.1). Northern Hemisphere shelves comprise 69% of global shelf area and host 64% of global volumetric wave pumping (Figure 4.1b), even though  $h_w$  and  $L_w$  in the Southern Hemisphere exceeded Northern Hemisphere values by 118% and 135%. Volumetric wave pumping had a moderate correlation to shelf area at a given latitude ( $R^2=0.51$ ; Figure 4.1b). However, no clear trend was observed between wave pumping velocities and latitude. Patterns of wave pumping velocities with latitude were different in Northern and Southern Hemispheres and observed patterns could not be attributed to known astronomical, atmospheric or meteorological patterns. Wave pumping was markedly low in both circumpolar oceans because of permanent and seasonal ice cover—especially in the deep Southern Ocean (Tables 4.1, C.2). Ocean

flushing rates depend on basin volumes and wave pumping rates. Thus, the North Atlantic flush 3-4 times faster than other temperate basins, which have smaller shelves, and the extremely wide-shelved Arctic Ocean flushes twice as fast as the North Atlantic (Tables 4.1, C.2).

Wave pumping velocities and volumes have seasonal signals whose amplitudes and phases vary by latitude and basin (Figure 4.2). Seasonality was highest in circumpolar oceans where late summer highs exceeded winter lows by approximately about four times (Figure 4.2). The subpolar maxima preceded ice formation in late autumn and the minima occurred in winter when sea ice inhibited wave development and propagation (Figures 4.1a, 4.2e). Arctic wave pumping was generally low during winters with greater ice extent (e.g. 1992-4) and high during winters when ice coverage was low (e.g. 1980-9; Figure 4.2). Peak wave pumping can be traced forward in time from these Arctic summer maxima toward subtropical winter maxima (red arrows in Figure 4.2e). This pattern is present but less pronounced in the Southern Hemisphere. The peaks decreased in amplitude and broadened along this path resulting in temperate ocean basins with less pronounced seasonality—maximum annual rates exceed the minimum by only about one third (Figure 4.2a-d). A smaller biannual peak was often present at mid- to low-latitudes, especially in the South Pacific and Indian Oceans (Figure 4.2). This secondary peak varied annually in time and magnitude so it is muted in inter-year averages (Figure 4.2d).

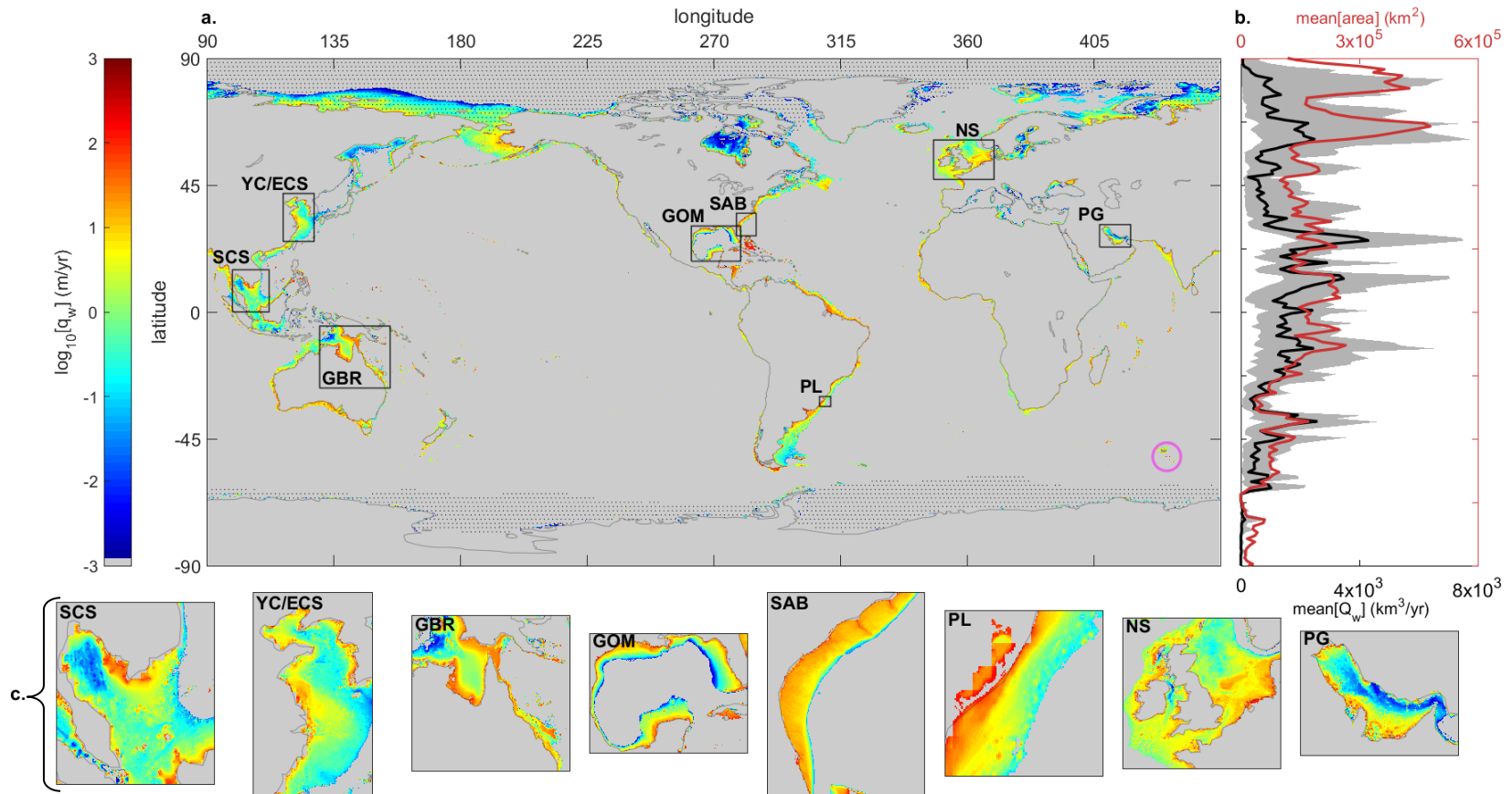


Figure 4.1. a) Time-averaged wave pumping rates in the single K scenario. Stippling indicates ocean area with sea ice > 30% of scenario duration. Pink circle around Coral Bank is location of highest wave pumping rate. b) Total volumetric wave pumping rate (black line is mean, grey region is  $\pm 1$  ) and shelf area (red line) by latitude. c) Eight regional maps of the South China Sea (SCS), Yellow/East China Seas (YS/ECS), Great Barrier Reef (GBR), Gulf of Mexico (GOM), South Atlantic Bight (SAB), Patos Lagoon (PL), North Sea (NS), and Persian Gulf (PG).

Table 4.1: Wave pumping rates for single K (*and variable K*) scenarios for the globe, the seven ocean basins discussed in the paper, and the Mediterranean and Black “Seas” (basin delineations shown in Figure C.5)

	Volumetric wave pumping ( $Q_w$ )		Avg. wave pumping rate ( $q_w$ )		Avg. $Q_w$ / basin area	Avg. $Q_w$ / shoreline length	Basin flushing time
	$(\text{km}^3/\text{yr})$	$(\text{km}^3/\text{yr})$	$(\text{m}/\text{yr})$	$(\text{m}/\text{yr})$	$(\text{km}^3/\text{yr}/\text{km}^2)$	$(\text{km}^3/\text{km}/\text{yr})$	$(\text{yr})$
<b>Global</b>	$1.8 \times 10^5$	$(1.7 \times 10^5)$	$6.1 \times 10^0$	$(5.7 \times 10^{-3})$	$4.8 \times 10^{-4}$	$5.0 \times 10^{-1}$	$7.6 \times 10^3$
<b>North Atlantic</b>	$5.0 \times 10^4$	$(1.7 \times 10^4)$	$1.0 \times 10^1$	$(3.5 \times 10^{-3})$	$1.2 \times 10^{-3}$	$3.6 \times 10^{-1}$	$2.9 \times 10^3$
<b>South Atlantic</b>	$1.6 \times 10^4$	$(2.9 \times 10^3)$	$8.5 \times 10^0$	$(1.6 \times 10^{-3})$	$4.0 \times 10^{-4}$		$1.0 \times 10^4$
<b>North Pacific</b>	$3.3 \times 10^4$	$(2.6 \times 10^4)$	$5.5 \times 10^0$	$(4.3 \times 10^{-3})$	$4.1 \times 10^{-4}$	$2.4 \times 10^{-1}$	$1.0 \times 10^4$
<b>South Pacific</b>	$2.9 \times 10^4$	$(5.6 \times 10^4)$	$8.7 \times 10^0$	$(1.6 \times 10^{-2})$	$3.3 \times 10^{-4}$		$1.1 \times 10^4$
<b>Indian Ocean</b>	$3.0 \times 10^4$	$(5.8 \times 10^4)$	$9.6 \times 10^0$	$(1.9 \times 10^{-2})$	$4.3 \times 10^{-4}$	$4.5 \times 10^{-1}$	$8.8 \times 10^3$
<b>Arctic Ocean</b>	$1.3 \times 10^4$	$(3.8 \times 10^3)$	$2.1 \times 10^0$	$(6.1 \times 10^{-4})$	$8.5 \times 10^{-4}$	$3.0 \times 10^{-1}$	$1.4 \times 10^3$
<b>Southern Ocean</b>	$4.9 \times 10^2$	$(8.2 \times 10^1)$	$2.3 \times 10^{-1}$	$(3.8 \times 10^{-5})$	$1.8 \times 10^{-5}$	$2.7 \times 10^{-2}$	$1.5 \times 10^5$
<b>Seas</b>	$3.1 \times 10^3$	$(2.0 \times 10^3)$	$2.5 \times 10^0$	$(1.6 \times 10^{-3})$	$8.3 \times 10^{-4}$		$1.5 \times 10^3$

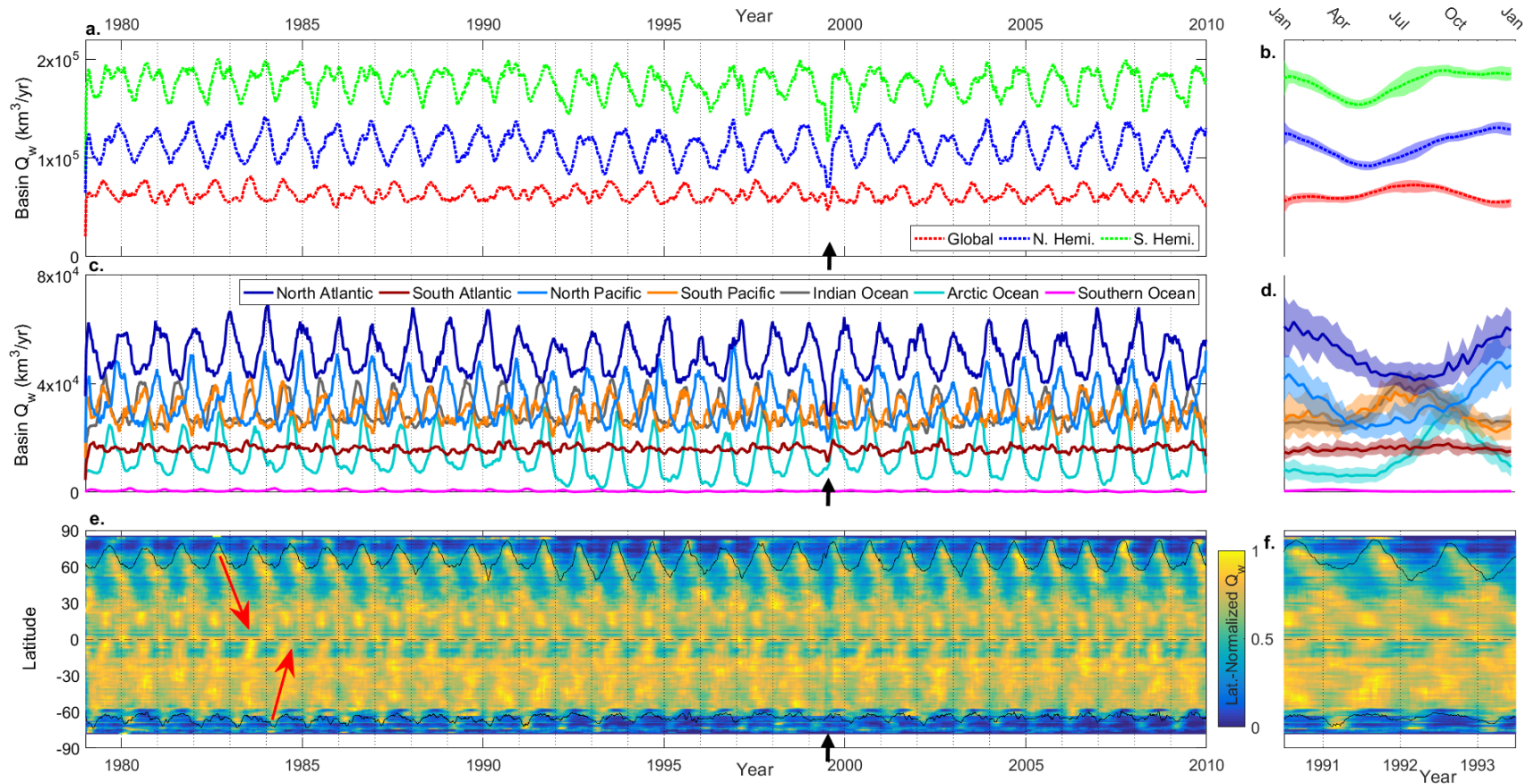


Figure 4.2. Wave pumping by basin and latitude for the single-K global scenario. a & c) One-month moving average of volumetric wave pumping for the 31-year scenario. b & d) Average annual volumetric wave pumping (solid lines)—shaded regions encompass  $\pm 1$  31-year scenario. Black contours show latitude where 30% of ocean cells are ice-covered. Red arrows illustrate movement of latitudinal peak annual volumetric wave pumping toward equator with time. Black arrows beneath July/August 1999 highlight abnormally-low wave pumping, likely from anomalous wave data.

### **4.3.2 Effect of Seabed Heterogeneity**

The consideration of heterogeneous seabed sediments resulted in a global volumetric pumping rates that was just 6% lower than the single-K scenario, but introduced additional inter- and intra-basin variability. Southern Hemisphere K values were nearly double Northern Hemisphere values, which resulted in 62% of global volumetric wave pumping occurring in the Southern Hemisphere, up from 36%. Higher-K sediments offshore of Australia, Oceania, and the Asia-Pacific region resulted in a near doubling of South Pacific and Indian Ocean wave pumping rates. In the Atlantic and North Pacific, lower-K sediments dampened wave pumping to just 46% of single-K scenario rates. Wave pumping rates in the Arctic and Southern Oceans were also greatly reduced due to lower K values. The range of wave pumping rates broadened greatly—the majority of volumetric wave pumping occurred at greater velocities over a smaller area while wave pumping velocities decreased over a majority of the shelf area (Figure C.6). The shelf area where wave pumping velocity exceeded 1 m/yr increased from 16% to 26%. The area where wave pumping was less than 1 mm/yr also increased, from 3% to 18%.

### **4.3.3 Effect of Extreme Events**

Wave pumping rates in the SAB were analyzed to better understand the amount of wave pumping associated with calm and energetic periods. Wave pumping averaged 12 m/yr, which exceeded global rates, and spanned two orders of magnitude (Figures 4.3, C6). The number of wave pumping events with fluxes in the 99<sup>th</sup> percentile ranged from 1 to 10 per year. Annually, wave pumping events in the 99<sup>th</sup> percentile accounted for 0.2-8% (mean=3%) of volumetric wave pumping, events above the 90<sup>th</sup> percentile drove 8-30% (mean=21%), and just 27-39% (mean=33%) of volumetric wave pumping occurred during calm periods when wave pumping rates were within the 50<sup>th</sup> percentile (Figure 4.3c, d).

Tropical cyclones are responsible for the most extreme periods of SAB wave pumping, but not the majority of extreme events. Tropical cyclones were rare, with just 25 of the 142 extreme wave pumping events that peaked above the 99<sup>th</sup> percentile (Figure 4.3a) occurring when a tropical cyclone was *near* (within one day of entering or leaving) the SAB region [Knapp et al., 2010]. Tropical cyclones drove 7 of the 10 highest wave pumping events—the four events with highest wave pumping rates were associated with category 2 and 3 hurricanes Hugo, Floyd, Bonnie, and Fran, respectively (Figure 4.3a). In total, 92 distinct tropical cyclones tracked through the SAB between January 1979 and December 2009 [Knapp et al., 2010]. A tropical cyclone was near the SAB region 1.1% of the time during which 2.1% of total volumetric wave pumping occurred (Figure 4.3c, d).

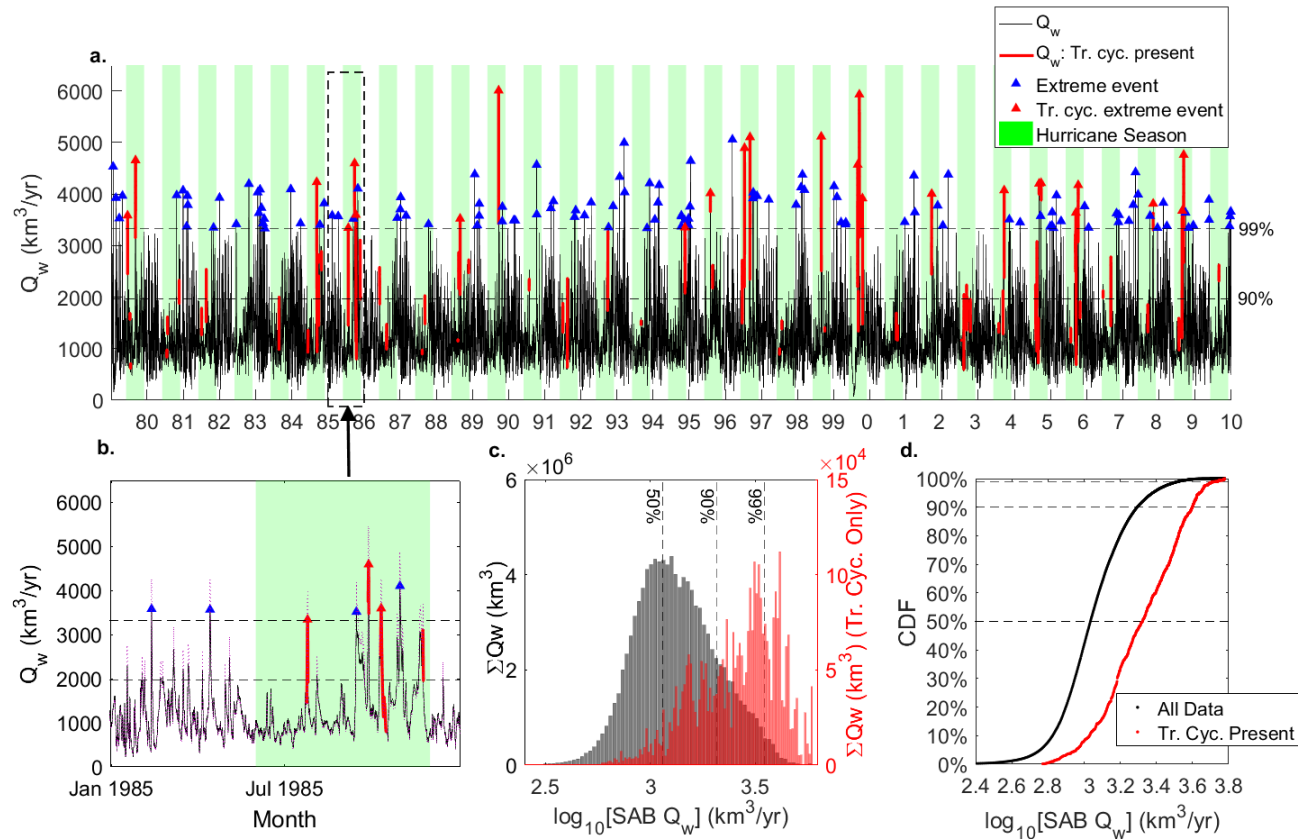


Figure 4.3. Comparison of SAB wave pumping during normal periods and tropical cyclone (Tr. Cyc.) events. a.) Time series of all wave pumping and extreme events. b.) Close-up view of 1985 (dashed box in a), when 4 tropical cyclones passed through the region and 7 extreme events occurred. Dotted purple line shows potential future with mild overall decrease to wave pumping rates but increase during extreme events. c.) Flux-weighted volumetric wave pumping histogram. d.) Empirical CDF showing cumulative probability wave-pumping event with given strength.

## 4.4 Discussion

### 4.4.1 Comparison to Previous Estimates and Global Discharge Rates

Global and SAB wave pumping rates compare well with previous wave pumping estimates. The SAB volumetric wave pumping rate reported herein is 94.4% of the value reported for the six-year period considered by Riedl et al. [1972]. Riedl et al. extrapolated the SAB rate to a global scale, which is 54% of the value reported herein. This difference is expected and reasonable because the SAB is relatively calm [e.g. Riedl et al., 1972] – SAB  $h_w$  and  $L_w$  are 64.3% and 96.7% of global averages, respectively.

Volumetric wave pumping exceeds estimates of fresh continental discharge through surface and subsurface pathways. Our global volumetric wave pumping is over four times the global river discharge estimated by Santos et al. (2012). In the contiguous United States (US), stream discharge, recorded for 60% of the area, averages  $1100 \text{ km}^3/\text{yr}$ . This value can be scaled up to about  $1800 \text{ km}^3/\text{yr}$  for the entire contiguous US, which is 67% of the volumetric wave pumping we calculate for continental shelves offshore of the contiguous US ( $2700 \text{ km}^3/\text{yr}$ ). Sawyer et al. [2016] calculated contiguous US coastal waters receive  $15 \text{ km}^3/\text{yr}$  of fresh submarine groundwater discharge (SGD) and Zekster [2000] estimated fresh SGD averages  $2.4 \times 10^3 \text{ km}^3/\text{yr}$  across the globe—these are 0.5% and 1.4% of the volumetric wave pumping we calculate for those areas, respectively.

Our estimated volumetric wave pumping rate exceeds the only previous global-scale calculations of SGD, which are based on  $^{228}\text{Ra}$  inventories [Kwon et al., 2014; Cho and Kim, 2016], by 47%. The Ra method traces saline SGD well, but likely underestimates both the fresh component of SGD [Michael et al., 2011; Mulligan and

Charrette 2006; Gonnee et al., 2008; Cho and Kim, 2016] and fluxes with residence times much less than the 5.75-year  $^{228}\text{Ra}$  half-life (such as wave pumping). Thus, Ra-based methods likely exclude a large portion of SGD driven by wave pumping, which is a significant, if not dominant, component of total SGD. Similarly, wave pumping accounts for 25 times the flux calculated for global hydrothermal circulation along mid ocean ridges of  $7.1 \times 10^3 \text{ km}^3/\text{yr}$  [Johnson and Pruis, 2003].

#### **4.4.2 Sources of Inaccuracy**

There are several sources of inaccuracy that arise from the nature of the wave model, differing dataset resolutions, resampling, and the homogeneous treatment of K. Wave parameters and resulting wave pumping rates are overestimated in icy regions, because wave parameters inputs generated by Wavewatch III hindcast models neglect wave damping and scattering by sea ice for the sake of computational efficiency (WW3DG). Dataset resolution issues also lead to over- or under-estimation of wave pumping, especially along shorelines and where bathymetry variation occurs over smaller scales than the wave dataset resolution. Wavewatch III-predicted waves neglect the shoaling effect and overestimate wave parameters (WW3DG) in locations where the mean depth of the coarse 30 arcsecond cell greatly exceeds that of shallow bathymetric discretized in the 2 arcsecond wave pumping scenarios. Thus, waves and wave pumping are likely overestimated in areas with high seabed slopes, like along shorelines and at shoals like Coral Bank. Wave pumping is underestimated along shorelines where discretization of the coarse wave parameter inputs result in coastal cells with no assigned wave data and an inability to estimate wave pumping in some coastal ocean cells (e.g. Figure 4.1c SCS). Uncertainty resulting from resolution issues is less in regions with fine-resolution wave datasets (Table C.1). Shelf sediments

generally coarsen shoreward []. So, the homogeneous K leads to near-shore underestimation and deep-water overestimation of wave pumping. Taken together, wave pumping uncertainty is greatest in nearshore areas where wave data is coarse and bathymetry is variable. However, these sources of inaccuracy likely cancel one-another minimizing their effect on the overall pumping rate.

#### **4.4.3 Effect of Climate Variability on Wave Pumping**

The results of this study can be expanded to predict how future changes in wave energy may affect wave pumping rates and patterns. A global observational study of wind and wave changes [Young et al., 2011] and general circulation model (GCM) predictions [e.g. Hemer et al., 2011; Camus et al., 2017] suggests that global wave energy will remain neutral or decrease slightly, on average, during the current century, but that frequency and intensity of extreme events will increase. This increase will be greatest in the Southern Ocean and north of 45° N [IPCC 2013] with mean wave heights in the southern hemisphere increasing by up to 4% by 2100 [Hemer et al., 2011; Camus et al., 2017]. Northern hemisphere wave heights will likely decrease by 2-4% over that period. In some areas, wave pumping increases from these extreme events, may offset decreased wave intensity during calm periods, especially because wave pumping rates during large storm events vastly exceed rates during calm periods (Figure 4.3). For example, in the SAB in 1985, wave pumping rates of 21 unique events exceeded the 90<sup>th</sup> percentile and 7 events breached the 99<sup>th</sup> percentile (Figure 4.3b). An overall wave pumping decrease of 4% could be offset by an increase in frequency (4 additional events), intensity (15%), or a combination of the two (e.g. 2% and 2 additional events) for extreme events in the 90<sup>th</sup> percentile (dotted purple line in Figure 4.3b shows varied intensity example).

GCM models also predict future changes to wave pumping seasonality over much of the globe. Average wave heights may increase drastically in the Arctic due to reduced sea ice cover [IPCC, 2013], with a complete loss of Arctic Ocean sea ice driving a potential increase of 2-3 times and reduced annual periodicity (Figure 4.2). Increased seasonality is expected along the wide continental shelves in North America, Asia, and South America, a finding confirmed by historical records [Hemer et al., 2013]. For instance, observations of SAB wave heights over the past several decades indicate that intensity and occurrence of extreme events have increased during hurricane season because of elevated cyclonic intensity, while winter extratropical storm-generated waves have remained steady over that same period [Komar and Allan, 2008]. However, in the SAB scenario, an average of less than one 99<sup>th</sup> percentile event was driven by a tropical cyclone each year (Figure 4.3a). So, a large increase to intensity or frequency would be required for these tropical cyclones to offset reduced wave pumping during the rest of the year.

#### **4.4.4 Effect of Wave Pumping on Coastal Ocean Chemistry**

Shelf sediments are important hosts to biogeochemical reactions [e.g. Seitzinger et al., 2006; Gattuso et al., 1998; Chen, 2010], so orders-of-magnitude spatiotemporal wave pumping variability directly affects water column chemistry [e.g. Berg and Huettel, 2008; Berg et al., 2009; Chipman et al., 2016]. Ultimately, this understanding of spatial and temporal wave pumping variability can aid predictions of locations and times the ocean may be particularly vulnerable to problems such as eutrophication, which can be mitigated or exacerbated by benthic reactivity [e.g. Chapelle et al., 1994; Rao and Charette, 2012].

Future changes to wave pumping rates and variability will propagate to affect chemical reactivity in shelf sediments, and combined with increased coastal nutrient loads, will have meaningful impacts on carbon and nutrient cycling. Coastal eutrophication indicators based on global terrestrial nutrient application show that eutrophication risk will increase over the next several decades with regional variability governing the intensity of that increase [Beusen et al., 2009; Garnier et al., 2010; Mayorga et al., 2010; Seitzinger et al., 2010]. Potential nutrient mitigation will increase in areas expected to see increased wave pumping or where seasonal wave pumping increases correspond to periods of high nutrient effluence. One such area is the U.S. east coast where high summer nutrient loads [e.g. Ullman et al., 2002] could be offset by predicted preferential increases to summer wave pumping rates [Hemer et al., 2013]. Similarly, we show that wave pumping in the Arctic should increase following sea ice reductions, which should offset increased terrestrial flux of nutrients and carbon associated with melting permafrost [e.g. Kipp et al., 2018]. Conversely, eutrophication risk will increase where wave pumping decreases or is temporally mismatched to seasonal nutrient discharge. One region of concern is northern Europe where coastal waters with an already high eutrophication risk [e.g. Seitzinger et al., 2010] may see reduced wave pumping rates and a decline in reactivity [Hemer et al., 2011; Perez et al., 2015].

#### **4.5 Conclusion**

We present global-scale process-based estimates of rates and patterns of wave-driven benthic water exchange across the global ocean—the first process-based calculation of submarine groundwater discharge at the global scale. The annual volumetric wave pumping rate of  $1.8 \times 10^5 \text{ km}^3/\text{yr}$  is a significant portion of the global

water budget—greater than previous estimates of both total SGD from all drivers and global river discharge. Wave pumping varies by orders of magnitude in time and space. Generally, small-scale variability is more pronounced than variability over larger scales. A regional analysis shows that extreme wave events account for a disproportionate amount of wave pumping and that tropical cyclones drive the most extreme events.

These estimates suggest where and when shelf sediments may play an active role in the processing of chemicals in the coastal ocean and allow us to better predict how coastal systems will respond to climate variability. Wave pumping rates are generally expected to decrease, especially in the Northern Hemisphere, as wave energy declines in coming years. This decrease may be partially offset as the intensity and frequency of extreme events increases, especially at high latitudes. While decreased wave-pumping induced chemical reactivity will likely decrease over much of the globe, reactivity will likely increase in areas with increased net wave pumping, such as the Arctic, or where increased seasonal wave pumping is in phase with nutrient inputs, as along the US Eastern Seaboard.

## Chapter 5

### CONCLUSIONS

These studies focus on benthic exchange through seabed aquifers and how benthic exchange may be quantified over a variety of different temporal and spatial scales, with an emphasis on wave-induced exchange. The efficiency of seepage meters and the impact of wave action on seepage meter measurements were studied. These results confirm the efficacy of seepage meters in measurements of ambient groundwater discharge, even in the presence of wave action and quantify uncertainties that may be expected in those measurements. Field measurements and numerical models of benthic exchange: 1) showed wave-induced exchange exceeded tide-induced exchange and exchange induced by currents over bedforms, 2) validated a wave parameter-based analytical solution of wave-induced exchange with pressure-based calculations, and 3) and detailed the effect of aquifer characteristics on the rate, depth, and residence time of wave-induced exchange. Wave-induced exchange was modeled for the entire Earth between 1979 and 2010 using global ocean bathymetry, wave parameters from a global wave model, and maps of global shelf sediment cover as input. The model is the first process-based estimate of groundwater discharge calculated over a global scale. Results show how exchange rates vary over a variety of spatial and temporal scales, the effect of ice cover on exchange in the circumpolar oceans, and the effect of extreme events on global wave pumping. Ultimately, chemical cycling and the fate and fluxes of nutrients across the aquifer-ocean interface

is controlled strongly by these physical flows, so in turn is dependent on the hydrologic forcing mechanisms acting on coastal seas across the globe.

### **5.1 Spatial and Temporal Variability in Benthic Exchange**

Benthic exchange rates varied over every temporal and spatial scale examined in these studies. In the wave flume, field study, and small-scale numerical models wave pumping rates varied with pressure oscillations at wavelength and wave period scales. Benthic exchange rates also varied with changes to seabed sediment hydraulic conductivity, which varies at the Holts Landing site and elsewhere by orders of magnitude over scales of centimeters to kilometers and longer. Over longer time scales, weather-induced hydrodynamic variability caused benthic exchange rates to vary over orders of magnitude between calm and highly-energetic periods. Variability was much less pronounced over the longest scales of time and space. The global wave pumping rate varied by less than a factor of 2 over the 31-year scope of this study. Similarly, regionally important events, such as tropical storms in the South Atlantic Bight, occur over such limited areas to have minor impacts on the global wave pumping rate. Only seasonal-scale variability from annual weather patterns or sea-ice cover propagate to affect the global pumping rate.

### **5.2 Working Toward Larger Scale Benthic Exchange Estimates**

Estimates of benthic exchange at a discrete location are useful because they inform estimates of exchange over broad spatial scales or feed into estimates of chemical cycling. For instance, field validation and process-scale models of the wave pumping analytical solution supported its use in regional and global-scale estimates of wave pumping in this study. Ideally, areal estimates of benthic exchange could be

combined with broad knowledge of surface and groundwater chemical parameters in simple models to identify chemical cycling rates to better estimate the impact of benthic exchange on chemistry over large areas. Identifying and modeling the relationships between benthic exchange and chemical parameters should be a future goal.

### **5.3 Implications**

Quantifying chemical pathways in coastal oceans and estuaries is crucial for predicting ecosystem health, but is difficult in practice because of temporal and spatial variability in rates of benthic exchange that fuels chemical reactions in shallow coastal waters. Benthic exchange rates are often extrapolated across large and hydrodynamically and geologically complex areas in an attempt to calculate a discrete value that can represent exchange rates for the region. Similarly, rates may be extrapolated over time without considering temporal variability in the driving mechanisms. The spatio-temporal variability of benthic exchange presented in this document show that such extrapolation across time and space can be problematic. However such extrapolation may be reasonable if it is guided by knowledge of the temporal and spatial variability of the forces and seabed characteristics that control exchange rates.

Chemical reaction rates in the shallow seabed aquifer are controlled by the supply of reactants from groundwater, sediments, and surface water, and the reaction timescale and groundwater residence times. The variability of benthic exchange rates measured in this study will affect both the fluxes of solutes from surface waters and the residence time of waters in the mixing zone, and thus chemical reaction rates. Therefore a single value for benthic exchange over broad spaces and times is likely

inadequate as a precursor for estimation of chemical reaction rates. Thus the purpose should be considered when extrapolating exchange rates across space and time.

#### **5.4 Recommendations for Future Work**

Important gaps remain in our understanding of how benthic exchange mechanisms operate in the real world including the rates associated with different driving mechanisms and how these rates vary in space and time, chemical and fluid pathways in the subsurface, and how different benthic exchange mechanisms sum together. These gaps may be filled in the future by: 1) studies considering a wider range of environments and mechanisms, 2) quantifying residence times and exchange depths in addition to fluid fluxes, 3) modeling reactive transport associated with benthic exchange in the seabed aquifer, and 4) working with existing large-scale datasets of hydrodynamic and seabed parameters at high-resolution to predict how different operate alone and in conjunction.

Future studies should focus on understanding how benthic exchange rates vary over a wider range of environments and how mechanisms interact to drive benthic exchange. In this study, field measurements were collected during temperate, relatively calm conditions at a shallow, protected, easy to access field site. Future investigation should consider a wider range of conditions to determine if the patterns observed here hold true as conditions change. Geologic heterogeneity, and aquifer properties including hydraulic conductivity and storativity, have profound impacts on flow and transport processes in the seabed aquifer, but we do not have simple-to-apply solutions that adequately include these factors in calculations of exchange rates, depths, and residence times. Numerical models that include heterogeneity over a variety of spatial scales can be used to assess the importance of geology on benthic

exchange and whether homogenous models can accurately represent real-world systems. Analytical equations exist for many of the mechanisms that drive benthic exchange, but these equations yield no insight into how different mechanisms interact. Understanding these interactions was an unachieved goal of the field study and an accompanying modeling effort. Still, understanding these interactions is of great importance, and will likely be best achieved through numerical modeling.

Most of the work on estimating benthic exchange has focused on the rates of exchange with much less attention paid to estimating exchange depths and residence times. The studies that have looked at exchange depths have noted that the mechanism lengthscale, sediment properties, and interactions with other mechanisms (e.g. ambient discharge) all affect the depth of mixing. Few studies have created simple models that are more widely applicable. The simple empirical model presented herein allows estimation of exchange depth based on sediment and wave characteristics. Similar models to predict residence time and exchange depth for this and other mechanisms should be pursued.

Ultimately, benthic exchange is important because of its direct impact on the ecosystem services provided by the seabed aquifer. To estimate these ecosystem services over regional and global scales, though, relatively simple models relating benthic exchange rates and water chemistry to reaction rates are required. Future studies that combine measurements of benthic exchange rates, *in situ* chemistry, and chemical fluxes across the sediment-water interface will likely be most successful. A variety of probes and sampling systems are available to measure *in situ* chemistry or collect samples for analysis. Eddy correlation techniques are also maturing and becoming easier to deploy, and analyze. If simple models relating chemical changes to

benthic exchange rates can be built from the combined results of these three techniques, reasonable predictions of chemical cycling over wide areas should be attainable.

One method of achieving this goal of simple, predictive models would be to extend the concept of ‘reaction significance factors’ (RSF) from the hyporheic literature into the coastal realm [Harvey and Fuller, 1998; Harvey et al, 2013]. This dimensionless index quantifies the relationship between hydrologic (flux and residence time) and biogeochemical factors (intrinsic reaction rate) to estimate the effect of different exchange zone types on downstream water quality. This is achieved by including both small scale controls (residence time and intrinsic reaction rate) and the cumulative effects of river water turnover through all similar exchange zones over a given distance of river transport. This concept works well in fluvial systems where currents and chemical evolution are directional in nature, but creating a similar system is more challenging in oscillatory coastal environments where fluid and chemical pathways are more difficult to identify and quantify, and no direct analogue exists for the “river discharge” term. A substitute would be required—possibly water depth or an embayment flux term (Figure 5.1).

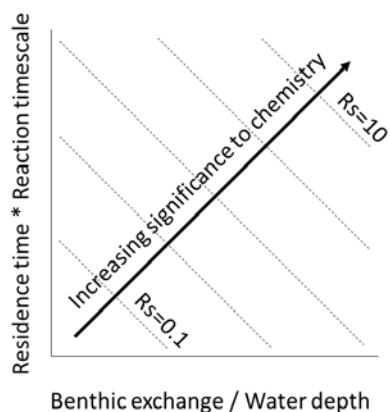


Figure 5.1 – Sample idea for a Marine Significance Factor

If flux/chemistry models allow prediction of chemical cycling then areal benthic exchange models and the datasets needed to construct them will become more important. Many estuary-, regional-, and global-scale hydrodynamic models already exist with results that may be used to estimate different exchange rates associated with different mechanisms. Mature hydrodynamic models can also make reasonable predictions of future hydrodynamic regimes, which can be applied to understand how benthic exchange rates and their effect on chemistry is likely to vary with changing climate. Ultimately it is these areal models that will allow estimation of the chemical cycling that occurs in the shallow seabed aquifers across our continental shelves.

## REFERENCES

- Amante, C., & Eakins, B. W. (2009). ETOPO1 1 arc-minute global relief model: Procedures, data sources and analysis: National Oceanic and Atmospheric Administration Technical Memorandum NESDIS NGDC-24, 19 p., doi: 10.7289.
- Anderson, W. J., and R. Emanuel. (2010). Effect of interannual climate oscillations on rates of submarine groundwater discharge. *Water Resources Research* **46**, no. 5: W05503.
- Andres, A. S., Michael, H., Russoniello, C. J., Fernandez, C., He, C., & Madsen, J. A. (2017). *Report of Investigation no. 80: Investigation of Submarine Groundwater Discharge at Holts Landing State Park, Delaware: Hydrogeologic Framework, Groundwater Level and Salinity Observations*. Newark, DE.
- Asbury, C. E. (1990). The role of groundwater seepage in sediment chemistry and nutrient budgets in Mirror Lake, New Hampshire. PhD Thesis. Cornell University.
- Bardini, L., Boano, F., Cardenas, M. B., Revelli, R., & Ridolfi, L. (2012). Nutrient cycling in bedform induced hyporheic zones. *Geochimica et Cosmochimica Acta*, *84*, 47–61. <https://doi.org/10.1016/j.gca.2012.01.025>
- Belanger, T. V., and M. T. Montgomery. (1992). Seepage Meter Errors. *Limnology and Oceanography*. **37**, no. 8: 1787–1795.
- Berg, P., & Huettel, M. (2008). Integrated benthic exchange dynamics. *Oceanography*, *21*(4), 164–167.
- Berg, P., Glud, R. N., Hume, A. C., Stahl, H., Oguri, K., Meyer, V., & Kitazato, H. (2009). Eddy correlation measurements of oxygen uptake in deep ocean sediments. *Limnology and Oceanography-Methods*, *7*. <https://doi.org/10.4319/lom.2009.7.576>.

- Berg, P., Røy, H., Janssen, F., Meyer, V., Jørgensen, B. B., Huettel, M., & De Beer, D. (2003). Oxygen uptake by aquatic sediments measured with a novel non-invasive eddy-correlation technique. *Marine Ecology Progress Series*, 261, 75–83. <http://doi.org/10.3354/meps261075>
- Beusen, A.H.W., A.F. Bouwman, H.H. Dürr, A.L.M. Dekkers and J. Hartmann. (2009). Global patterns of dissolved silica export to the coastal zone: Results from a spatially explicit global model. *Global Biogeochemical Cycles*, 23, GB0A02, doi:10.1029/2008GB003281
- Boano, F., Harvey, J.W., Marion, A., Packman, A.I., Revelli, R., Ridolfi, L., & Wörman, A. (2014). Hyporheic flow and transport processes: Mechanisms, models, and biogeochemical implications. *Reviews of Geophysics*, 52, <http://doi.org/10.1002/2012RG000417>.
- Boudreau, BP, Huettel, M, Forster, S, Jahnke, R A, MacLachlan, A, Middelberg, JJ, Nielson, P, Sansone, F, Taghon, G, Van Raaphorst, W, Webster, I, Weslawski, JM, Wiberg, P, and Sundby, B (2001) Permeable marine sediments: overturning an old paradigm. *EOS, Transactions, American Geophysical Union* 82: 133–136.
- Bourke, M. F., Marriott, P. J., Glud, R. N., Hasler-Sheetal, H., Kamalanathan, M., Beardall, J., ... Cook, P. L. M. (2016). Metabolism in anoxic permeable sediments is dominated by eukaryotic dark fermentation. *Nature Geoscience*, 1(November). <http://doi.org/10.1038/NNGEO2843>
- Bratton, J. F., Böhlke, J. K., Manheim, F. T., & Krantz, D. E. (2004). Ground water beneath coastal bays of the Delmarva Peninsula: ages and nutrients. *Ground Water*, 42(7), 1021–1034. <https://doi.org/10.1111/j.1745-6584.2004.tb02641.x>
- Briggs, M. A., Lautz, L. K., & Hare, D. K. (2014). Residence time control on hot moments of net nitrate production and uptake in the hyporheic zone. *Hydrological Processes*, 28(11), 3741–3751. <http://doi.org/10.1002/hyp.9921>
- Briggs, M. A., Lautz, L. K., Buckley, S. F., and Lane, J. W. (2014). Practical limitations on the use of diurnal temperature signals to quantify groundwater upwelling. *Journal of Hydrology*, 519, Part B. <https://doi.org/10.1016/j.jhydrol.2014.09.030>
- Burnett, W., and H. Dulaiova. (2003). Estimating the dynamics of groundwater input into the coastal zone via continuous radon-222 measurements, *Journal of Environmental Radioactivity* 69, no. 1-2: 21-35.

- Burnett, W.C., P.K. Aggarwal, A. Aureli, H. Bokuniewicz, J.E. Cable, M.A. Charette, E. Kontar, S. Krupa, K.M. Kulkarni, A. Loveless, W.S. Moore, J.A. Oberdorfer, J. Oliveira, N. Ozyurt, P. Povinec, A.M.G. Privitera, R. Rajar, R.T. Ramessur, J. Scholten, T. Stieglitz, M. Taniguchi, and J.V. Turner. (2006). Quantifying submarine groundwater discharge in the coastal zone via multiple methods, *Science of the Total Environment* **367**, no. 2-3: 498-543.
- Cable, J. E., J. B. Martin, and J. Jaeger. (2006). Exonerating Bernoulli? On evaluating the physical and biological processes affecting marine seepage meter measurements. *Limnology and Oceanography: Methods* **4**: 172–183.
- Cable, J. E., W. C. Burnett, J. P. Chanton, D. R. Corbett, and P. H. Cable. (1997). Field Evaluation of Seepage Meters in the Coastal Marine Environment, *Estuarine, Coastal and Shelf Science* **45**, no. 3: 367-375.
- Camus, P., Losada, I. J., Izaguirre, C., Espejo, A., Menéndez, M., & Pérez, J. (2017). Statistical wave climate projections for coastal impact. *Earth's Future*, *5*, 918–933. <http://doi.org/10.1002/2017EF000609>
- Cardenas, M. B., & Wilson, J. (2006). The influence of ambient groundwater discharge on exchange zones induced by current–bedform interactions. *Journal of Hydrology*, *331*, 103–109. <http://doi.org/10.1016/j.jhydrol.2006.05.012>
- Cardenas, M. B., & Wilson, J. (2007). Exchange across a sediment–water interface with ambient groundwater discharge. *Advances in Water Resources*, *30*(301–313). <https://doi.org/10.1016/j.advwatres.2006.06.009>
- Cardenas, M. B., Cook, P. L. M., Jiang, H., & Traykovski, P. (2008). Constraining denitrification in permeable wave-influenced marine sediment using linked hydrodynamic and biogeochemical modeling. *Earth and Planetary Science Letters*, *275*(1–2), 127–137. <http://doi.org/10.1016/j.epsl.2008.08.016>
- Cardenas, M. B., J. L. Wilson, and V.A. Zlotnik. (2004). Impact of heterogeneity, bed forms, and stream curvature on subchannel hyporheic exchange. *Water Resources Research* **40** no. 8: W08307.
- Chapelle, A., Lazure, P., & Ménesguen, A. (1994). Modelling eutrophication events in a coastal ecosystem. Sensitivity analysis. *Estuarine, Coastal and Shelf Science*, *39*(6), 529–548. [http://doi.org/10.1016/S0272-7714\(06\)80008-9](http://doi.org/10.1016/S0272-7714(06)80008-9)
- Charette MA (2007) Hydrologic forcing of submarine groundwater discharge: insight from a seasonal study of radium isotopes in a groundwater-dominated salt marsh estuary. *Limnol Oceanogr* *52*:230–239

- Chen CT.A. (2010) Cross-Boundary Exchanges of Carbon and Nitrogen in Continental Margins<sup>1</sup>. In: Liu KK., Atkinson L., Quiñones R., Talaue-McManus L. (eds) Carbon and Nutrient Fluxes in Continental Margins. Global Change – The IGBP Series. Springer, Berlin, Heidelberg
- Chen, C.-T. A. (2003). New vs. export production on the continental shelf. *Deep Sea Research Part II: Topical Studies in Oceanography*, 50(6–7), 1327–1333. [http://doi.org/10.1016/S0967-0645\(03\)00026-2](http://doi.org/10.1016/S0967-0645(03)00026-2)
- Chipman, L., Berg, P., & Huettel, M. (2016). Benthic Oxygen Fluxes Measured by Eddy Covariance in Permeable Gulf of Mexico Shallow-Water Sands. *Aquatic Geochemistry*, 22(5), 529–554. <http://doi.org/10.1007/s10498-016-9305-3>
- Cho, H. M., & Kim, G. (2016). Determining groundwater Ra end-member values for the estimation of the magnitude of submarine groundwater discharge using Ra isotope tracers. *Geophysical Research Letters*, 43(8), 3865–3871. <http://doi.org/10.1002/2016GL068805>
- Cho, H.M., Kim, G., Kwon, E. Y., Moosdorf, N., Garcia-Orellana, J., & Santos, I. R. (2018). Radium tracing nutrient inputs through submarine groundwater discharge in the global ocean. *Scientific Reports*, 8(1), 2439. <http://doi.org/10.1038/s41598-018-20806-2>
- Cook, P. L. M., Wenzho, F., Glud, R. N., Janssen, F., Huettel, M., Glud, A., et al. (2007). Benthic solute exchange and carbon mineralization in two shallow subtidal sandy sediments: Effect of advective pore-water exchange. *Limnology and Oceanography*, 52(5), 1943–1963.
- Corbett, D., W. Burnett, P. Cable, and S. Clark. (1997). Radon tracing of groundwater input into Par Pond, Savannah River site *Journal of Hydrology* **203**: no. 1-4: 209-227.
- Crusius, J., Berg, P., Koopmans, D. J., & Erban, L. (2008). Eddy correlation measurements of submarine groundwater discharge. *Marine Chemistry*, 109(1–2), 77–85. <http://doi.org/10.1016/j.marchem.2007.12.004>
- Devlin, J. F. (2015). HydrogeoSieveXL: an Excel-based tool to estimate hydraulic conductivity from grain-size analysis. *Hydrogeology Journal*, 23(4), 837–844. <http://doi.org/10.1007/s10040-015-1255-0>
- Duarte C.M., Middelburg JJ, Caraco N. (2005). Major role of marine vegetation on the oceanic carbon cycle. *Biogeosciences* 2:1–8

- Dutkiewicz, A., Mueller, R. D., O'Callaghan, S., & Jonasson, H. (2015). Census of seafloor sediments in the world's ocean. *Geology*, *43*(9), 795–798. <https://doi.org/10.1130/G36883.1>
- Elliott, A. H., & Brooks, N. H. (1997). Transfer of nonsorbing solutes to a streambed with bed forms: Laboratory experiments. *Water Resources Research*, *33*(1), 137–151.
- Erikson, D. R. (1981). A Study of Littoral Groundwater Seepage at Williams Lake, Minnesota Using Separate Meters and Wells. PhD Thesis. University of Minnesota.
- Fernandez, C (2012) Relation of the spatial and temporal distribution of water quality parameters to hydrogeology at Indian River Bay, Delaware: field observations and modeling. M.S. Thesis. University of Delaware.
- Ferris, J. G. (1952). *Cyclic fluctuations of water level as a basis for determining aquifer transmissibility*. USGS Ground Water Report. Washington, D.C.
- Fetter, C. W. (2001). *Applied Hydrogeology* (4th ed.). Prentice-Hall, Inc. New Jersey
- Filippelli, G. M. (1997). Controls on phosphorus concentration and accumulation in oceanic sediments. *Marine Geology*, *139*, 231–240.
- Filippelli, G. M. (2002). The global phosphorus cycle. *Reviews in mineralogy and geochemistry*, *48*(1), 391-425.
- Freeze, R.A., and Cherry, J.A. (1979) *Groundwater*. Prentice-Hall. Englewood Cliffs, NJ. 604 p.
- Ganju, N. K. (2011). A novel approach for direct estimation of fresh groundwater discharge to an estuary. *Geophysical Research Letters* **38**: no. 11: L11402.
- Gardner, A.T., H.N. Karam, A.E. Mulligan, C.F. Harvey, T.R. Hammar, and H.F. Hemond. (2009). A Differential Pressure Instrument with Wireless Telemetry for In-Situ Measurement of Fluid Flow across Sediment-Water Boundaries. *Sensors* **9**, no. 1: 404–29.
- Garnier, J., A. Beusen, V. Thieu, G. Billen, and L. Bouwman (2010), N:P: Si nutrient export ratios and ecological consequences in coastal seas evaluated by the ICEP approach, *Global Biogeochem. Cycles*, *24*: doi:10.1029/2009GB003583
- Gattuso JP, Frankignoulle M, Wollast R. (1998). Carbon and carbonate metabolism in coastal aquatic ecosystems. *Annu. Rev. Ecol. Syst.* *29*:405–34

- Glud, R. N. (2008). Oxygen dynamics of marine sediments. *Marine Biology Research*, 4(4), 243–289. <https://doi.org/10.1080/17451000801888726>
- Gomez-Velez, J.D., Harvey, J.W., Cardenas, M.B. and Kiel, B. (2015). Denitrification in the Mississippi river network controlled by flow through river bedforms, *Nature Geoscience*, 8. <http://doi.org/10.1038/ngeo2567>
- Gonneea, M. E., Morris, P. J., Dulaiova, H., & Charette, M. A. (2008). New perspectives on radium behavior within a subterranean estuary. *Marine Chemistry*, 109(3–4), 250–267. <https://doi.org/10.1016/j.marchem.2007.12.002>
- Gu, C, Anderson W, Maggi F (2012) Riparian biogeochemical hot moments induced by stream fluctuations. *Water Resources Research* 48, doi:10.1029/2011WR011720.
- Hall SJ. (2002). The continental shelf benthic ecosystem: current status, agents for change and future prospects. *Environ. Conserv.* 29:350–74
- Harbaugh, A. W., Banta, E. R., Hill, M. C., & McDonald, M. G. (2000). *MODFLOW-2000, the U.S. Geological Survey Modular Ground-Water Model-User Guide to Modularization Concepts and the Ground-Water Flow Process: Open File Report 00-92*. Reston, VA: US Geological Survey
- 1 sport  
process in marine sediments. *Journal of Geophysical Research*, 88(C12), 7617–7622. <https://doi.org/10.1029/JC088iC12p07617>
- Harvey, J. W., Boehlke, J. K., Voytek, M. A., Scott, D., & Tobias, C. R. (2013). Hyporheic zone denitrification: Controls on effective reaction depth and contribution to whole-stream mass balance. *Water Resources Research*, 49(10), 6298–6316. <https://doi.org/10.1002/wrcr.20492>
- Harvey, J.W., Böhlke, J.K., Voytek, M.A. Scott, D. & Tobias, C.R. (2013). Hyporheic zone denitrification: Controls on effective reaction depth and contribution to whole-stream mass balance. *Water Resources Research*, 49. <http://doi.org/10.1002/wrcr.20492>
- Heiss, J. W., Post, V. E. A., Laattoe, T., Russoniello, C. J., & Michael, H. A. (2017). Physical controls on biogeochemical processes in intertidal zones of beach aquifers. *Water Resources Research*, 53. <https://doi.org/10.1002/2017WR021110>
- Hemer, M. A., Fan, Y., Mori, N., Semedo, A., & Wang, X. L. (2013). Projected changes in wave climate from a multi-model ensemble. *Nature Climate Change*, 3(5), 471–476. <https://doi.org/10.1038/nclimate1791>

- Hemer, M. A., Katzfey, J., & Hotan, C. (2011). The wind-wave climate of the Pacific Ocean. *Report for the Pacific Adaptation Strategy Assistance Program Department of Climate Change and Energy Efficiency*, (September), 120 pp.
- Henderson, R.D., F.D. Day-Lewis, and C.F. Harvey. (2009). Investigation of aquifer-estuary interaction using wavelet analysis of fiber-optic temperature data. *Geophysical Research Letters* **36**: L06403.
- Herbers, T. H. C., Elgar, S., & Guza, R. T. (1999). Directional spreading of waves in the nearshore zone. *Journal of Geophysical Research*, *104*(C4), 7683–7693. <https://doi.org/10.1029/1998JC900092>
- Huettel, M, Roy, H, Precht, E, Ehrenhauss, S, (2003) Hydrodynamical impact on biogeochemical processes in aquatic sediments. *Hydrobiologia* 494, 231-236.
- Huettel, M, Webster, I (2001) Pore water flow in permeable sediments. In: Boudreau, B., Jorgensen, B. (Eds.), *The Benthic Boundary Layer Transport Processes and Biogeochemistry*. Oxford University Press, New York:144-179.
- Huettel, M. H., Iebis, W. Z., Orster, S. F., & Luther, G. W. (1998). Advective transport affecting metal and nutrient distributions and interfacial fluxes in permeable sediments. *Geochimica et Cosmochimica Acta*, *62*(4), 613–631.
- Huettel, M., Berg, P., & Kostka, J. E. (2014). Benthic exchange and biogeochemical cycling in permeable sediments. *Annual Review of Marine Science*, *6*, 23–51. <http://doi.org/10.1146/annurev-marine-051413-012706>
- Huettel, M., Berg, P., & Kostka, J. E. (2014). Benthic exchange and biogeochemical cycling in permeable sediments. *Annual Review of Marine Science*, *6*, 23–51. <https://doi.org/10.1146/annurev-marine-051413-012706>
- IPCC. (2013). *Climate Change 2013: The Physical Science Basis. Contribution of Working Group I to the Fifth Assessment Report of the Intergovernmental Panel on Climate Change* [Stocker, T.F., D. Qin, G.-K. Plattner, M. Tignor, S.K. Allen, J. Boschung, A. Nauels, Y. Xia, V. Bex and P.M. Midgley (eds.)]. Cambridge University Press, Cambridge, United Kingdom and New York, NY, USA, 1535 pp.
- Jahnke RA, Nelson JR, Richards ME, Robertson CY, Rao AMF, Jahnke DB. (2008). Benthic primary productivity on the Georgia midcontinental shelf: benthic flux measurements and high-resolution, continuous in situ PAR records. *J. Geophys. Res.* 113:C08022

- Jahnke, R., & Nelson, J. (2000). Benthic flux of biogenic elements on the Southeastern US continental shelf: influence of pore water advective transport and benthic microalgae. *Cont. Shelf Res.*, *20*, 109–127.
- Janssen F., Huettel M., Witte U., (2005). Pore-water advection and solute fluxes in permeable marine sediments (II): benthic respiration at three sandy sites with different permeabilities (German Bight, North Sea). *Limnol. Oceanogr.* *50*:779–92
- Jeng, D. S., Barry, D. A., & Li, L. (2001). Water wave-driven seepage in marine sediments. *Advances in Water Resources*, *24*(1), 1–10.  
[http://doi.org/10.1016/S0309-1708\(00\)00036-1](http://doi.org/10.1016/S0309-1708(00)00036-1)
- Johannes, R.E. (1980). The ecological significance of submarine discharge of groundwater. *Marine Ecology Progress Series* **3**: 365-373.
- Johnson, A.G., Glenn, C.R., Burnett, W.C., Peterson, R.N., and Lucey, P.G. (2008). Aerial infrared imaging reveals large nutrient-rich groundwater inputs to the ocean. *Geophysical Research Letters* **35**: L15606.
- Johnson, H. P. & Pruis, M. J. (2003). Fluxes of fluid and heat from the oceanic crustal reservoir. *Earth Planet. Sci. Lett.* **216**, 565–574
- Kennedy, C. D., L. C. Murdoch, D. P. Genereux, D. R. Corbett, K. Stone, P. Pham, and H. Mitasova. (2010). Comparison of Darcian flux calculations and seepage meter measurements in a sandy streambed in North Carolina, United States. *Water Resources Research* **46**, no. 9: W09501.
- King, J. N. (2011), Analytical characterization of selective benthic flux components in estuarine and coastal waters, in *Treatise on Estuarine and Coastal Science*, edited by E. Wolanski and D. McLusky, pp. 397–423, Academic Press, Waltham, Mass
- King, J. N. (2012). Synthesis of benthic flux components in the Patos Lagoon coastal zone, Rio Grande do Sul, Brazil. *Water Resources Research*, *48*(12),  
<http://doi.org/10.1029/2011WR011477>
- King, J. N., Mehta, A. J., & Dean, R. G. (2009). Generalized analytical model for benthic water flux forced by surface gravity waves. *Journal of Geophysical Research*, *114*(C4), C04004. <http://doi.org/10.1029/2008JC005116>
- Kipp, L. E., Charette, M. A., Moore, W. S., Henderson, P. B., & Rigor, I. G. (2018). Increased fluxes of shelf-derived materials to the central Arctic Ocean. *Science Advances*, *4*(January), 1–10.

- Knapp, Kenneth R., Scott Applequist, Howard J. Diamond, James P. Kossin, Michael Kruk, and Carl Schreck (2010). NCDC International Best Track Archive for Climate Stewardship (IBTrACS) Project, Version 3. [North Atlantic]. NOAA National Centers for Environmental Information. DOI:10.7289/V5NK3BZP
- Komar, P. D., & Allan, J. C. (2008). Increasing Hurricane-Generated Wave Heights along the U.S. East Coast and Their Climate Controls. *Journal of Coastal Research*, 242(2), 479–488. <https://doi.org/10.2112/07-0894.1>
- Konikow, LF, Akhavan, M, Langevin, CD, Michael, HA, and Sawyer, AH (2013) Seawater circulation in sediments driven by interactions between seabed topography and fluid density. *Water Resources Research*, 49, 1386–1399. doi:10.1002/wrcr.20121
- Kroeger, KD, Charette, MA (2008) Nitrogen biogeochemistry of submarine groundwater discharge. *Limnology and Oceanography*, 53(3), 1025–1039. doi:10.4319/lo.2008.53.3.1025
- Laruelle, G. G., Cai, W.-J., Hu, X., Gruber, N., Mackenzie, F. T., & Regnier, P. (2018). Continental shelves as a variable but increasing global sink for atmospheric carbon dioxide. *Nature Communications*, 9(1), 454. <https://doi.org/10.1038/s41467-017-02738-z>
- Latham, W., & Lewis, K. (2012). *The Contribution of the Coastal Economy to the State of Delaware*. Delaware Sea Grant. Newark, DE
- Lee, R. D. (1977). A Device for Measuring Seepage Flux in Lakes and Estuaries. *Limnology and Oceanography* 22: no. 1: 140–147.
- Libelo, E. L., and W. G. MacIntyre. (1994). Effects of surface-water movement on seepage-meter measurements of flow through the sediment-water interface. *Hydrogeology Journal* 2, no. 4: 49–54.
- Martin, J. B., J. E. Cable, C. Smith, M. Roy, and J. Cherrier. (2007). Magnitudes of submarine groundwater discharge from marine and terrestrial sources: Indian River Lagoon, Florida, *Water Resources Research* 43, no. 5: W05440.
- Marzadri, A., Tonina, D., & Bellin, A. (2012), Morphodynamic controls on redox conditions and on nitrogen dynamics within the hyporheic zone: Application to gravel bed rivers with alternate-bar morphology, *J. Geophys. Res.*, 117(G3), G00N10, doi:10.1029/2012JG001966

- Mayorga, E., S.P. Seitzinger, J.A. Harrison, E. Dumont, A.H.W. Beusen, A.F. Bouwman, B.M. Fekete, C. Kroeze and G. Van Drecht. (2010). Global Nutrient Export from WaterSheds 2 (NEWS 2): Model development and implementation. *Environmental Modelling & Software* 25: 837-853, doi:10.1016/j.envsoft.2010.01.007
- McClain M, Boyer E, Dent C (2003) Biogeochemical hot spots and hot moments at the interface of terrestrial and aquatic ecosystems. *Ecosystems* 6(4):301-312
- Merritt, M. L. (2004). *Estimating Hydraulic Properties of the Floridan Aquifer System by Analysis of Effects. Collier and Hendry Counties, Florida*. USGS Water-Resources Investigations Report 03-4267. Tallahassee, FL
- Michael, H. A., Charette, M. A., & Harvey, C. F. (2011). Patterns and variability of groundwater flow and radium activity at the coast: A case study from Waquoit Bay, Massachusetts. *Marine Chemistry*, 127(1-4), 100-114. <http://doi.org/10.1016/j.marchem.2011.08.001>
- Michael, H. A., Lubetsky, J., & Harvey, C. (2003). Characterizing submarine groundwater discharge: A seepage meter study in Waquoit Bay, Massachusetts. *Geophysical Research Letters*, 30(6). <http://doi.org/10.1029/2002GL016000>
- Michael, H.A., A.E. Mulligan, and C.F. Harvey. (2005). Seasonal oscillations in water exchange between aquifers and the coastal ocean. *Nature* **436**, no. 7054: 1145-8.
- MMAB; NOAA; National Weather Service; National Centers for Environmental Prediction; Environmental Modeling Center; Marine Modeling and Analysis Branch. (2017). WAVEWATCH III Hindcast and Reanalysis Archives: Phase II. <http://polar.ncep.noaa.gov/waves/hindcasts/nopp-phase2.php>
- Moore, W. S., & Wilson, A. M. (2005). Advective flow through the upper continental shelf driven by storms, buoyancy, and submarine groundwater discharge. *Earth and Planetary Science Letters*, 235(3-4), 564-576. <https://doi.org/10.1016/j.epsl.2005.04.043>
- Moore, W.S. (2010). The effect of submarine groundwater discharge on the ocean. *Annual Review of Marine Science* **2**: 59-88.
- Moosdorf, N., & Oehler, T. (2017). Societal use of fresh submarine groundwater discharge: An overlooked water resource. *Earth-Science Reviews*, 171(June), 338-348. <https://doi.org/10.1016/j.earscirev.2017.06.006>

- Mu, Y., Cheng, A. H.-D., Badiey, M., & Bennett, R. (1999). Water wave driven seepage in sediment and parameter inversion based on pore pressure data. *International Journal for Numerical and Analytical Methods in Geomechanics*, 23(13), 1655–1674. [https://doi.org/10.1002/\(SICI\)1096-9853\(199911\)23:13<1655::AID-NAG61>3.0.CO;2-D](https://doi.org/10.1002/(SICI)1096-9853(199911)23:13<1655::AID-NAG61>3.0.CO;2-D)
- Mulligan, A.E., and M.A. Charette. (2006). Intercomparison of submarine groundwater discharge estimates from a sandy unconfined aquifer. *Journal of Hydrology* 327, no. 3-4: 411-425.
- Murdoch, L. C., and S. E. Kelly. (2003). Factors affecting the performance of conventional seepage meters. *Water Resources Research* 39, no. 6: 1163-1172.
- National Climatic Data Center (NCDC) (2016). Quality controlled local climatological data ASCII Files. <https://www.ncdc.noaa.gov/orders/qclcd/> accessed 9/20/2016
- Naval Oceanographic Office (NAVO). (2010). Database for Bottom Sediment Type: Oceanographic and Atmospheric Master Library. Naval Oceanographic Office: Acoustics Division: Stennis Space Center, Mississippi. Accessed through Effect of Sound on the Marine Environment FOIA Request: <https://esme.bu.edu/index.shtml>
- Nelson, J.R., Eckman, J.E., Robertson, C.Y., Marinelli, R.L., & Jahnke, R.A. (1999). Benthic microalgal biomass and irradiance at the sea floor on the continental shelf of the South Atlantic Bight: spatial and temporal variability and storm effects. *Cont. Shelf Res.* 19(4):477–505. [https://doi.org/10.1016/S0278-4343\(98\)00092-2](https://doi.org/10.1016/S0278-4343(98)00092-2)
- Nortek-AS. (2015). Aquadopp HR-Profiler Factsheet. Nortek AS. Oslo, Norway
- Orzech, M. D., and N. Kobayashi. (1997). Random wave transformation and sediment transport across barred and terraced sand beaches: research report No. CACR-97-06, Newark, DE.
- Perez, J., Menendez, M., Camus, P., Mendez, F. J., & Losada, I. J. (2015). Statistical multi-model climate projections of surface ocean waves in Europe. *Ocean Modelling*, 96, 161–170. <https://doi.org/10.1016/j.ocemod.2015.06.001>
- Precht, E., & Huettel, M. (2003). Advective pore-water exchange driven by surface gravity waves and its ecological implications. *Limnology and Oceanography*, 48(4), 1674–1684.

- Precht, E., & Huettel, M. (2004). Rapid wave-driven advective pore water exchange in a permeable coastal sediment. *Journal of Sea Research*, 51(2), 93–107. <https://doi.org/10.1016/j.seares.2003.07.003>
- Rao, A. M. F., & Charette, M. A. (2012). Benthic Nitrogen Fixation in an Eutrophic Estuary Affected by Groundwater Discharge. *Journal of Coastal Research*, 280, 477–485. <https://doi.org/10.2112/JCOASTRES-D-11-00057.1>
- Reid, R. O., & Kajiura, K. (1957). On the damping of gravity waves over a permeable sea bed. *Transactions of the American Geophysical Union*, 38(5), 662–6. <http://doi.org/10.1029/TR038i005p00662>
- Riedl, R. J., Huang, N., & Machan, R. (1972). The subtidal pump: a mechanism of interstitial water exchange by wave action. *Marine Biology*, 13(3), 210–221. <http://doi.org/10.1007/BF00391379>
- Robinson, C., Li, L., & Barry, D. A. (2007). Effect of tidal forcing on a subterranean estuary. *Advances in Water Resources*, 30(4), 851–865. <https://doi.org/10.1016/j.advwatres.2006.07.006>
- Rosenberry, D. O. (2005). Integrating seepage heterogeneity with the use of ganged seepage meters. *Limnology and Oceanography: Methods*, 3, no. Feb: 131 - 142.
- Rosenberry, D. O. (2008). A seepage meter designed for use in flowing water. *Journal of Hydrology*, 359(1–2), 118–130. <http://doi.org/10.1016/j.jhydrol.2008.06.029>
- Rosenberry, D. O., & Morin, R. H. (2004). Use of an electromagnetic seepage meter to investigate temporal variability in lake seepage. *Ground Water*, 42. <http://doi.org/10.1111/j.1745-6584.2004.tb02451.x>
- Rosenberry, D. O., and M. A. Menheer. (2006). A System for Calibrating Seepage Meters Used to Measure Flow Between Ground Water and Surface Water. U.S. Geological Survey Scientific Investigations Report 2006-5053.
- Rosenberry, D. O., J. W. Labaugh, and R. J. Hunt. (2008). Use of Monitoring Wells, Portable Piezometers, and Seepage Meters to Quantify Flow Between Surface Water and Ground Water. in Rosenberry, D.O. and J. W. LaBaugh. eds. Field Techniques for Estimating Water Fluxes Between Surface Water and Ground Water: U.S. Geological Survey Techniques and Methods 4-D2.
- Rosenberry, D. O., P. Z. Klos, and A. Neal. (2012). In situ quantification of spatial and temporal variability of hyporheic exchange in static and mobile gravel-bed rivers. *Hydrological Processes* 26, no. 4: 604–612.

Rosenberry, D. O., R. W. Sheibley, S. E. Cox, F. W. Simonds, and D. L. Naftz. (2013). Temporal variability of exchange between groundwater and surface water based on high-frequency direct measurements of seepage at the sediment-water interface. *Water Resources Research* **49**, no. 5: 2975–2986.

200

cond *Hydrological Processes* **23**, 23:  
3306-3318.

Roy, M., Martin, J. B., Cable, J. E., & Smith, C. G. (2012). Variations of iron flux and organic carbon remineralization in a subterranean estuary caused by inter-annual variations in recharge. *Geochimica et Cosmochimica Acta*, *103*(null), 301–315. <https://doi.org/10.1016/j.gca.2012.10.055>

Russoniello, C. J., & Michael, H. A. (2014). Investigation of Seepage Meter Measurements in Steady Flow and Wave Conditions. *Groundwater*, *53*(6), 959-66. <http://doi.org/10.1111/gwat.12302>

Russoniello, C. J., & Michael, H. A. (2015). Investigation of Seepage Meter Measurements in Steady Flow and Wave Conditions. *Groundwater*, *53*(6), 959–966. <https://doi.org/10.1111/gwat.12302>

Russoniello, C. J., Fernandez, C., Bratton, J. F., Banaszak, J. F., Krantz, D. E., Andres, A. S., Konikow, L.F., & Michael, H. A. (2013). Geologic effects on groundwater salinity and discharge into an estuary. *Journal of Hydrology*, *498*, 1–12. <https://doi.org/10.1016/j.jhydrol.2013.05.049>

Russoniello, C. J., Heiss, J. W., & Michael, H. A. (2018). Variability in Benthic Exchange Rate, Depth, and Residence Time Beneath A Shallow Coastal Estuary. *Journal of Geophysical Research: Oceans*, *123*, 1–17. <https://doi.org/10.1002/2017JC013568>

Russoniello, C. J., Konikow, L. F., Kroeger, K. D., Fernandez, C., Scott Andres, A., & Michael, H. A. (2016). Hydrogeologic controls on groundwater discharge and nitrogen loads in a coastal watershed. *Journal of Hydrology*, *538*, 783–793. <https://doi.org/10.1016/j.jhydrol.2016.05.013>

Russoniello, C., Heiss, J.W., & Michael, H.A. (2017). Variability in benthic exchange rate, depth, and residence time beneath a shallow coastal estuary, HydroShare, <http://www.hydroshare.org/resource/d1c980ba6dd7411db6931b8758f3abe2>

Russoniello, C.J. (2012). Exploring submarine groundwater discharge into the Delaware Inland Bays over diverse scales with direct measurements and modeling. M.S. Thesis. University of Delaware.

- Santoro, A. E., Francis, C. A., De Siewes, N. R., & Boehm, A. B. (2008). Shifts in the relative abundance of ammonia-oxidizing bacteria and archaea across physicochemical gradients in a subterranean estuary. *Environmental Microbiology*, *10*(4), 1068–1079. <https://doi.org/10.1111/j.1462-2920.2007.01547.x>
- Santos, I. R., Eyre, B. D., & Huettel, M. (2012). The driving forces of porewater and groundwater flow in permeable coastal sediments: A review. *Estuarine, Coastal and Shelf Science*, *98*, 1–15. <http://doi.org/10.1016/j.ecss.2011.10.024>
- Santos, I. R., W. C. Burnett, J. P. Chanton, N. Dimova, and R. N. Peterson. (2009). Land or ocean?: Assessing the driving forces of submarine groundwater discharge at a coastal site in the Gulf of Mexico. *Journal of Geophysical Research* **114**, no. C4: C04012.
- Sawyer, A. H. (2015). Enhanced removal of groundwater-borne nitrate in heterogeneous aquatic sediments. *Geophysical Research Letters*, *42*, 403–410. <http://doi.org/10.1002/2014GL062234>.
- Sawyer, A. H., & Cardenas, M. B. (2009). Hyporheic flow and residence time distributions in heterogeneous cross-bedded sediment. *Water Resources Research*, *45*(8), n/a-n/a. <https://doi.org/10.1029/2008WR007632>
- Sawyer, A. H., Cardenas, M. B., & Buttle, J. (2011). Hyporheic exchange due to channel-spanning logs. *Water Resources Research*, *47*, 12. <https://doi.org/10.1029/2011WR010484>
- Sawyer, A. H., Lazareva, O., Kroeger, K. D., Crespo, K., Chan, C. S., Stieglitz, T., & Michael, H. A. (2014). Stratigraphic controls on fluid and solute fluxes across the sediment-water interface of an estuary. *Limnology and Oceanography*, *59*(3), 997–1010. <http://doi.org/10.4319/lo.2014.59.3.0997>
- Sawyer, A. H., Shi, F., Kirby, J. T., & Michael, H. A. (2013). Dynamic response of surface water-groundwater exchange to currents, tides, and waves in a shallow estuary. *Journal of Geophysical Research: Oceans*, *118*(4), 1749–1758. <http://doi.org/10.1002/jgrc.20154>
- Seitzinger, S. P., Harrison, J. A., Böhlke, J. K., Bouwman, A. F., Lowrance, R., Peterson, B., Tobias, C., & Van Drecht, G. (2006). Denitrification across landscapes and waterscapes: a synthesis. *Ecological Applications* *16*(6), 2064–2090. [http://doi.org/10.1890/1051-0761\(2006\)016\[2064:DALAWA\]2.0.CO;2](http://doi.org/10.1890/1051-0761(2006)016[2064:DALAWA]2.0.CO;2)

- Seitzinger, S.P., E. Mayorga, A.F. ouwman, C. Kroeze, A.H.W. Beusen, G. Billen, G. Van Drecht, E. Dumont, B.M. Fekete, J. Garnier and J.A. Harrison. (2010). Global river nutrient export: A scenario analysis of past and future trends. *Global Biogeochemical Cycles* 24:GB0A08, doi:10.1029/2009GB003587
- Shaw, R., and E. Prepas. (1989). Anomalous, short-term influx of water into seepage meters. *Limnology and Oceanography* **34**, no. 7: 1343-1351.
- Shinn, E. A., C. D. Reich, and T. D. Hickey. 2002. Seepage Meters and Bernoulli's Revenge. *Estuaries* **25**, no. 1: 126–132.
- 1 2  
sediment interface. *Journal of Geophysical Research: Oceans*, 97(C1), 789–808. <https://doi.org/10.1029/91jc02101>
- Shum, K. T. (1993). The Effects of Wave-Induced Pore-Water Circulation on the Transport of Reactive Solutes Below a Rippled Sediment Bed. *Journal of Geophysical Research-Oceans*, 98(C6), 10289–10301. <http://doi.org/10.1029/93jc00787>
- Shum, K. T., & Sundby, B. (1996). Organic matter processing in continental shelf sediments—the subtidal pump revisited. *Marine Chemistry*, 53(1–2), 81–87. [http://doi.org/10.1016/0304-4203\(96\)00014-X](http://doi.org/10.1016/0304-4203(96)00014-X)
- Slomp, C.P., and P. Van Capellen. (2004). Nutrient inputs to the coastal ocean through submarine groundwater discharge: controls and potential impact. *Journal of Hydrology* **295**: 64-86.
- Smith, A. J., Herne, D. E., & Turner, J. V. (2009). Wave effects on submarine groundwater seepage measurement. *Advances in Water Resources*, 32(6), 820–833. <http://doi.org/10.1016/j.advwatres.2009.02.003>
- Spiteri, C, Slomp, CP, Charette, MA, Tuncay, K, and Meile, C (2008) Flow and nutrient dynamics in a subterranean estuary (Waquoit Bay, MA, USA): field data and reactive transport modeling. *Geochimica et Cosmochimica Acta*, 72(14), 3398–3412. doi:10.1016/j.gca.2008.04.027
- Stieglitz, T., M. Taniguchi, and S. Neylon. (2008). Spatial variability of submarine groundwater discharge, Ubatuba, Brazil, Estuarine. *Coastal and Shelf Science* **76**, no. 3: 493–500.
- Taniguchi, M., W. Burnett, J. E. Cable, and J. V. Turner. (2002). Investigation of submarine groundwater discharge. *Hydrological Processes* **16**, no. 11: 2115-2129.

- Thibodeaux, L. J., & Boyle, J. D. (1987). Bedform-generated convective transport in bottom sediment. *Nature*, 325, 341–343. <http://doi.org/10.1038/325341a0>
- Tobias CR, Anderson IC, Canuel EA, Macko SA (2001) Nitrogen cycling through a fringing marsh-aquifer ecotone. *Mar Ecol Prog Ser* 210:25–39
- Tolman, H. L. (2009). *User manual and system documentation of WAVEWATCH-III version 3.14*. Environmental Modeling Center Technical note. NOAA NWS National Centers for Environmental Prediction. Camp Springs, MD.
- Ullman, W. J., Andres, A. S., Scudlark, J. R., & Savidge, K. B. (2002). *Storm-Water and Base-Flow Sampling and Analysis In the Delaware Inland Bays Preliminary Report of Findings 1998-2000: Open File Report 44*. Newark, DE: Delaware Geological Survey.
- Validyne. (2014). *P24 Datasheet*. Validyne Engineering, Northridge, CA.
- Vitousek P, Aber J (1997) Human alteration of the global nitrogen cycle: sources and consequences. *Ecological Applications* 7:737-750
- Walch, M., Seldomridge, E., McGowan, A., Boswell, S., & Bason, C. (2016). *2016 State of the inland bays*. Center for the Inland Bays. Rehoboth Beach, DE.
- Wang, H. F. (2000), *Theory of Linear Poroelasticity with Applications to Geomechanics and Hydrogeology*, 287 pp., Princeton University Press, Princeton, NJ.
- Wang, K., & Davis, E. E. (1996). Theory for the propagation of tidally induced pore pressure variations in layered subseafloor formations. *Journal of Geophysical Research*, 101(B5), 11483. <https://doi.org/10.1029/96JB00641>
- WAVEWATCH III Development Group (WW3DG), 2016: User manual and system documentation of WAVEWATCH III version 5.16. Tech. Note 329, NOAA/NWS/NCEP/MMAB, College Park, MD, USA, 326 pp. + Appendices.
- Webb, J. E., & Theodor, J. (1968). Irrigation of Submerged Marine Sands through Wave Action. *Nature*, 220(5168), 682–683. <https://doi.org/10.1038/220682a0>
- Webb, J. E., and J. Theodor. (1968). Irrigation of Submerged Marine Sands through Wave Action. *Nature* **220**, no. 5168: 682–683.
- White, F. M. (2003). *Fluid Mechanics*, 5th ed., Hill, McGraw.

- Wilson, A. M., Woodward, G. L., & Savidge, W. B. (2016). Using heat as a tracer to estimate the depth of rapid porewater advection below the sediment-water interface. *Journal of Hydrology*, 538, 743–753. <http://doi.org/10.1016/j.jhydrol.2016.04.047>
- Wilson, A. M., Woodward, G. L., & Savidge, W. B. (2016). Using heat as a tracer to estimate the depth of rapid porewater advection below the sediment-water interface. *Journal of Hydrology*. <https://doi.org/10.1016/j.jhydrol.2016.04.047>
- Woessner, W. W., and K. E. Sullivan. (1984). Results of seepage meter and mini-piezometer study, Lake Mead, Nevada. *Ground Water* **22** no. 5: 561–568.
- Yamamoto, T., Koning, H. L., Sellmeijer, H., & Van Hijum, E. (1978). On the response of a poro-elastic bed to water waves. *Journal of Fluid Mechanics*, 87, 193–206. <https://doi.org/10.1017/S0022112078003006>
- Young, I. R., & Verhagen, L. A. (1996). The growth of fetch limited waves in water of finite depth. Part 1. Total energy and peak frequency. *Coastal Engineering*, 29(1–2), 47–78. [http://doi.org/10.1016/S0378-3839\(96\)00006-3](http://doi.org/10.1016/S0378-3839(96)00006-3)
- Younger, P. L. (1993). Simple generalized methods for estimating aquifer storage parameters. *Quarterly Journal of Engineering Geology and Hydrogeology*, 26(2), 127–135. <http://doi.org/10.1144/GSL.QJEG.1993.026.02.04>
- Zarnetske, J., & Haggerty, R. (2011). Dynamics of nitrate production and removal as a function of residence time in the hyporheic zone. *Journal of Geophysical Research*, G01025. <https://doi.org/doi:10.1029/2010JG001356>
- Zarnetske, J., & Haggerty, R. (2011). Dynamics of nitrate production and removal as a function of residence time in the hyporheic zone. *Journal of Geophysical Research*, G01025. <https://doi.org/doi:10.1029/2010JG001356>
- Zekster, I. S. (2000). *Groundwater and the Environment - Applications for the global community*. Boca Raton: Lewis Publishers.
- Ziebis, W., Huettel, M., & Forster, S. (1996). Impact of biogenic sediment topography on oxygen fluxes in permeable seabeds. *Marine Ecology Progress Series*, 140, 227–237. <http://doi.org/10.3354/meps240227>

## Appendix A

### SUPPLEMENTAL INFORMATION FOR CHAPTER 2

#### A.1 One-Way Valve Characterization

Bel-Art Scienceware 0.95 cm I.D. 1-way valves were chosen for their low sealing and reopening pressures compared to similar inexpensive valves. Flux reduction due to resistance in the valves was tested in the laboratory. A source of water with a constant head was applied to one end of a seepage meter outflow tube that had been detached from a seepage meter. Flux was recorded with and without an inline valve for seven head values between 1 and 100 cm. For these gradients, the mean flux through the valve was  $66\% \pm 2\%$  of the flux measured without a valve.

#### A.2 Sediment Characterization

The average ( $\pm$  the standard deviation over three hydraulic gradients) K measured with a 7.62 cm diameter constant-head permeameter was  $1.8 \times 10^{-4} \pm 2.1 \times 10^{-6}$  m/s and  $1.9 \times 10^{-4} \pm 1.0 \times 10^{-6}$  m/s for two sediment samples from the tank, and  $1.8 \times 10^{-4} \pm 5.9 \times 10^{-6}$  m/s and  $2.1 \times 10^{-4} \pm 3.8 \times 10^{-6}$  m/s for two samples from the flume. The effective K for the entire tank, including the plywood diffuser and seepage meters, measured for the 14 head gradients tested in the tank experiments was  $1.4 \times 10^{-4} \pm 3.3 \times 10^{-5}$  m/s, slightly lower than the K of the sand samples.

### A.3 Supplementary Figures for Chapter 2

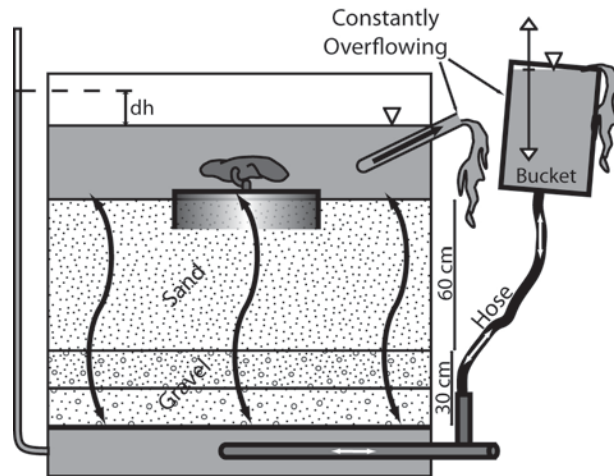


Figure A.1: Cross sectional schematic of wave tank with seepage meter installed. A constant head was maintained in both the tank and bucket through all experiments. In recharge experiments, tap water was allowed to overflow the tank and the bucket was lowered below the tank water level. In discharge experiments, tap water was allowed to overflow the bucket and the bucket was raised above the tank water level. The hydraulic gradient was controlled by changing the bucket elevation and was measured between the tank water surface and water level in a manometer tapped into the tank beneath the diffuser.

## Appendix B

### SUPPLEMENTAL FIGURES FOR CHAPTER 3

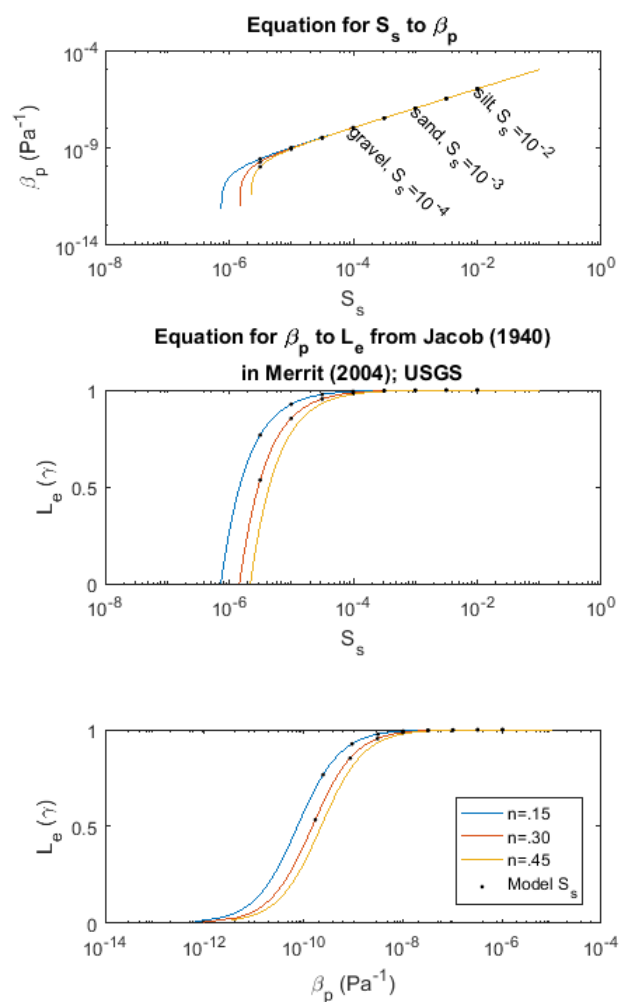


Figure B.1: Relationship between aquifer compressibility ( $\beta_p$ ), loading efficiency ( $L_e$ ), and storage coefficient ( $S_s$ ) for three porosity values ( $n$ ). A value of  $5 \times 10^{-10}$  Pa<sup>-1</sup> was used as in Merrit (2004).

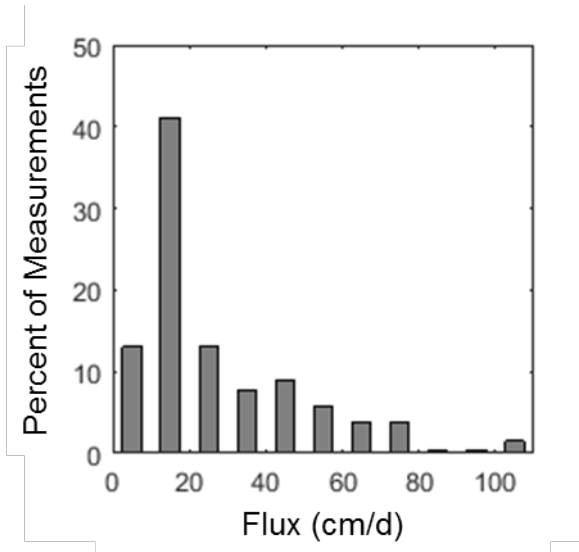


Figure B.2: Histogram of burst-averaged benthic exchange rate frequency from differential pressure sensors.

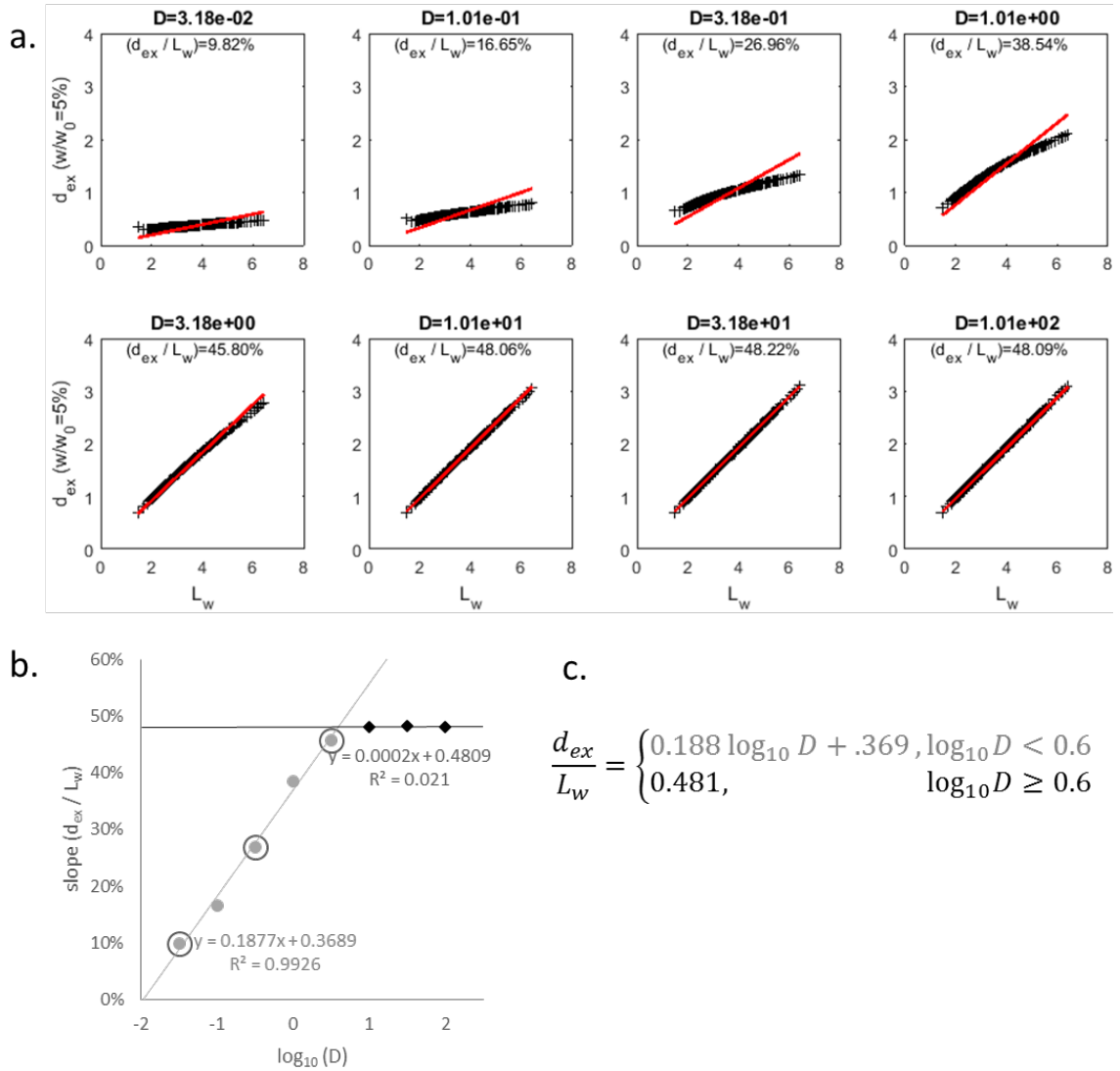


Figure B.3: a.) Scatter plots of mixing zone depth vs.  $L_w$  for 8 sets of MODFLOW models. Exchange zone depth ( $d_{ex}$  was determined as  $\bar{w}/\bar{w}_0=5\%$ ) from individual model runs are shown as black ‘x’s. A linear line of best fit (red) is plotted for the 260 model runs of each model set, and the corresponding slope is displayed as a percentage at the top of each chart. b.) Relationship between  $d_{ex}/L_w$  and  $D$  for the 8 sets of model runs. Black circles indicate high- $D$  model sets in which a mixing zone depth of one-half gravity wavelength is most appropriate. Grey circles indicate model sets where that assumption is less appropriate. Large open circles indicate the three sets of models discussed as low- $D$ , intermediate- $D$ , and high- $D$  in the manuscript. c.) empirical relationship between  $d_{ex}$ ,  $L_w$ , and  $D$ .

**Appendix C**

**SUPPLEMENTAL FIGURES FOR CHAPTER 4**

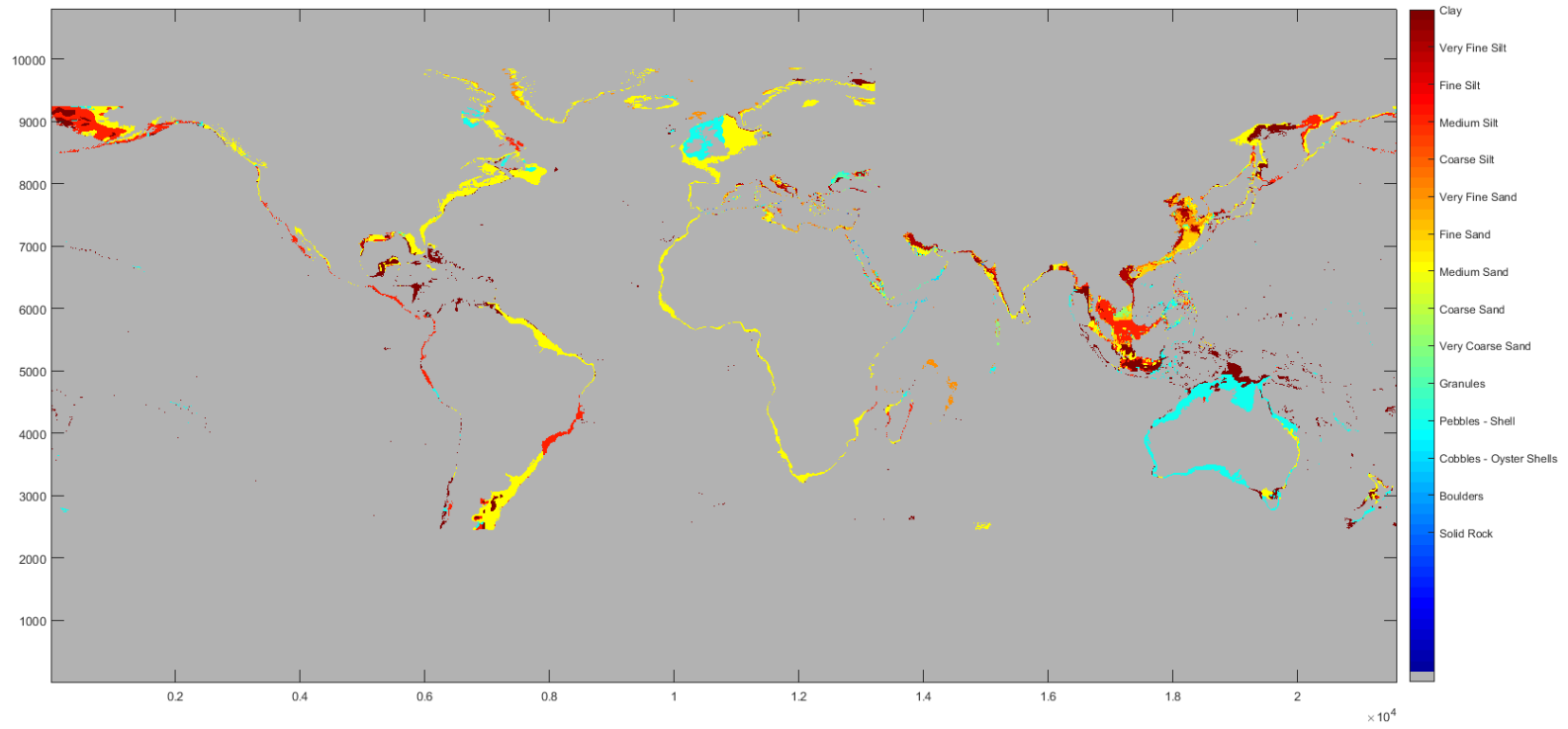


Figure C.1: Sediment type over the global seabed (NAVO, 2010)



Figure C.2: Workflow for computing global wave pumping rates

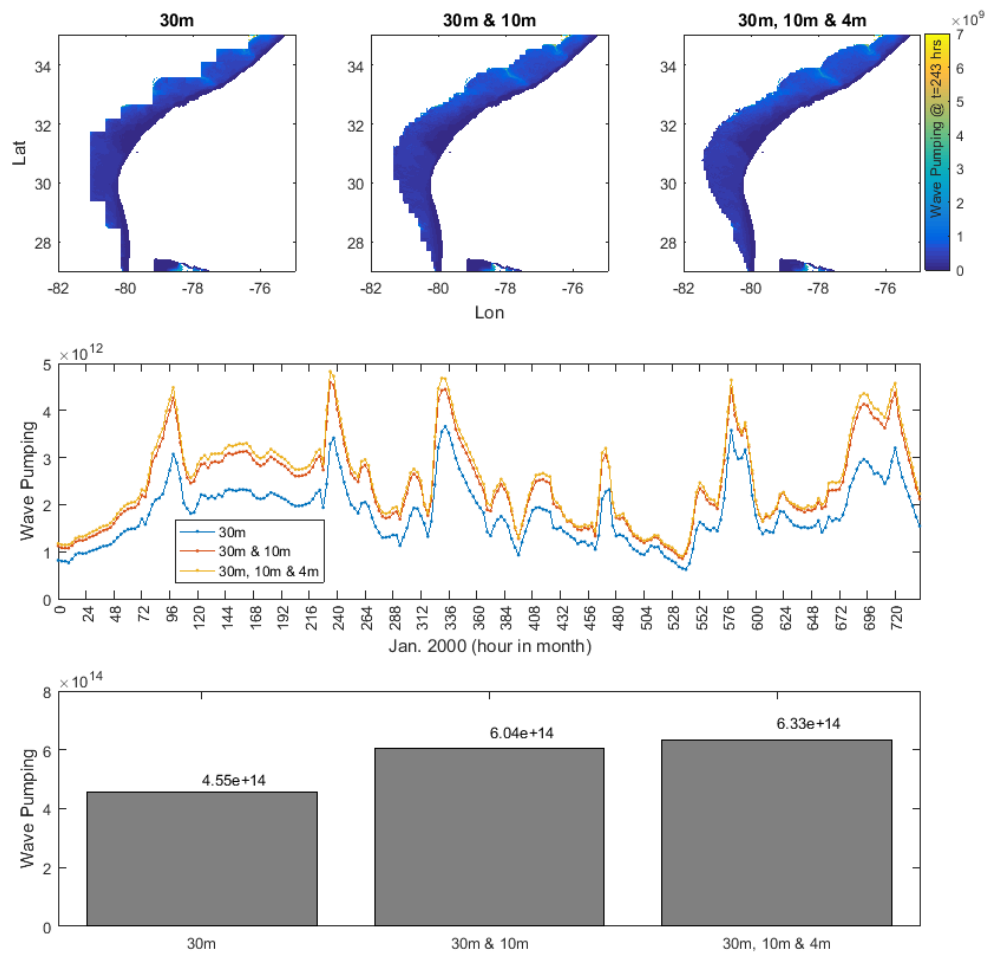


Figure C.3: Sensitivity to resolution of the wave simulation data

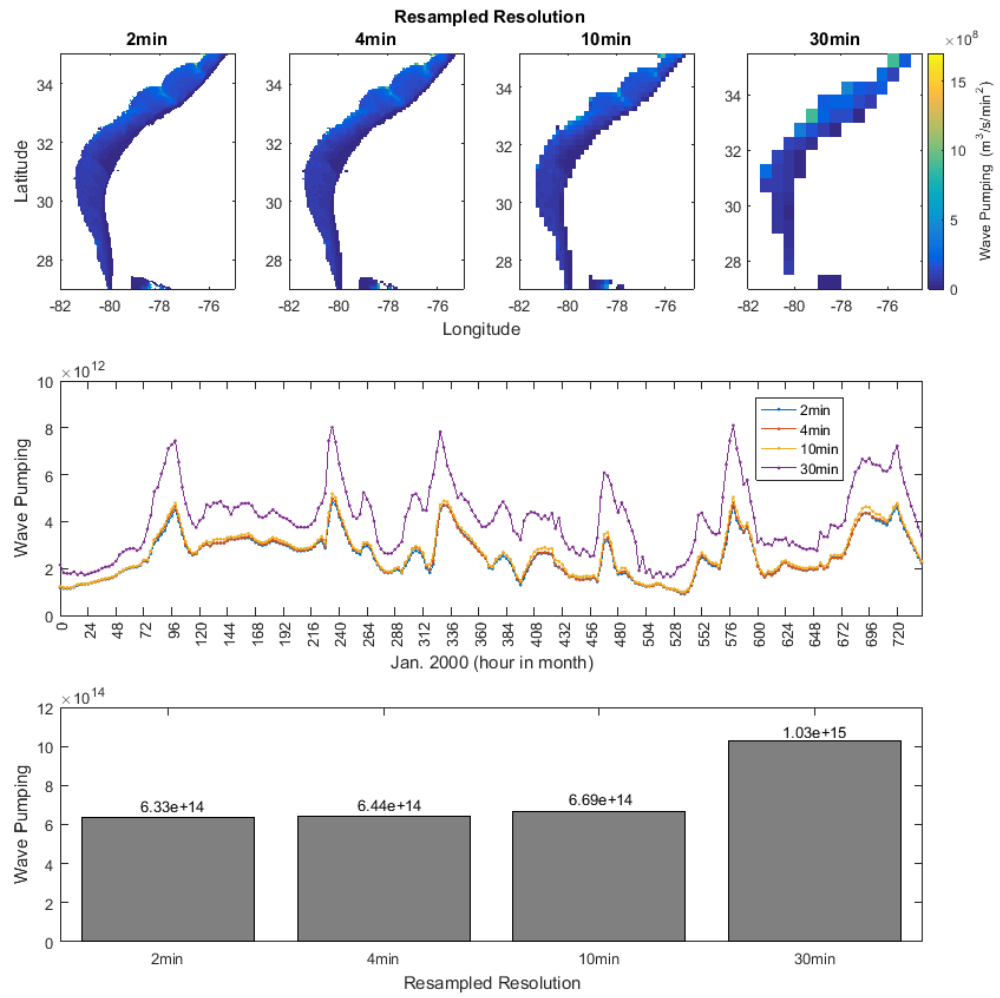


Figure C.4: Sensitivity to simulation resolution (resample resolution)

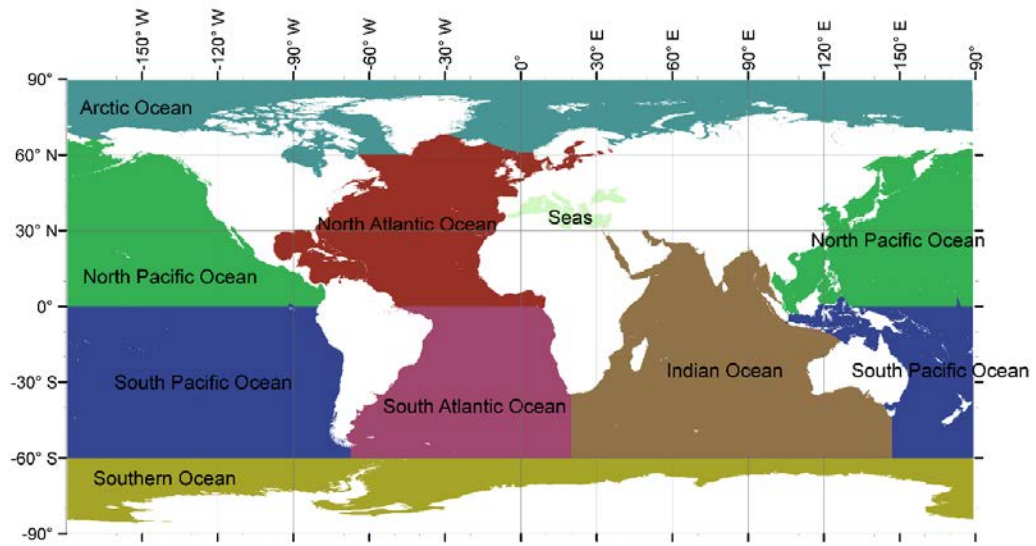


Figure C.5: Basin delineations used in the paper

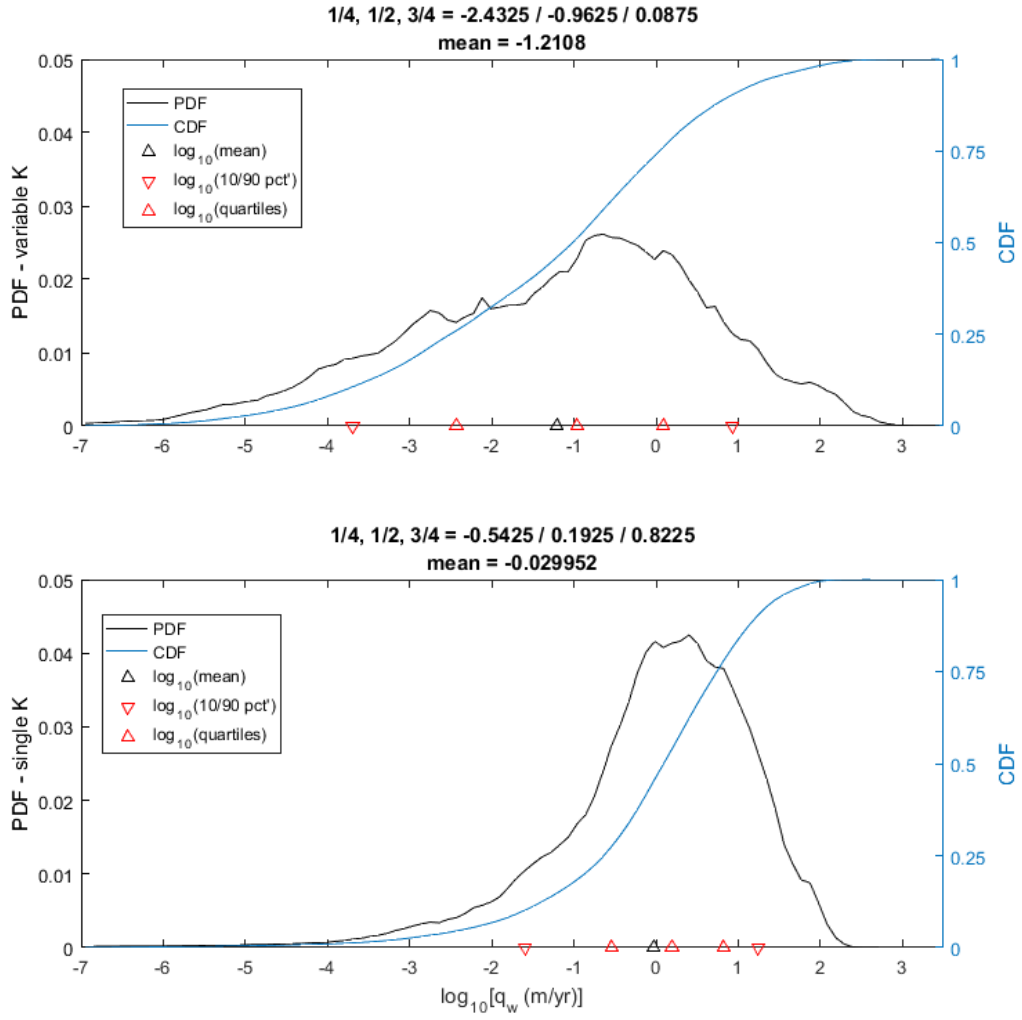


Figure C.6: Flux weighted PDF of flux in the Single-K and Variable-K simulations

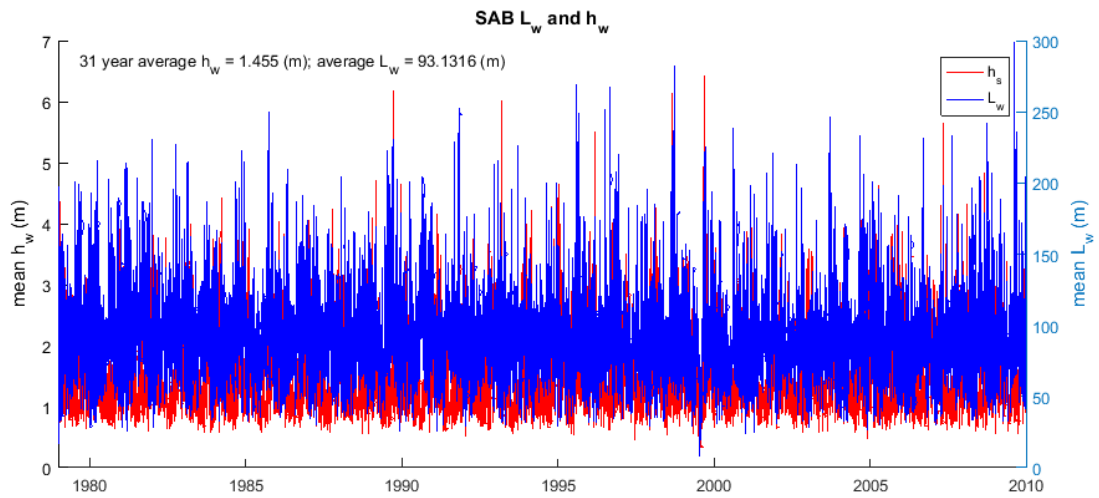
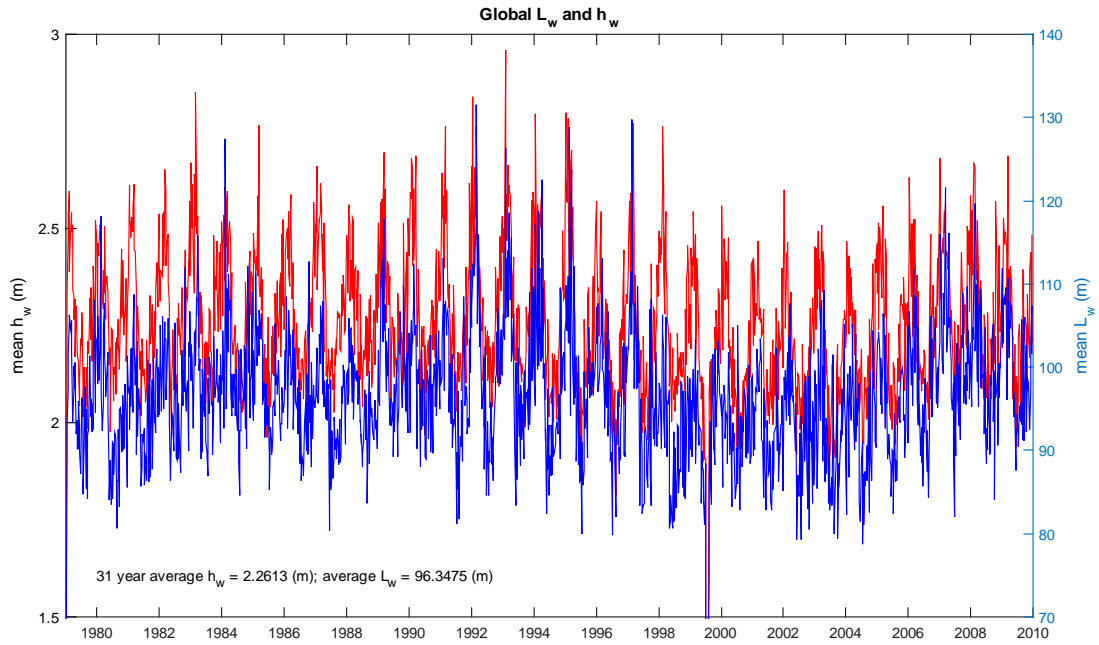


Figure C.7: Mean a.) global and b.) SAB wave parameters for the 31 year scenarios.

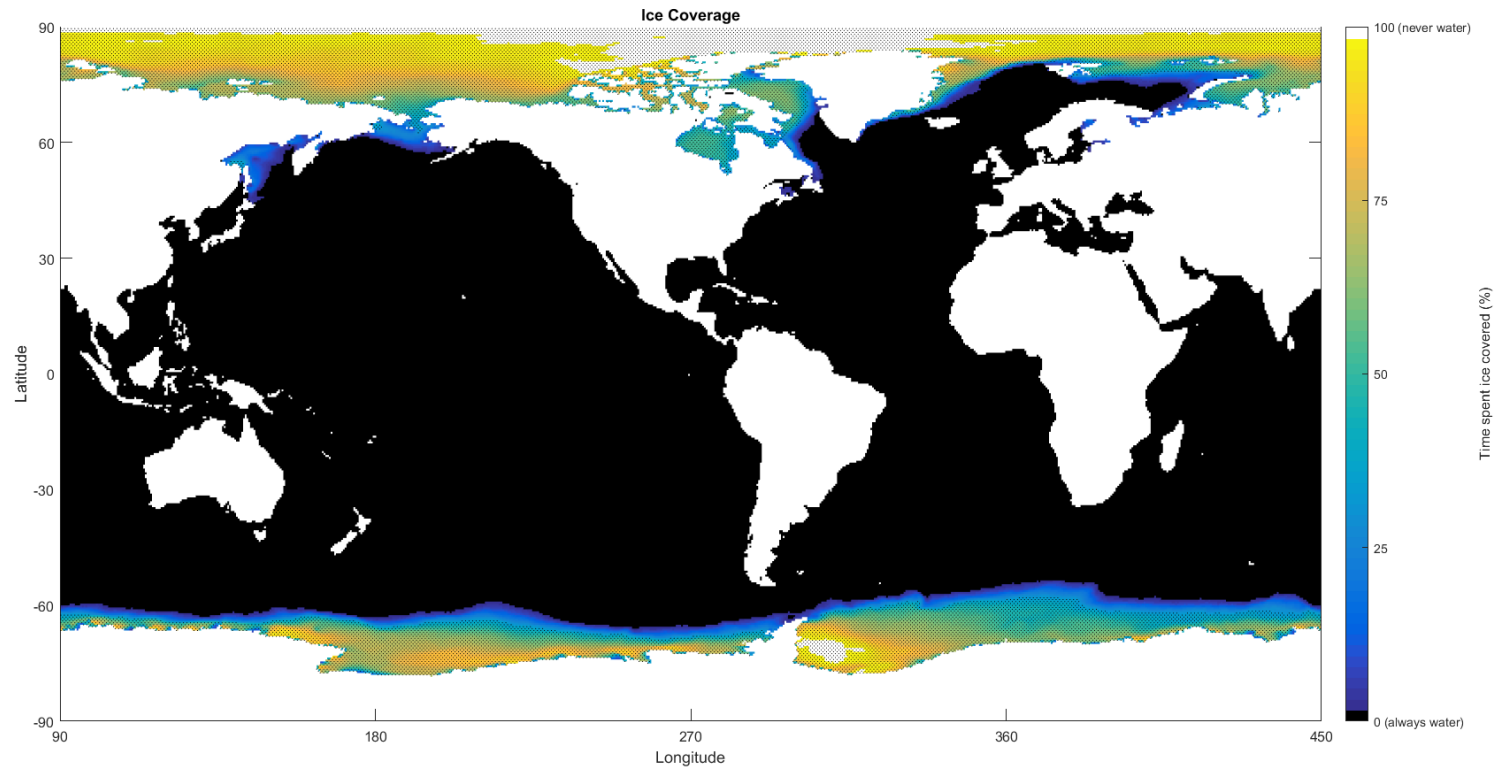


Figure C.8: Ice cover percentage over 31 year simulation

Table C.1 – Wavewatch III Grid information

	<b>ID</b>	<b>Width (cells)</b>	<b>Height (cells)</b>	<b>dx (degrees)</b>	<b>dy (degrees)</b>
<a href="#">Global 30 min</a>	glo_30m	720	336	1/2	1/2
<a href="#">Arctic Ocean 30 min</a>	ao_30m	720	51	1/2	1/2
<a href="#">NW Atlantic 10 min</a>	at_10m	301	331	1/6	1/6
<a href="#">US West Coast 10 min</a>	wc_10m	241	151	1/6	1/6
<a href="#">East Pacific 10 min</a>	ep_10m	511	301	1/6	1/6
<a href="#">Alaskan 10 min</a>	ak_10m	401	187	1.5/6	1/6
<a href="#">Gulf of Mexico and NW Atlantic 4 min</a>	at_4m	586	481	1/15	1/15
<a href="#">US West Coast 4 min</a>	wc_4m	736	526	1/15	1/15
<a href="#">Alaskan 4 min</a>	ak_4m	548	391	2/15	1/15

Table C.2 – Detailed Single-K simulation results

Basin	Total basin area	Average basin depth	Basin volume	Basin shoreline length	Basin shelf area (<200m depth)	Percent of Basin<200m depth	Mean Shelf Depth (m)	Mean $h_w$	Mean $L_w$	Volumetric flux ( $Q_w$ )	Avg. $Q_w$ /basin area	Avg. wave pumping rate ( $q_w$ )	Avg. $Q_w$ /Shoreline length	Basin flushing time
	( $km^2$ )	(m)	( $km^3$ )	(km)	( $km^2$ )		(m)	(m)	(m)	( $km^3$ /yr)	( $km^3$ /yr/ $km^2$ )	(m/yr)	( $km^3$ /km/yr)	(yr)
Global	3.7E+8	3627	1.3E+9	3.6E+5	2.90E+7	7.9%	74.9	0.91	67.82	1.76E+5	4.77E-4	6.06E+0	4.94E-1	7,601
North Atlantic	4.2E+7	3463	1.5E+8	1.1E+5	4.86E+6	11.5%	66.3	1.35	92.62	5.03E+4	1.19E-3	1.04E+1	3.64E-1	2,906
South Atlantic	4.0E+7	3959	1.6E+8		1.88E+6	4.7%	83.4	1.70	115.24	1.60E+4	3.97E-4	8.52E+0		9,981
North Pacific	8.2E+7	4137	3.4E+8	1.4E+5	6.09E+6	7.4%	67.1	1.06	74.53	3.32E+4	4.06E-4	5.46E+0	2.35E-1	10,197
South Pacific	8.8E+7	3767	3.3E+8		3.41E+6	3.9%	54.4	1.01	86.39	2.94E+4	3.34E-4	8.65E+0		11,275
Indian Ocean	6.9E+7	3780	2.6E+8	6.7E+4	3.10E+6	4.5%	56.3	1.27	138.67	2.98E+4	4.29E-4	9.59E+0	4.47E-1	8,808
Arctic Ocean	1.6E+7	1184	1.9E+7	4.5E+4	6.26E+6	39.8%	77.0	0.53	27.55	1.34E+4	8.52E-4	2.14E+0	2.95E-1	1,390
Southern ocean	2.7E+7	2740	7.4E+7	1.8E+4	2.15E+6	8.0%	92.3	0.20	16.57	4.87E+2	1.82E-5	2.26E-1	2.71E-2	150,924
Seas	3.7E+6	1214	4.5E+6	<del>X</del>	1.25E+6	34.0%	53.0	0.70	37.26	3.07E+3	8.34E-4	2.45E+0	<del>X</del>	1,456

Table C.3 – Detailed Variable-K simulation results

Basin	Total basin area	Average basin depth	Basin volume	Basin shoreline length	Basin shelf area (<200m depth)	Percent of Basin<200m depth	Mean Shelf Depth (m)	Log Mean (K)	Mean $h_w$	Mean $L_w$	Volumetric flux (Qw)	Avg. $Q_w$ /basin area	Avg. $Q_w$ /Shelf area ( $q_w$ )	Avg. $Q_w$ /Shoreline length	Basin flushing time
	(km <sup>2</sup> )	(m)	(km <sup>3</sup> )	(km)	(km <sup>2</sup> )		(m)	m/s	(m)	(m)	(km <sup>3</sup> /yr)	(km <sup>3</sup> /yr/km <sup>2</sup> )	(km <sup>3</sup> /yr/km <sup>2</sup> )	(km <sup>3</sup> /km/yr)	(yr)
Global	3.7E+8	3627	1.3E+9	3.6E+5	2.9E+7	7.9%	74.9	1.1E-05	0.91	67.82	1.65E+5	5.70E-3	5.70E-3	4.64E-1	8,083
North Atlantic	4.2E+7	3463	1.5E+8	1.1E+5	4.9E+6	11.5%	66.3	1.2E-05	1.35	92.62	1.69E+4	4.00E-4	3.48E-3	1.16E-1	8,654
South Atlantic	4.0E+7	3959	1.6E+8		1.9E+6	4.7%	83.4	8.6E-06	1.70	115.24	2.94E+3	7.28E-5	1.56E-3		54,402
North Pacific	8.2E+7	4137	3.4E+8	1.4E+5	6.1E+6	7.4%	67.1	1.5E-06	1.06	74.53	2.62E+4	3.20E-4	4.30E-3	2.70E-1	12,948
South Pacific	8.8E+7	3767	3.3E+8		3.4E+6	3.9%	54.4	3.6E-06	1.01	86.39	5.55E+4	6.30E-4	1.63E-2		5,980
Indian Ocean	6.9E+7	3780	2.6E+8	6.7E+4	3.1E+6	4.5%	56.3	1.2E-05	1.27	138.67	5.78E+4	8.33E-4	1.86E-2	8.68E-1	4,538
Arctic Ocean	1.6E+7	1184	1.9E+7	4.5E+4	6.3E+6	39.8%	77.0	2.1E-05	0.53	27.55	3.82E+3	2.43E-4	6.11E-4	8.42E-2	4,867
Southern ocean	2.7E+7	2740	7.4E+7	1.8E+4	2.2E+6	8.0%	92.3	2.1E-05	0.20	16.57	8.20E+1	3.06E-6	3.81E-5	4.56E-3	896,341
Seas	3.7E+6	1214	4.5E+6		1.3E+6	34.0%	53.0	8.9E-06	0.70	37.26	2.03E+3	5.50E-4	1.62E-3		2,207

Results by basin for global variable-K scenario

**Appendix D**  
**Permissions**

**JOHN WILEY AND SONS LICENSE  
TERMS AND CONDITIONS**

Apr 22, 2018

This Agreement between Mr. Christopher Russoniello ("You") and John Wiley and Sons ("John Wiley and Sons") consists of your license details and the terms and conditions provided by John Wiley and Sons and Copyright Clearance Center.

License Number	4334360274199
License date	Apr 22, 2018
Licensed Content Publisher	John Wiley and Sons
Licensed Content Publication	Ground Water
Licensed Content Title	Investigation of Seepage Meter Measurements in Steady Flow and Wave Conditions
Licensed Content Author	Christopher J. Russoniello, Holly A. Michael
Licensed Content Date	Nov 18, 2014
Licensed Content Volume	53
Licensed Content Issue	6
Licensed Content Pages	8
Type of use	Dissertation/Thesis
Requestor type	Author of this Wiley article
Format	Print and electronic
Portion	Full article
Will you be translating?	No
Title of your thesis / dissertation	THE EFFECT OF WAVES ON BENTHIC EXCHANGE: MEASUREMENT AND ESTIMATION OVER A BROAD RANGE OF SPATIAL AND TEMPORAL SCALES
Expected completion date	May 2018
Expected size (number of pages)	150
Requestor Location	Mr. Christopher Russoniello 600 Hibben Magie Dr. Apt 112  PRINCETON, NJ 08540 United States Attn: Mr. Christopher Russoniello
Publisher Tax ID	EU826007151
Total	0.00 USD

[Terms and Conditions](#)

**TERMS AND CONDITIONS**

This copyrighted material is owned by or exclusively licensed to John Wiley & Sons, Inc. or one of its group companies (each a "Wiley Company") or handled on behalf of a society with which a Wiley Company has exclusive publishing rights in relation to a particular work (collectively "WILEY"). By clicking "accept" in connection with completing this licensing transaction, you agree that the following terms and conditions apply to this transaction

(along with the billing and payment terms and conditions established by the Copyright Clearance Center Inc., ("CCC's Billing and Payment terms and conditions"), at the time that you opened your RightsLink account (these are available at any time at <http://myaccount.copyright.com>).

## Terms and Conditions

- The materials you have requested permission to reproduce or reuse (the "Wiley Materials") are protected by copyright.
- You are hereby granted a personal, non-exclusive, non-sub licensable (on a stand-alone basis), non-transferable, worldwide, limited license to reproduce the Wiley Materials for the purpose specified in the licensing process. This license, **and any CONTENT (PDF or image file) purchased as part of your order**, is for a one-time use only and limited to any maximum distribution number specified in the license. The first instance of republication or reuse granted by this license must be completed within two years of the date of the grant of this license (although copies prepared before the end date may be distributed thereafter). The Wiley Materials shall not be used in any other manner or for any other purpose, beyond what is granted in the license. Permission is granted subject to an appropriate acknowledgement given to the author, title of the material/book/journal and the publisher. You shall also duplicate the copyright notice that appears in the Wiley publication in your use of the Wiley Material. Permission is also granted on the understanding that nowhere in the text is a previously published source acknowledged for all or part of this Wiley Material. Any third party content is expressly excluded from this permission.
- With respect to the Wiley Materials, all rights are reserved. Except as expressly granted by the terms of the license, no part of the Wiley Materials may be copied, modified, adapted (except for minor reformatting required by the new Publication), translated, reproduced, transferred or distributed, in any form or by any means, and no derivative works may be made based on the Wiley Materials without the prior permission of the respective copyright owner. **For STM Signatory Publishers clearing permission under the terms of the [STM Permissions Guidelines](#) only, the terms of the license are extended to include subsequent editions and for editions in other languages, provided such editions are for the work as a whole in situ and does not involve the separate exploitation of the permitted figures or extracts**, You may not alter, remove or suppress in any manner any copyright, trademark or other notices displayed by the Wiley Materials. You may not license, rent, sell, loan, lease, pledge, offer as security, transfer or assign the Wiley Materials on a stand-alone basis, or any of the rights granted to you hereunder to any other person.
- The Wiley Materials and all of the intellectual property rights therein shall at all times remain the exclusive property of John Wiley & Sons Inc, the Wiley Companies, or their respective licensors, and your interest therein is only that of having possession of and the right to reproduce the Wiley Materials pursuant to Section 2 herein during the continuance of this Agreement. You agree that you own no right, title or interest in or to the Wiley Materials or any of the intellectual property rights therein. You shall have no rights hereunder other than the license as provided for above in Section 2. No right, license or interest to any trademark, trade name, service mark or other branding ("Marks") of WILEY or its licensors is granted hereunder, and you agree that you shall not assert any such right, license or interest with respect thereto
- NEITHER WILEY NOR ITS LICENSORS MAKES ANY WARRANTY OR REPRESENTATION OF ANY KIND TO YOU OR ANY THIRD PARTY,

EXPRESS, IMPLIED OR STATUTORY, WITH RESPECT TO THE MATERIALS OR THE ACCURACY OF ANY INFORMATION CONTAINED IN THE MATERIALS, INCLUDING, WITHOUT LIMITATION, ANY IMPLIED WARRANTY OF MERCHANTABILITY, ACCURACY, SATISFACTORY QUALITY, FITNESS FOR A PARTICULAR PURPOSE, USABILITY, INTEGRATION OR NON-INFRINGEMENT AND ALL SUCH WARRANTIES ARE HEREBY EXCLUDED BY WILEY AND ITS LICENSORS AND WAIVED BY YOU.

- WILEY shall have the right to terminate this Agreement immediately upon breach of this Agreement by you.
- You shall indemnify, defend and hold harmless WILEY, its Licensors and their respective directors, officers, agents and employees, from and against any actual or threatened claims, demands, causes of action or proceedings arising from any breach of this Agreement by you.
- IN NO EVENT SHALL WILEY OR ITS LICENSORS BE LIABLE TO YOU OR ANY OTHER PARTY OR ANY OTHER PERSON OR ENTITY FOR ANY SPECIAL, CONSEQUENTIAL, INCIDENTAL, INDIRECT, EXEMPLARY OR PUNITIVE DAMAGES, HOWEVER CAUSED, ARISING OUT OF OR IN CONNECTION WITH THE DOWNLOADING, PROVISIONING, VIEWING OR USE OF THE MATERIALS REGARDLESS OF THE FORM OF ACTION, WHETHER FOR BREACH OF CONTRACT, BREACH OF WARRANTY, TORT, NEGLIGENCE, INFRINGEMENT OR OTHERWISE (INCLUDING, WITHOUT LIMITATION, DAMAGES BASED ON LOSS OF PROFITS, DATA, FILES, USE, BUSINESS OPPORTUNITY OR CLAIMS OF THIRD PARTIES), AND WHETHER OR NOT THE PARTY HAS BEEN ADVISED OF THE POSSIBILITY OF SUCH DAMAGES. THIS LIMITATION SHALL APPLY NOTWITHSTANDING ANY FAILURE OF ESSENTIAL PURPOSE OF ANY LIMITED REMEDY PROVIDED HEREIN.
- Should any provision of this Agreement be held by a court of competent jurisdiction to be illegal, invalid, or unenforceable, that provision shall be deemed amended to achieve as nearly as possible the same economic effect as the original provision, and the legality, validity and enforceability of the remaining provisions of this Agreement shall not be affected or impaired thereby.
- The failure of either party to enforce any term or condition of this Agreement shall not constitute a waiver of either party's right to enforce each and every term and condition of this Agreement. No breach under this agreement shall be deemed waived or excused by either party unless such waiver or consent is in writing signed by the party granting such waiver or consent. The waiver by or consent of a party to a breach of any provision of this Agreement shall not operate or be construed as a waiver of or consent to any other or subsequent breach by such other party.
- This Agreement may not be assigned (including by operation of law or otherwise) by you without WILEY's prior written consent.
- Any fee required for this permission shall be non-refundable after thirty (30) days from receipt by the CCC.
- These terms and conditions together with CCC's Billing and Payment terms and conditions (which are incorporated herein) form the entire agreement between you and

WILEY concerning this licensing transaction and (in the absence of fraud) supersedes all prior agreements and representations of the parties, oral or written. This Agreement may not be amended except in writing signed by both parties. This Agreement shall be binding upon and inure to the benefit of the parties' successors, legal representatives, and authorized assigns.

- In the event of any conflict between your obligations established by these terms and conditions and those established by CCC's Billing and Payment terms and conditions, these terms and conditions shall prevail.
- WILEY expressly reserves all rights not specifically granted in the combination of (i) the license details provided by you and accepted in the course of this licensing transaction, (ii) these terms and conditions and (iii) CCC's Billing and Payment terms and conditions.
- This Agreement will be void if the Type of Use, Format, Circulation, or Requestor Type was misrepresented during the licensing process.
- This Agreement shall be governed by and construed in accordance with the laws of the State of New York, USA, without regards to such state's conflict of law rules. Any legal action, suit or proceeding arising out of or relating to these Terms and Conditions or the breach thereof shall be instituted in a court of competent jurisdiction in New York County in the State of New York in the United States of America and each party hereby consents and submits to the personal jurisdiction of such court, waives any objection to venue in such court and consents to service of process by registered or certified mail, return receipt requested, at the last known address of such party.

## **WILEY OPEN ACCESS TERMS AND CONDITIONS**

Wiley Publishes Open Access Articles in fully Open Access Journals and in Subscription journals offering Online Open. Although most of the fully Open Access journals publish open access articles under the terms of the Creative Commons Attribution (CC BY) License only, the subscription journals and a few of the Open Access Journals offer a choice of Creative Commons Licenses. The license type is clearly identified on the article.

### **The Creative Commons Attribution License**

The [Creative Commons Attribution License \(CC-BY\)](#) allows users to copy, distribute and transmit an article, adapt the article and make commercial use of the article. The CC-BY license permits commercial and non-

### **Creative Commons Attribution Non-Commercial License**

The [Creative Commons Attribution Non-Commercial \(CC-BY-NC\) License](#) permits use, distribution and reproduction in any medium, provided the original work is properly cited and is not used for commercial purposes.(see below)

### **Creative Commons Attribution-Non-Commercial-NoDerivs License**

The [Creative Commons Attribution Non-Commercial-NoDerivs License \(CC-BY-NC-ND\)](#) permits use, distribution and reproduction in any medium, provided the original work is properly cited, is not used for commercial purposes and no modifications or adaptations are made. (see below)

### **Use by commercial "for-profit" organizations**

Use of Wiley Open Access articles for commercial, promotional, or marketing purposes requires further explicit permission from Wiley and will be subject to a fee.

Further details can be found on Wiley Online Library

<http://olabout.wiley.com/WileyCDA/Section/id-410895.html>

**Other Terms and Conditions:**

**v1.10 Last updated September 2015**

**Questions? [customercare@copyright.com](mailto:customercare@copyright.com) or +1-855-239-3415 (toll free in the US) or +1-978-646-2777.**

---

---

**JOHN WILEY AND SONS LICENSE  
TERMS AND CONDITIONS**

Apr 22, 2018

This Agreement between Mr. Christopher Russoniello ("You") and John Wiley and Sons ("John Wiley and Sons") consists of your license details and the terms and conditions provided by John Wiley and Sons and Copyright Clearance Center.

License Number	4334361007065
License date	Apr 22, 2018
Licensed Content Publisher	John Wiley and Sons
Licensed Content Publication	Journal of Geophysical Research: Oceans
Licensed Content Title	Variability in Benthic Exchange Rate, Depth, and Residence Time Beneath a Shallow Coastal Estuary
Licensed Content Author	
Licensed Content Date	Mar 8, 2018
Licensed Content Pages	1
Type of use	Dissertation/Thesis
Requestor type	Author of this Wiley article
Format	Print and electronic
Portion	Full article
Will you be translating?	No
Title of your thesis / dissertation	THE EFFECT OF WAVES ON BENTHIC EXCHANGE: MEASUREMENT AND ESTIMATION OVER A BROAD RANGE OF SPATIAL AND TEMPORAL SCALES
Expected completion date	May 2018
Expected size (number of pages)	150
Requestor Location	Mr. Christopher Russoniello 600 Hibben Magie Dr. Apt 112  PRINCETON, NJ 08540 United States Attn: Mr. Christopher Russoniello
Publisher Tax ID	EU826007151
Total	0.00 USD

[Terms and Conditions](#)

**TERMS AND CONDITIONS**

This copyrighted material is owned by or exclusively licensed to John Wiley & Sons, Inc. or one of its group companies (each a "Wiley Company") or handled on behalf of a society with which a Wiley Company has exclusive publishing rights in relation to a particular work (collectively "WILEY"). By clicking "accept" in connection with completing this licensing transaction, you agree that the following terms and conditions apply to this transaction (along with the billing and payment terms and conditions established by the Copyright Clearance Center Inc., ("CCC's Billing and Payment terms and conditions"), at the time that

you opened your RightsLink account (these are available at any time at <http://myaccount.copyright.com>).

## Terms and Conditions

- The materials you have requested permission to reproduce or reuse (the "Wiley Materials") are protected by copyright.
- You are hereby granted a personal, non-exclusive, non-sub licensable (on a stand-alone basis), non-transferable, worldwide, limited license to reproduce the Wiley Materials for the purpose specified in the licensing process. This license, **and any CONTENT (PDF or image file) purchased as part of your order**, is for a one-time use only and limited to any maximum distribution number specified in the license. The first instance of republication or reuse granted by this license must be completed within two years of the date of the grant of this license (although copies prepared before the end date may be distributed thereafter). The Wiley Materials shall not be used in any other manner or for any other purpose, beyond what is granted in the license. Permission is granted subject to an appropriate acknowledgement given to the author, title of the material/book/journal and the publisher. You shall also duplicate the copyright notice that appears in the Wiley publication in your use of the Wiley Material. Permission is also granted on the understanding that nowhere in the text is a previously published source acknowledged for all or part of this Wiley Material. Any third party content is expressly excluded from this permission.
- With respect to the Wiley Materials, all rights are reserved. Except as expressly granted by the terms of the license, no part of the Wiley Materials may be copied, modified, adapted (except for minor reformatting required by the new Publication), translated, reproduced, transferred or distributed, in any form or by any means, and no derivative works may be made based on the Wiley Materials without the prior permission of the respective copyright owner. **For STM Signatory Publishers clearing permission under the terms of the [STM Permissions Guidelines](#) only, the terms of the license are extended to include subsequent editions and for editions in other languages, provided such editions are for the work as a whole in situ and does not involve the separate exploitation of the permitted figures or extracts**, You may not alter, remove or suppress in any manner any copyright, trademark or other notices displayed by the Wiley Materials. You may not license, rent, sell, loan, lease, pledge, offer as security, transfer or assign the Wiley Materials on a stand-alone basis, or any of the rights granted to you hereunder to any other person.
- The Wiley Materials and all of the intellectual property rights therein shall at all times remain the exclusive property of John Wiley & Sons Inc, the Wiley Companies, or their respective licensors, and your interest therein is only that of having possession of and the right to reproduce the Wiley Materials pursuant to Section 2 herein during the continuance of this Agreement. You agree that you own no right, title or interest in or to the Wiley Materials or any of the intellectual property rights therein. You shall have no rights hereunder other than the license as provided for above in Section 2. No right, license or interest to any trademark, trade name, service mark or other branding ("Marks") of WILEY or its licensors is granted hereunder, and you agree that you shall not assert any such right, license or interest with respect thereto
- NEITHER WILEY NOR ITS LICENSORS MAKES ANY WARRANTY OR REPRESENTATION OF ANY KIND TO YOU OR ANY THIRD PARTY, EXPRESS, IMPLIED OR STATUTORY, WITH RESPECT TO THE MATERIALS OR THE ACCURACY OF ANY INFORMATION CONTAINED IN THE

MATERIALS, INCLUDING, WITHOUT LIMITATION, ANY IMPLIED WARRANTY OF MERCHANTABILITY, ACCURACY, SATISFACTORY QUALITY, FITNESS FOR A PARTICULAR PURPOSE, USABILITY, INTEGRATION OR NON-INFRINGEMENT AND ALL SUCH WARRANTIES ARE HEREBY EXCLUDED BY WILEY AND ITS LICENSORS AND WAIVED BY YOU.

- WILEY shall have the right to terminate this Agreement immediately upon breach of this Agreement by you.
- You shall indemnify, defend and hold harmless WILEY, its Licensors and their respective directors, officers, agents and employees, from and against any actual or threatened claims, demands, causes of action or proceedings arising from any breach of this Agreement by you.
- IN NO EVENT SHALL WILEY OR ITS LICENSORS BE LIABLE TO YOU OR ANY OTHER PARTY OR ANY OTHER PERSON OR ENTITY FOR ANY SPECIAL, CONSEQUENTIAL, INCIDENTAL, INDIRECT, EXEMPLARY OR PUNITIVE DAMAGES, HOWEVER CAUSED, ARISING OUT OF OR IN CONNECTION WITH THE DOWNLOADING, PROVISIONING, VIEWING OR USE OF THE MATERIALS REGARDLESS OF THE FORM OF ACTION, WHETHER FOR BREACH OF CONTRACT, BREACH OF WARRANTY, TORT, NEGLIGENCE, INFRINGEMENT OR OTHERWISE (INCLUDING, WITHOUT LIMITATION, DAMAGES BASED ON LOSS OF PROFITS, DATA, FILES, USE, BUSINESS OPPORTUNITY OR CLAIMS OF THIRD PARTIES), AND WHETHER OR NOT THE PARTY HAS BEEN ADVISED OF THE POSSIBILITY OF SUCH DAMAGES. THIS LIMITATION SHALL APPLY NOTWITHSTANDING ANY FAILURE OF ESSENTIAL PURPOSE OF ANY LIMITED REMEDY PROVIDED HEREIN.
- Should any provision of this Agreement be held by a court of competent jurisdiction to be illegal, invalid, or unenforceable, that provision shall be deemed amended to achieve as nearly as possible the same economic effect as the original provision, and the legality, validity and enforceability of the remaining provisions of this Agreement shall not be affected or impaired thereby.
- The failure of either party to enforce any term or condition of this Agreement shall not constitute a waiver of either party's right to enforce each and every term and condition of this Agreement. No breach under this agreement shall be deemed waived or excused by either party unless such waiver or consent is in writing signed by the party granting such waiver or consent. The waiver by or consent of a party to a breach of any provision of this Agreement shall not operate or be construed as a waiver of or consent to any other or subsequent breach by such other party.
- This Agreement may not be assigned (including by operation of law or otherwise) by you without WILEY's prior written consent.
- Any fee required for this permission shall be non-refundable after thirty (30) days from receipt by the CCC.
- These terms and conditions together with CCC's Billing and Payment terms and conditions (which are incorporated herein) form the entire agreement between you and WILEY concerning this licensing transaction and (in the absence of fraud) supersedes all prior agreements and representations of the parties, oral or written. This Agreement

may not be amended except in writing signed by both parties. This Agreement shall be binding upon and inure to the benefit of the parties' successors, legal representatives, and authorized assigns.

- In the event of any conflict between your obligations established by these terms and conditions and those established by CCC's Billing and Payment terms and conditions, these terms and conditions shall prevail.
- WILEY expressly reserves all rights not specifically granted in the combination of (i) the license details provided by you and accepted in the course of this licensing transaction, (ii) these terms and conditions and (iii) CCC's Billing and Payment terms and conditions.
- This Agreement will be void if the Type of Use, Format, Circulation, or Requestor Type was misrepresented during the licensing process.
- This Agreement shall be governed by and construed in accordance with the laws of the State of New York, USA, without regards to such state's conflict of law rules. Any legal action, suit or proceeding arising out of or relating to these Terms and Conditions or the breach thereof shall be instituted in a court of competent jurisdiction in New York County in the State of New York in the United States of America and each party hereby consents and submits to the personal jurisdiction of such court, waives any objection to venue in such court and consents to service of process by registered or certified mail, return receipt requested, at the last known address of such party.

## **WILEY OPEN ACCESS TERMS AND CONDITIONS**

Wiley Publishes Open Access Articles in fully Open Access Journals and in Subscription journals offering Online Open. Although most of the fully Open Access journals publish open access articles under the terms of the Creative Commons Attribution (CC BY) License only, the subscription journals and a few of the Open Access Journals offer a choice of Creative Commons Licenses. The license type is clearly identified on the article.

### **The Creative Commons Attribution License**

The [Creative Commons Attribution License \(CC-BY\)](#) allows users to copy, distribute and transmit an article, adapt the article and make commercial use of the article. The CC-BY license permits commercial and non-

### **Creative Commons Attribution Non-Commercial License**

The [Creative Commons Attribution Non-Commercial \(CC-BY-NC\) License](#) permits use, distribution and reproduction in any medium, provided the original work is properly cited and is not used for commercial purposes.(see below)

### **Creative Commons Attribution-Non-Commercial-NoDerivs License**

The [Creative Commons Attribution Non-Commercial-NoDerivs License \(CC-BY-NC-ND\)](#) permits use, distribution and reproduction in any medium, provided the original work is properly cited, is not used for commercial purposes and no modifications or adaptations are made. (see below)

### **Use by commercial "for-profit" organizations**

Use of Wiley Open Access articles for commercial, promotional, or marketing purposes requires further explicit permission from Wiley and will be subject to a fee.

Further details can be found on Wiley Online Library

<http://olabout.wiley.com/WileyCDA/Section/id-410895.html>

## **Other Terms and Conditions:**

**v1.10 Last updated September 2015**

**Questions? [customercare@copyright.com](mailto:customercare@copyright.com) or +1-855-239-3415 (toll free in the US) or +1-978-646-2777.**

---

---